UNIVERSITY OF SOUTHAMPTON

FACULTY OF ENGINEERING, SCIENCE AND MATHEMATICS

Optoelectronics Research Centre

Broadband Sources and Fibre Delay Line for the Functionality Enhancement of Optical Coherence Tomography Application

by

King Nien Wong

Thesis submitted for the degree of Master of Philosophy

September 2007

UNIVERSITY OF SOUTHAMPTON

ABSTRACT

FACULTY OF ENGINEERING, SCIENCE AND MATHEMATICS

OPTOELECTRONICS RESEARCH CENTRE

Master of Philosophy

BROADBAND SOURCES AND FIBRE DELAY LINE FOR THE FUNCTIONALITY ENHANCEMENT OF OPTICAL COHERENCE TOMOGRAPHY APPLICATION

by King Nien Wong

The usage of supercontinuum sources has enabled a significant improvement of tomographic imaging in optical coherence tomography (OCT) systems. However, because of the intensity noise, the clarity of the OCT image can be sacrificed even though much finer axial resolution can be obtained when using this technology. Using a commercial supercontinuum SC450 (Fianium, UK) source, its performance in terms of its interference signal shape and its relative intensity noise (RIN) was compared with two other broadband sources, a semiconductor optical amplifier (SOA) and an erbium-doped fibre amplifier (EDFA). As a measure of axial resolution in OCT; by using different grating filters the full width at half maximum (FWHM) of the interference signal and the RIN figure for each source is analysed. The measured RIN value for the SC450 is found to be between ~26.8 dB and ~30.5 dB times noisier, in terms of power fluctuation, when compared to the SOA and EDFA.

The construction of dispersion compensated chirped fibre Bragg gratings (CFBGs) in an all fibre optical delay line was also discussed in this thesis. Using a pair of identical CFBGs and positioning them in a reversed cascaded orientation against each other, the anticipated Gaussian-like interference signal was successfully obtained when one of the CFBGs was stretched.

The development of a time-domain OCT system was also highlighted in this thesis. The OCT system can be used to perform a meaningful scan on small and thin transparent samples. An OCT image of a mirror sample was presented, taken using full bandwidth of the SOA source. Later, the SOA was amplified at higher driving current when scanning a biological sample and the OCT image of an onion skin was successfully constructed. Problems encountered during this research project were also highlighted and future work to be done to try to overcome these were also outlined.

Contents

List of Figures

List of Tables

DECLARATION OF AUTHORSHIP

I, ……King Nien Wong…….declare that the thesis entitled “.....Broadband sources and fibre delay line for functionality enhancement of Optical Coherence Tomography”……and the work presented in the thesis are both my own, and have been generated by me as the result of my own original research. I confirm that:

- this work was done wholly or mainly while in candidature for a research degree at this University;

- where any part of this thesis has previously been submitted for a degree or any other qualification at this University or any other institution, this has been clearly stated;

- where I have consulted the published work of others, this is always clearly attributed;

- where I have quoted from the work of others, the source is always given. With the exception of such quotations, this thesis is entirely my own work;

- I have acknowledged all main sources of help;

- where the thesis is based on work done by myself jointly with others, I have made clear exactly what was done by others and what I have contributed myself;

- none of this work has been published before submission.

Signed: ……..
Date:…….

Acknowledgement

I thank my supervisor, Dr. Morten Ibsen, whose help, brilliant creativity, and enthusiasm have guided me from the beginning until today. All the long and interesting conversations we have had benefited me in many ways.

I thank Dr. Anatoly Grudinin, whose help, through his Fianium company, has enable me to loan a unit of their supercontinuum source – SC450. Without it, this study would not have been a success.

I thank my past and present research group members; i.e. Nyuk Yung Voo, Albert Canagasabey, and Zhaowei Zhang whose input and bright discussion provided the stimulating ideas and environment to carry forward my research.

I thank Dr. Anoma McCoy, who has helped collaboratively in the noise measurement research. Her remarkable wide experience together with her generous assistance and advaice has brought this research to completion with ease.

I am grateful for the help of the technicians; Simon Butler and Timothy McIntyre in their quality workmanship crafting my project setup.

Last but not least, I would like to express gratitude to Mrs. Eveline Smith and Dr. Eleanor Tarbox in providing smooth administrative and supervision in my study progress and throughout my transition here.

Nomenclature

c	Speed of light in the vacuum
k	Propagation constant in the vacuum
n_{eff}	Effective modal index
β	Mode propagation constant
β_2	Group delay dispersion parameter
γ	Complex degree of coherence/ also nonlinear parameter
λ_B	Bragg wavelength
ε	Strain
λ	Wavelength
Λ	Grating pitch
ρ_e	Elasto-optic coefficient
τ	Time delay
ω	Angular frequency
λ_o	Central wavelength
$\Delta\lambda$	Full width at half maximum spectral width
I	Intensity
E	Electric field
P	Polarisation
Γ	Mutual coherence function
A_{eff}	Effective core area
α	Attenuation coefficient
v_g	Group velocity dispersion
n	Refractive index
v	Frequency
v	Velocity
f_D	Doppler frequency
f	Focal length

Δx	Focused spot size
z_R	Rayleigh range
b	Confocal parameter
NA_{obj}	Numerical aperture of the microscope objective
d	Spot size
A	Complex amplitude of the electrical pulse
P	Power
χ	Susceptibility
ε_o	Permittivity of free space
ϕ	Phase
q	Electron charge
R_L	Load resistance
k_B	Boltzmann constant
P	Power
$\Delta\lambda_B$	Shift of Bragg wavelength
r	Mode field radii

Acronyms

A/D	Analog-to-digital
AC	Alternating current
APC	Angle-polished connector
ASE	Amplified spontaneous emission
CFBG	Chirped fibre Bragg grating
CMRR	Common-mode-rejection-ratio
CW	Continuous wave
DFG	Difference frequency generation
EDFA	Erbium-doped fibre amplifier
FWHM	Full width at half maximum
FWM	Four wave mixing
GDR	Group delay ripple
GVD	Group velocity dispersion
NA	Numerical aperture
NIR	Near infra-red
OCT	Optical coherence tomography
OSA	Optical spectrum analyser
PCF	Photonic crystal fibre
PSD	Power spectral density
RF	Radio frequency
RIN	Relative intensity noise
RMS	Root mean square
RSODL	Rapid scanning optical delay line
SLD	Superluminescent diode
SMF	Single mode fibre
SOA	Semiconductor optical amplifier
SPM	Self phase modulation
SRS	Stimulated Raman scattering
UV	Ultra violet

Chapter 1

Overview

Optical coherence tomography (OCT) can be used to perform *in vivo*, high resolution cross-sectional imaging of microstructures in transparent as well as turbid biological tissues [1, 2]. It is analogous to ultrasound B-scan imaging except that it uses light instead of acoustic vibration to create the image. The term A-scan and B-scan are used commonly in OCT and ultrasonography because of the similarities in the way both techniques are constructing their images or tomograms. An A-scan is a one dimensional, axial profile obtained at a point location while B-scan is a two dimensional, cross sectional image of the sample that is built up from a laterally displaced A-scans. OCT has less penetration depth than ultrasound techniques but its main advantage is that it can provide micron level resolution, routinely achieving around 10 μm, which improves the ultrasound resolution more than a factor of ten [3]. OCT has great advantages over other medical imaging systems too. For example, magnetic resonance imaging (MRI) methods are not suitable for tissue morphology imaging and have poor resolution compared to OCT. MRI's average resolution is only 1 mm and its imaging execution is very slow. Confocal microscopy instead does not allow morphological tissue imaging and lacks millimetre penetration depth. Confocal microscopy has better image resolution at 1 μm but it currently suffers from a limited penetration depth of 200 μm.

OCT uses the correlation or interferometry techniques to measure the reflected light intensity. Low coherence interferometry is used as it has the capability of measuring time delay of light. Low coherence interferometry was first developed for measuring reflections in fibre optics and optoelectronic devices [4-6]. It relies on the interference between a split, and later re-combined, broadband optical field. The broadband light source is coupled into an interferometer and the light is split into two fields. The split field travels in a reference path, reflecting from a reference mirror,

and also in a sample path where it is reflected from multiple layers within the sample (Fig. 1.1). Interference between the optical fields can only be observed when the optical path lengths of the reference and sample arm are matched within the coherence length of the broadband source. Therefore the depth (axial) resolution of an OCT system is determined by the temporal coherence of the light source.

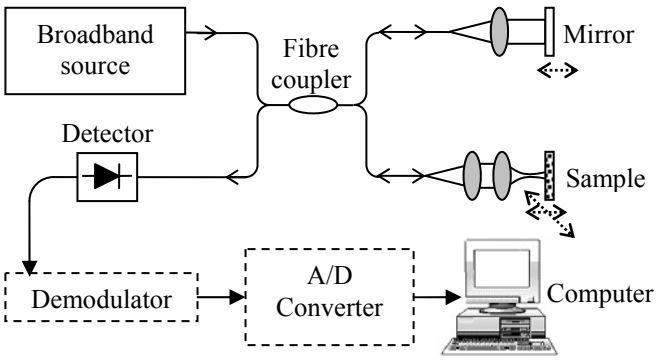

Fig. 1.1: A typical OCT system.

A time domain interference pattern can be obtained by translating the reference mirror to match the optical paths of both the reference and sample arms. A light beam is focused onto the sample and the intensity of the backscattered light and its time delay are measured to yield an axial backscattering profile. Later a multiple depth scan is performed by moving the scanning beam laterally, and its backscattering profile is measured at those lateral positions to produce a two-dimensional set of data.

For more comprehensive reading of OCT's theory, latest developments and its breakthrough applications please refer to reviews by Schmitt [7] , Fercher *et al.*[8] Sampson *et al.* [3] and Tomlins *et al.* [9]. These authors have made a very thorough review of the OCT technology ever since its inception in 1991 [1]. The applications for this technology are extensive. To date, OCT technology has been demonstrated for applications in biomedical fields such as ophthalmology, optical biopsy in dermatology, dental, cardiovascular medicine, endoscopy and oncology [10, 11]. OCT can also be adapted to other real world applications such as optical metrology evaluation in highly scattering media. Nondestructive testing of material defects is also prossible [12]. To date, a small number of OCT scanners have found their way to commercialisation [13, 14].

1.1 Broadband Sources for Optical Coherence Tomography

According to Sampson [15], one of the technologies that is having an enormous impact on the OCT research field is the ultrahigh resolution OCT systems. To reduce down to micron level resolution imaging, many researchers have used a new type of broadband source, which is the supercontinuum generation based on optical fibre technology, as it has the potential to provide a low coherence and high power light source. Thus it is realised that the key parameter for the OCT backbone, is

Table 1.1: Examples of broadband sources used in OCT systems

Source	λ_o (nm)	$\Delta\lambda$ (nm)	Emission power	Reference
SLD	675	8.5	5 mW	
	820	20	2 mW	
	980	30	30 mW	[16]
	1050	35	30 mW	
	1300	35	10 mW	
	1550	40	10 mW	
Kerr lens mode-locked laser				
Ti:Al_2O_3	776	176	20 mW	Unterhuber *et al.*[17]
Cr:$^{4+}$:forsterite	1280	75	30 mW	Tearney *et al.*[18]
Superfluorescence fibres				
Er-doped	1550	40 - 80	10–100 mW	Bouma *et al.*[19]
Tm-doped	1800	80	7 mW	"
Nd/Yb-doped	1060	65	108 mW	Paschotta [20]
Photonic crystal fibre	725	325	27 mW	Považay *et al.*[21]
	1100	372	100 mW	Wang *et al.*[22]
High-NA nonlinear fibre	1000	139	n.a.	Bourquin *et al.*[23]

the selection of proper broadband sources. More on this topic will be reviewed in Chapter 2.

Table 1.1 lists the characteristics of a variety of broadband sources suitable for use in OCT. The most commonly used sources in OCT systems are superluminescent diodes (SLDs). Because of their adequate level of irradiance and relatively low cost, superluminescent sources come close to being the ideal sources for OCT imaging. Commercially available SLDs [16] cover a wide range of wavelengths and many can provide broad bandwidth spectra. Until recently, however, the average power and bandwidth of these sources limited their application to slow acquisition and modest resolution imaging.

The high power and wide bandwidth mode-locked Ti:Al_2O_3 laser has made it an attractive source for fast and high resolution OCT imaging. Femtosecond laser development has concentrated so far mainly on the temporal features of the pulses, which were often optimized at the expense of the spectral shape. In OCT however, the pulse duration is irrelevant, while the spectral width and shape play a crucial role. Unlike ultrafast femtosecond time-resolved measurements, where special care must be exercised to maintain the short pulse duration, OCT measurements depend on field correlations rather than intensity correlations. Field correlation is preserved even if the pulse duration is long. Moreover, its lack of portability limits its use in clinical applications.

Much work has been done to find the best broadband light solution to produce the best OCT image quality [24]. The best sub-micrometer ultrahigh resolution OCT imaging ever reported to date is 0.75 μm [21]. To produce such a short coherence length, Považay *et al.* uses a commercial photonic crystal fibre (PCF) pumped by a Kerr lens, mode-locked, Ti:Al_2O_3 laser to generate a supercontinuum spectrum at a mean wavelength of 725 nm and having a spectral width of 325 nm. PCF is a promising new class of light source emitting a low temporal coherence light, similarly to other broadband light sources. Supercontinuum generation is more efficient when generated from PCF compared with other nonlinear media. More discussion of supercontinuum generation will be explained in Section 2.2.

A recent review paper by Drexler [25] highlights the level of activity in ultrahigh resolution OCT. The main activity has been the development and deployment of supercontinuum generation sources in various forms of nonlinear optical fibres in the OCT research area. The primary goal has been to push the

resolution as small as possible and to reduce the complexity, cost and size of this source. However, performance degradation is likely to be observed when a supercontinuum broadband source is used in the OCT system as it keeps producing intensity noise many tens of decibels above the pump noise [26]. The noise originates from the nonlinear amplification of quantum fluctuations in the input laser light and in the Raman scattering process within the PCF used for supercontinuum generation. In Section 4.3, the experimental investigation will be carried out to characterize the noise sources of a commercial supercontinuum source.

1.2 Motivation

1.2.1 Supercontinuum Source Characterisation

Recent advances in optical telecoms technology have played some part in rolling out optical devices, suitable for OCT imaging, at a fast pace and relatively low cost. The advent of supercontinuum sources from PCF has enabled the possibility of acquiring ultrahigh resolution tomographic images for OCT applications in a scale of a few microns. It is very important to know the quality outcome of OCT images using the supercontinuum as the broadband source. This aspect of the new generation of broadband sources has been little studied in OCT. In this thesis, early work on characterizing the supercontinuum SC450 source (Fianium UK) performance will be studied. Its relative intensity noise (RIN) was measured and compared against the standard performance of two thermal-like light sources; i.e. semiconductor optical amplifier (SOA) and erbium doped fibre amplifier (EDFA). Also, using different grating filter shapes, their RIN value is compared. This study will be reported in Chapter 4 of this thesis.

1.2.2 All Fibre Optical Delay Line Study

Present OCT systems have delay lines based on bulk optics. The reference arm is controlled using various optical delay techniques such as moving mirrors, rotating prisms, and rapid scanning optical delay (RSODL) which uses a Fourier domain technique. To obtain a delay, the beam must come out from fibre, pass though the bulk-optics based delay line and then recouple back to fibre. An all fibre optical delay

line for use in the OCT system will be constructed; it will consist of two chirped fibre Bragg gratings cascaded in opposite directions with one of the gratings being stretched to amplify the optical path delay. The motivation of using this method is that there is no coupling or insertion loss, there is ease of alignment, it is less bulky, more compact and durable; all of which are inherent properties of fibre optics. This study will be reported in Chapter 5 of this thesis.

1.3 Arrangement of Thesis

This thesis is organised in the following manner. Chapter 2 will give a brief overview of low coherence interferometry – the key technology in OCT. Then follows an explanation of the nonlinear effects required for the supercontinuum generation in photonic crystal fibre. In the following chapter, the development of a time domain OCT system in the gratings lab will be thoroughly discussed. In Chapter 4, early work on noise characterisation in terms of interference signal performance for each SC450, SOA and EDFA source will be reported as well as their RIN measurement using various grating filters. In Chapter 5, the development of an all fibre optical delay line in the OCT reference arm will be covered. Then to wrap up, in the sixth chapter, the conclusions and the future work of this research study will be summarised.

1.4 References

1. D. Huang, E. A. Swanson, C. P. Lin, J. S. Schuman, W. G. Stinson, W. Chang, M. R. Hee, T. Flotte, K. Gregory, C. A. Puliafito, and J. G. Fujimoto, "Optical coherence tomography," Science **254**, 1178-1181 (1991).

2. J. G. Fujimoto, M. E. Brezinski, G. J. Tearney, S. A. Boppart, B. Bouma, M. R. Hee, J. F. Southern, and E. A. Swanson, "Optical biopsy and imaging using optical coherence tomography," Nature Medicine **1**, 970-972 (1995).

3. D. D. Sampson, and T. R. Hillman, *Optical Coherence Tomography, Chapter 17 in Lasers and Current Optical Techniques in Biology* (Royal Society of Chemistry, Cambridge, UK, 2004).

4. K. Takada, I. Yokohama, K. Chida, and J. Noda, "New measurement system for fault location in optical waveguide devices based on an interferometric technique," Applied Optics **26**, 1603-1606 (1987).

5. R. C. Youngquist, S. Carr, and D. E. N. Davies, "Optical coherence-domain reflectometry: a new optical evaluation technique," Optics Letters **12**, 158-160 (1987).

6. H. H. Gilgen, R. P. Novak, R. P. Salathe, W. Hodel, and P. Beaud, "Submillimeter optical reflectometry," Journal of Lightwave Technology **7**, 1225-1233 (1989).

7. J. M. Schmitt, "Optical coherence tomography (OCT): a review," IEEE Journal of Selected Topics in Quantum Electronics **5**, 1205-1215 (1999).

8. A. F. Fercher, W. Drexler, C. K. Hitzenberger, and T. Lasser, "Optical coherence tomography - Principles and applications," Reports on Progress in Physics **66**, 239-303 (2003).

9. P. H. Tomlins, and R. K. Wang, "Theory, developments and applications of optical coherence tomography," Journal of Physics D: Applied Physics **38**, 2519-2535 (2005).

10. M. E. Brezinski, *Optical Coherence Tomography: Principles and Applications* (Elsevier, Burlington, MA, 2006).

11. B. E. Bouma, and G. J. Tearney, *Handbook of Optical Coherence Tomography,* (Marcel Dekker, New York, 2002).

12. M. Bashkansky, M. D. Duncan, M. Kahn, D. Lewis, III, and J. Reintjes, "Subsurface defect detection in ceramics by high-speed high-resolution optical coherent tomography," Optics Letters **22**, 61-63 (1997).

13. http://www.lightlabimaging.com/.

14. http://www.thorlabs.com/OCT/index.cfm.

15. D. D. Sampson, "Trends and prospects for optical coherence tomography," in *Proceedings of SPIE - The International Society for Optical Engineering*(2004), pp. 25-32.

16. http://www.superlumdiodes.com/.

17. A. Unterhuber, B. Považay, B. Hermann, H. Sattmann, W. Drexler, V. Yakovlev, G. Tempea, C. Schubert, E. M. Anger, P. K. Ahnelt, M. Stur, J. E. Morgan, A. Cowey, G. Jung, T. Le, and A. Stingl, "Compact, low-cost Ti:Al2O3 laser for in vivo ultrahigh-resolution optical coherence tomography," Optics Letters **28**, 905-907 (2003).

18. G. J. Tearney, M. E. Brezinski, B. E. Bouma, S. A. Boppart, C. Pitris, J. F. Southern, and J. G. Fujimoto, "In vivo endoscopic optical biopsy with optical coherence tomography," Science **276**, 2037-2039 (1997).

19. B. E. Bouma, L. E. Nelson, G. J. Tearney, D. J. Jones, M. E. Brezinski, and J. G. Fujimoto, "Optical coherence tomographic imaging of human tissue at 1.55 μM and 1.81 μM using ER- and TM-doped fiber sources," Journal of Biomedical Optics **3**, 76-79 (1998).

20. R. Paschotta, J. Nilsson, A. C. Tropper, and D. C. Hanna, "Efficient superfluorescent light sources with broad bandwidth," IEEE Journal on Selected Topics in Quantum Electronics **3**, 1097-1099 (1997).

21. B. Považay, K. Bizheva, A. Unterhuber, B. Hermann, H. Sattmann, A. F. Fercher, W. Drexler, A. Apolonski, W. J. Wadsworth, J. C. Knight, P. S. J. Russell, M. Vetterlein, and E. Scherzer, "Submicrometer axial resolution optical coherence tomography," Optics Letters **27**, 1800-1802 (2002).

22. Y. Wang, Y. Zhao, J. S. Nelson, Z. Chen, and R. S. Windeler, "Ultrahigh-resolution optical coherence tomography by broadband continuum generation from a photonic crystal fiber," Optics Letters **28**, 182-184 (2003).

23. S. Bourquin, I. Hartl, A. D. Aguirre, P. L. Hsiung, T. H. Ko, T. A. Birks, W. J. Wadsworth, U. Bünting, D. Kopf, and J. G. Fujimoto, "Portable broadband light sources using a femtosecond Nd: Glass laser and nonlinear fiber for ultrahigh resolution OCT imaging," in *Proceedings of SPIE - The International Society for Optical Engineering*(2003), pp. 4-8.

24. A. Unterhuber, B. Považay, K. Bizheva, B. Hermann, H. Sattmann, A. Stingl, T. Le, M. Seefeld, R. Menzel, M. Preusser, H. Budka, C. Schubert, H. Reitsamer, P. K. Ahnelt, J. E. Morgan, A. Cowey, and W. Drexler, "Advances in broad bandwidth light sources for ultrahigh resolution optical coherence tomography," Physics in Medicine and Biology **49**, 1235-1246 (2004).

25. W. Drexler, "Ultrahigh-resolution optical coherence tomography," Journal of Biomedical Optics **9**, 47-74 (2004).

26. N. R. Newbury, B. R. Washburn, K. L. Corwin, and R. S. Windeler, "Noise amplification during supercontinuum generation in microstructure fiber," Optics Letters **28**, 944-946 (2003).

Chapter 2

Background

This chapter will examine the principle behind using low coherence interferometry, utilising a broadband source in OCT and later give a brief explanation of nonlinear effects required for supercontinuum generation.

2.1 Low Coherence Interferometry in Optical Coherence Tomography

Optical coherence tomography (OCT) is a two beam interferometric technique which uses low coherence or partially coherent light. In a basic Michelson interferometer case, shown in Fig. 2.1, the beam wave is split into reference field E_1 and sample field E_2. After reflecting back from the reference mirror and scattering back from the sample, both fields mix on the surface of photodetector.

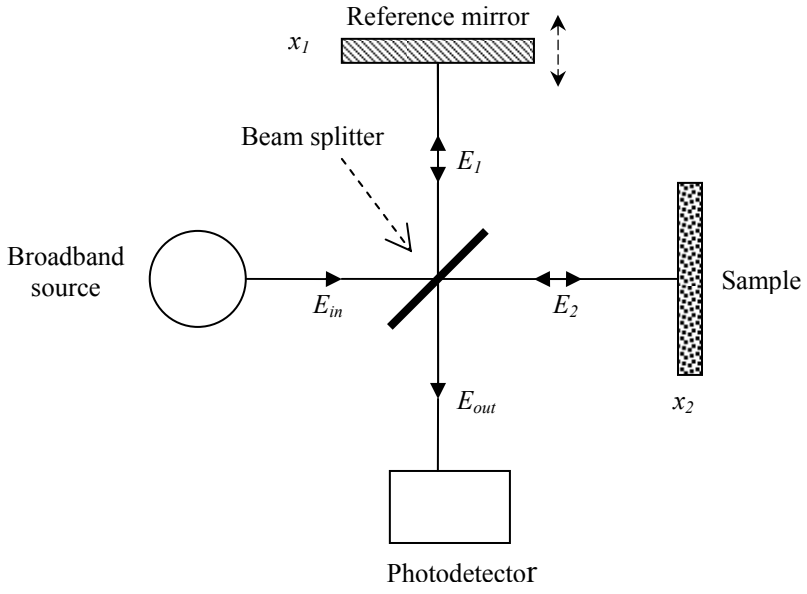

Fig. 2.1: Basic OCT system, based on a Michelson interferometer.

Optical detectors are square law intensity detection devices, where the intensity is proportional to a time average over the electric field multiplied by its complex conjugate. Thus the intensity that is incident on the photodetector is

$$I_{out}(\tau) = \left\langle E_{out} E_{out}^{*} \right\rangle \tag{2.1}$$

$$= \left\langle E_1 E_1^{*} \right\rangle + \left\langle E_2 E_2^{*} \right\rangle + 2\,\mathrm{Re}\{\Gamma_{12}(\tau)\} \tag{2.2}$$

$$= \left\langle |\, E_1 \,|^2 \right\rangle + \left\langle |\, E_2 \,|^2 \right\rangle + 2\,\mathrm{Re}\left\{ \left\langle E_1(t+\tau) E_2^{*}(t) \right\rangle \right\} \tag{2.3}$$

$$= I_1 + I_2 + G_{12}(\tau) \tag{2.4}$$

where I_1 and I_2 are mean (dc) intensities returning from the reference and sample arms of the interferometer.

The key function in the theory of partially coherent light is the mutual coherence function. The time average portion of the last term in Eq. 2.3 is a cross-correlation function, which is denoted by

$$\Gamma_{12}(\tau) = \left\langle E_1(t+\tau) E_2^{*}(t) \right\rangle \tag{2.5}$$

and referred to as the mutual coherence function of the light field at x_1 and x_2.

In many cases it is convenient to work with a normalised version of the mutual coherence function, rather than the mutual coherence function itself. The normalised form of the mutual coherence function is defined as

$$\gamma_{12}(\tau) = \frac{\Gamma_{12}(\tau)}{\sqrt{\Gamma_{11}(0)\Gamma_{22}(0)}} = \frac{\left\langle E_1(t+\tau) E_2^{*}(t) \right\rangle}{\sqrt{\left\langle |\, E_1 \,|^2 \right\rangle \left\langle |\, E_2 \,|^2 \right\rangle}} \tag{2.6}$$

which is also known as the complex degree of coherence of the light. Take note that at position x_1, when $\tau = 0$, self coherence of the light reduces to the intensity, $\Gamma_{11}(0) = \left\langle |\, E_1 \,|^2 \right\rangle = I_1$. The same applies for the light field at position x_2. For future reference, $\gamma_{12}(0) = 1$ and $|\gamma_{12}(\tau)| \leq 1$. Eq. (2.3) can now be recast as

$$I_{out}(\tau) = I_1 + I_2 + 2\sqrt{I_1 I_2}\,\mathrm{Re}\{\gamma_{12}(\tau)\} \tag{2.7}$$

or

$$= I_1 + I_2 + 2\sqrt{I_1 I_2}\,|\gamma_{12}(\tau)|\cos[2\pi\upsilon\tau] \tag{2.8}$$

which is the general interference law for the partially coherent light. The visibility, V

$$V = \frac{2\sqrt{I_1 I_2}\,|\gamma_{12}(\tau)|}{I_1 + I_2} \tag{2.9}$$

defines the depth or contrast of the interference fringe.

The modulus $|\gamma_{12}(\tau)|$ of the complex degree of coherence is a direct measure of the fringe visibility. In the special case, $I_1 = I_2$, the visibility and the modulus of the complex degree of coherence are identical:

$$V = |\gamma_{12}(\tau)|. \tag{2.10}$$

From the definition of visibility, it is clear for partially coherent light, we have $0<|\gamma_{12}(\tau)|<1$. When $\gamma_{12}(\tau) = 1$ or 0, we have completely coherent or incoherent light respectively.

In a two beam interferometry set-up, when two beams, I_1 and I_2 from the reference and sample arm respectively, coincide at the detector, the mutual coherence function reduces to an autocorrelation function $G_{12}(\tau)$ (Eq. 2.4) which contains only temporal effects. The term $G_{12}(\tau)$ is the interferogram and it depends on the optical time delay τ set by the position of the reference mirror. It represents the amplitude of the interference signals that carry information about the sample under scan. The nature of the interference signal depends on the degree to which the temporal and spatial characteristics (coherence properties) of E_1 and E_2 match. Its real part represents an interferogram with the fringes spread out

$$G_{12}(\tau) = 2\sqrt{I_1 I_2}\cos[2\pi\upsilon\tau]. \tag{2.11}$$

where $\tau = l/c$ with the l as the optical path travelled by the moving mirror and c is the speed of light.

As it is an autocorrelation function, the Wiener-Khincin theorem states that its Fourier transform is the power spectrum $S(\upsilon)$ of the light source [1]. Since Γ is an analytic signal and has no components of negative frequency:

$$S(\upsilon) = \int_{-\infty}^{+\infty} \Gamma_{12}(\tau) \exp(i2\pi\upsilon\tau) d\tau \qquad (\upsilon \geq 0) \tag{2.12}$$

thus

$$G_{12}(\tau) = \int_{0}^{\infty} S(\upsilon) \exp(-i2\pi\upsilon\tau) d\upsilon \tag{2.13}$$

$S(\upsilon)$ is the transform of $G_{12}(\tau)$, the real part of $\Gamma_{12}(\tau)$ that describes the intensity modulation, that is, the interferogram. The interferogram and power spectrum are thus Fourier transforms of each other. From this relationship, the shape and width of the light source spectrum are the important variable in OCT. The width of this autocorrelation function, or the coherence length, is inversely proportional to the width of the power spectrum.

The axial resolution is determined by the coherence length, l_c of the light source. For a source with a Gaussian spectral distribution, the axial resolution is [2]

$$\Delta z = l_c = \frac{2\ln 2}{\pi} \frac{\lambda_o^{\,2}}{\Delta\lambda} \tag{2.14}$$

where λ_o is the centre wavelength and $\Delta\lambda$ is the full width at half-maximum (FWHM) spectral width. Fig. 2.2 shows the relationship of axial resolution with the choice of different sources' central wavelength and their FWHM bandwidth. Higher resolution is influenced only by the source spectrum. Thus high resolution can be achieved independently of the beam focusing condition. The mechanisms that govern the axial and lateral image resolution in OCT are independent.

The lateral resolution in the OCT imaging system is determined by the focused spot size, as in conventional microscopy, which is

$$\Delta x = \frac{4\lambda}{\pi}\left(\frac{f}{d}\right) \tag{2.15}$$

where d is the spot size of the objective lens and f is its focal length. In general optics, f/d = 1/(2 NA_{obj}) where NA_{obj} is referring to the numerical aperture of the microscope objective which is inversely proportional to the lateral resolution. The lateral resolution is also related to the depth of focus or the confocal parameter, b which is $2z_R$, two times the Rayleigh range

$$b = 2z_R = \frac{\pi \Delta x^2}{2\lambda} \tag{2.16}$$

Improving the lateral resolution produces a decrease in the depth of focus, similar to conventional microscopy.

Penetration depth of OCT is determined by the emission wavelength and source power. In general, the OCT imaging depth of penetration is limited by both absorption and scattering. Both of these sources of attenuation are wavelength dependent. The presence of these two phenomena can degrade the axial resolution of an OCT image. A common limiting factor for optical imaging of biological tissues is the absorption profile of water in the wavelengths at 0.8 and 1.3 μm. Another setback is the short mean scattering lengths of photons in tissue at wavelengths in the blue and ultraviolet wavelengths. OCT imaging with a source that emits in these spectral regions would be limited to layers of few hundred micrometres thick. However scattering decreases monotonically in the red and near infra-red (NIR) regions as the light experiences highly forward-directed scattering interactions in tissue. Hence imaging in this region of the spectrum is preferable even though water absorption increases here. Maximizing OCT imaging depth of penetration therefore requires the use of a centre wavelength that balances these two influences of absorption and scattering. Choosing a source with a centre wavelength of 1 μm is the most optimal, as the influence of absorption and dispersion of water in tissue is the least at this wavelength [3].

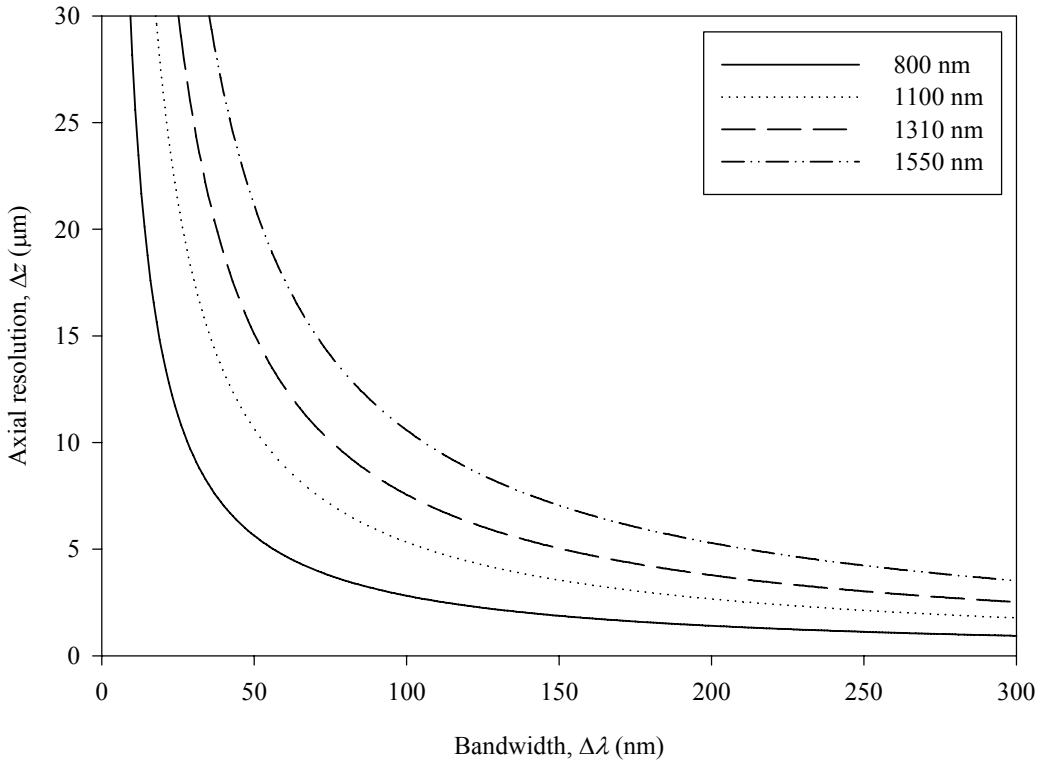

Fig. 2.2: Relationship of OCT's axial resolution against the FWHM bandwidth of the broadband source being used.

As mentioned earlier, the light source is the key technological parameter for an OCT system, and a proper choice is very important. For this purpose, the supercontinuum source has been identified as the likely candidate for improving the axial resolution in OCT applications. With its integral properties of very broad spectra and high power source, the supercontinuum source is seen as having the potential for source integration into OCT systems. In the next section, an overview of the nonlinear effects required for supercontinuum generation will be briefly discussed.

2.2 Supercontinuum Generation

Ever since it started being reported in 1970 [4], it has been observed that intense picosecond pulses can exhibit spectral broadening upon nonlinear propagation through transparent glasses and crystals. Similar broadening has also been observed in in liquid [5] and gases [6]. The supercontinuum generation in microstructured fibre or photonic crystal fibre (PCF) was first demonstrated by Ranka *et al*.[7] who reported the generation of a supercontinuum spectrum extending from 390 nm to 1600 nm by launching pulses of 100 fs duration, 8-kW peak power, and a centre wavelength of 790 nm into a 75 cm length of microstructure fibre with a zero dispersion wavelength at ~ 767 nm [7].

Supercontinuum generation is a universal feature of the light-matter interaction. Supercontinuum or white light generation is a nonlinear spectral broadening phenomenon in the frequency domain upon launching intense ultrashort pulses (Fig. 2.3). The origin of supercontinuum generation can be traced back to the nonlinear Schrödinger equation. The general term for nonlinear pulse propagation in a single-mode fibre can be expressed using the nonlinear Schrödinger equation [8]

$$\frac{\partial A}{\partial z}+\frac{1}{\upsilon_g}\frac{\partial A}{\partial t}+\frac{i}{2}\beta_2\frac{\partial^2 A}{\partial t^2}+\frac{\alpha}{2}A=i\gamma\left|A\right|^2 A \tag{2.17}$$

where z is the longitudinal coordinate along the fibre, t is the time in the reference frame travelling with the pump light, α is the fibre loss, and A is the pulse envelope function. The first two terms on the left-hand side describe the envelope propagation of the pulse in fibre at the group velocity υ_g, while effects of the group-velocity dispersion (GVD) are governed by β_2 and the last term is the effects of fibre loss. The nonlinear parameter γ is defined as

$$\gamma=\frac{n_2\omega_o}{cA_{eff}}=\frac{2\pi n_2}{A_{eff}\lambda}. \tag{2.18}$$

The second-order nonlinear refractive index is $n_2 \sim 2.2 \times 10^{-20}$ m^2/W for silica fibres and it is frequency independent [8]. In PCF the γ value is higher than those in

conventional fibres. This is because of the large refractive index step between silica and air which allows light to be concentrated in a small area, thus resulting in an enhanced nonlinear effect. The parameter A_{eff} is the effective core area of the PCF material given by

$$A_{eff} = \frac{\left(\int\int_{-\infty}^{+\infty} |F(x,y)|^2 \, dxdy\right)^2}{\int\int_{-\infty}^{+\infty} |F(x,y)|^4 \, dxdy} \tag{2.19}$$

where $F(x,y)$ is the transverse mode function. When the normalised frequency $V = 2\pi a/\lambda \sqrt{n_{co}^2 - n_{cl}^2}$ is in the vicinity of 2, the effective core area is well approximated by $A_{eff} = \pi a^2$, where a is the core radius [8]. The value of V determines the number of confined modes that exist in the core. If the value of V for a fibre is less than 2.405, it can be shown that only single mode propagation is satisfied.

However, Eq. 2.17 does not include the effects of stimulated Raman scattering (SRS) and four wave mixing (FWM). The right hand side of Eq. 2.17 already models the self-phase modulation (SPM) nonlinear optical effect.

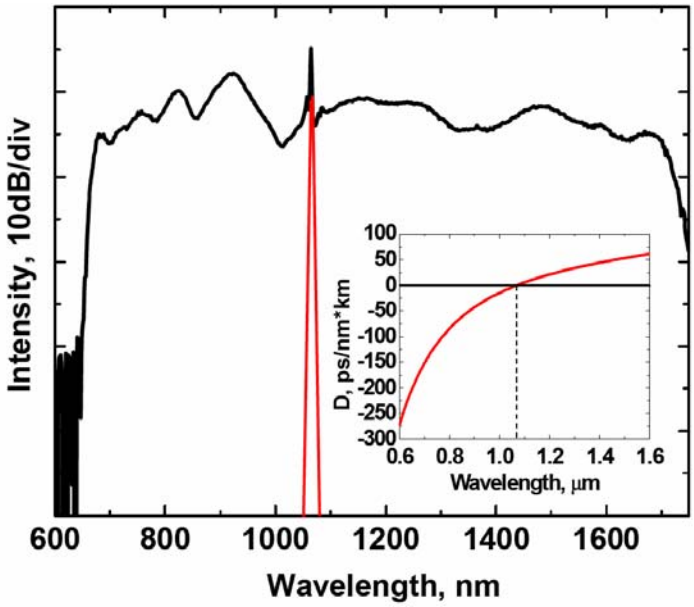

Fig. 2.3: Broadened spectrum and its input laser pump (peak at 1064 nm). Inset shows the PCF dispersion map. (From [9]).

No consensus of theoretical explanations has been given for the spectral behaviour of broadening in a supercontinuum. The processes behind supercontinuum generation, depended particularly on pulse duration (nanosecond, picosecond or femtosecond) and the peak power. Typically, SPM, SRS and FWM are the dominant contributors. These processes are briefly discussed in the next few sections. It has been found that many different operating regimes allow for supercontinuum generation and in these various regimes the process can drastically differ.

2.2.1 Fibre Nonlinearities

When an intense electromagnetic field is applied to a material, the response of the material depends in the nonlinear manner, upon the strength of the optical field. The polarisation **P** induced by the electric dipoles can be expressed as a power series in electric field **E** as

$$\mathbf{P} = \varepsilon_0 \left(\chi^{(1)} \cdot \mathbf{E} + \chi^{(2)} : \mathbf{EE} + \chi^{(3)} \vdots \mathbf{EEE} + ... \right), \tag{2.20}$$

where ε_0 is the permittivity of free space, and $\chi^{(j)}$ (j = 1,2,…) is the jth order susceptibility and a tensor rank j + 1 of the medium. For silica fibre, an isotropic centrosymmetric material, the number of independent terms in the third order susceptibility $\chi^{(3)}$ is reduced to only three [8]. For centrosymmetric molecules only odd-order susceptibilities are non-zero. The third order susceptibility $\chi^{(3)}$ can be non-zero for centrosymmetric and noncentrosymmetric materials. As a result, the lowest order nonlinear phenomena in silica fibre originate from $\chi^{(3)}$. The second-order susceptibility $\chi^{(2)}$ however vanishes for centrosymmetric material. $\chi^{(2)}$ can gives rise to nonlinear effects such as sum and difference frequency generation and second harmonic generation. The $\chi^{(3)}$ term is responsible for nonlinear effects such as third harmonic generation, two photon absorption, four wave mixing and nonlinear refractive index [8]. The FWM and SRS nonlinear effects covered in this section originate from this third-order susceptibility $\chi^{(3)}$.

2.2.2 Self Phase Modulation

When a high optical intensity light is launched into an optical fibre, it will cause a nonlinear phase delay which has the same temporal shape as the optical intensity. This effect produces a refractive index change with intensity, I

$$n(I) = n_o + n_2 I \tag{2.21}$$

where n_o is the linear refractive index, and n_2 is the second-order nonlinear refractive index of fibre. When the optical pulse is travelling in the fibre, this will cause a time-dependent phase shift according to the time-dependent pulse intensity. For this, the initial unchirped optical pulse acquires a chirped shape; a temporally varying instantaneous frequency. For a Gaussian pulse, propagating the distance of L, the instantaneous frequency $\omega(t)$ is given by [8]

$$\omega(t) = \omega_o + \frac{4\pi L n_2 I}{\lambda T^2} \cdot t \cdot \exp\left(-\frac{t^2}{T^2}\right) \tag{2.22}$$

where ω_o is the carrier frequency of the pulse and T is the half-width (at 1/e intensity point). In practice it is customary to use the FWHM in place of T. Plotting $\omega(t)$ shows the frequency of each part of the pulse (Fig. 2.4).

In the normal dispersion regime, lower frequencies or 'redder' portions of the pulse travel faster than higher frequencies or 'blue' portions. Thus, the front pulse moves faster than the back, which broadens the pulse in time. In the regions of anomalous dispersion, the pulse is compressed temporally and becomes shorter. This effect can be exploited to produce ultrashort pulse compression and soliton effects.

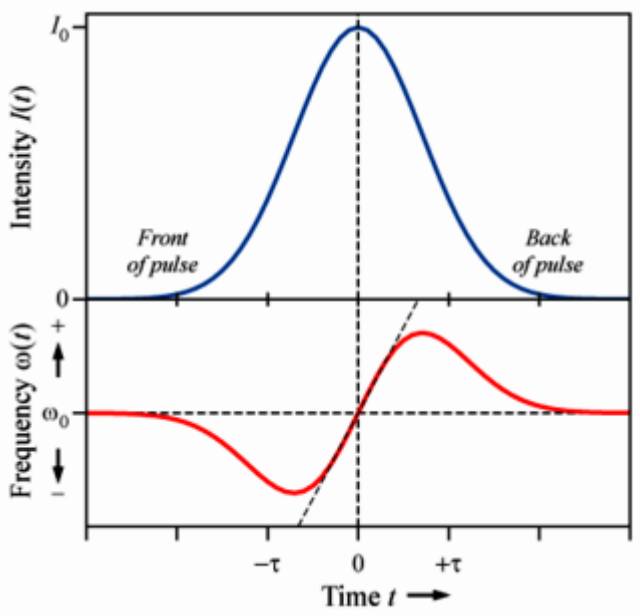

Fig. 2.4: A pulse (top curve) propagating through a nonlinear medium, e.g. an optical fibre, undergoes a self-frequency shift (bottom curve) due to SPM. The front of the pulse is shifted to lower frequencies, and the back to higher frequencies. In the centre of the pulse the frequency shift is approximately linear (From [8]).

2.2.3 Stimulated Raman Scattering

Stimulated Raman Scattering (SRS), a third-order susceptibility $\chi^{(3)}$ is an important nonlinear phenomenon that can lead to the generation of new spectral lines. By introducing the Raman effect for pulse evolution in SMF, SRS process can be included in Eq. 2.17 by modifying it to the generalised (or extended) nonlinear Schrödinger equation [8]. SRS results from a stimulated inelastic scattering process in which the optical field transfers part of its energy to the medium and generates a photon.

The spontaneous Raman effect can be observed when a beam of light illuminates any molecular medium and the scattered light is observed spectroscopically. The Raman effect scatters only a small fraction of the incident optical field into other fields. Those new frequency components are shifted to lower frequencies and are called the Stokes line and those shifted to higher frequencies are called the anti-Stokes lines. The amount of frequency shift is determined by the vibrational modes of molecules.

These properties of Raman scattering can be understood quantum mechanically through the use of energy level diagrams shown in Fig. 2.5.

Fig. 2.5: Energy level diagram describing (a) Raman Stokes scattering and (b) Raman anti-Stokes scattering.

Raman Stokes scattering can be described as an incoming photon of frequency ω_p that encounters one of the molecules in ground state *g* and excites the molecule to make a transition from the ground state to a virtual intermediate level associated with the excited state *n'*, followed by a transition from the virtual level to the final lower excited state *n* as the molecules emits a lower-frequency photon ω_S. Anti-Stokes Raman scattering consists of a transition from level *n* to level *g*, with *n'* serving as the intermediate level, resulting a higher-frequency photon ω_a. The anti-Stokes lines are typically orders of magnitude weaker than the Stokes lines. For PCF, when the pump power exceed a threshold value, a stimulated version of Raman scattering can occur in which the Stokes line grows rapidly inside the medium with high conversion efficiency. The lower energy Stokes lines are generated on the red-side of the spectrum whereas the anti-Stokes lines are shifted to the blue-side of the spectrum. In practice, the Stokes wave can serve as a pump to generate a second-order Stokes wave if its power exceeds the threshold value.

2.2.4 Four Wave Mixing

Four wave mixing (FWM) is a parametric process in the optical fibre which can be viewed as two photons of energies $\hbar\omega_1$ and $\hbar\omega_2$ that are annihilated and two new photons of energies $\hbar\omega_3$ and $\hbar\omega_4$ that are created such that the net energy is conserved during the process. It is a process where no energy is transferred to a

medium. Each of the four waves has its own direction of propagation, polarisation and frequency. For this process to occur, it requires the phase matching condition to be satisfied for momentum conservation. The parametric interactions are strongest when waves are phase-matched. Another equivalent way to understand this is by realizing that, since the energy transfer is a coherent process, all four photons or waves must maintain a constant phase relative to the others in order to avoid any destructive interference.

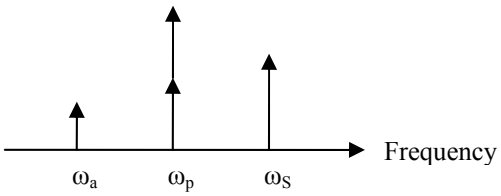

Fig. 2.6: Additional frequency generated in parametric FWM process.

Consider this process where two pump photons of equal frequency create a Stokes and anti-Stokes photon (Fig. 2.6) such that

$$\omega_p + \omega_p = \omega_S + \omega_a \,. \tag{2.23}$$

In a single mode fibre, when all four photons propagate in the fundamental mode in the same direction, the phase matching condition requirement can be written as

$$\Delta k = k_1 + k_2 - k_3 + k_4 \,. \tag{2.24}$$

where Δk is the phase mismatch. Fig. 2.7 shows the pictorial representation of the wave vector mismatch: situation (a) shows a finite wave vector mismatch, while (b) demonstrates the corresponding phase matched case.

Fig. 2.7: A typical phase matching diagram where (a) a vector mismatch of Δk and (b) is the perfectly phase matched case (From [10]).

2.2.5 Nonlinear Supercontinuum Generation in Photonic Crystal Fibre

Supercontinuum generation is more efficient in PCF compared to other nonlinear media. PCFs, in this example, are made up of silica where the core is surrounded by an array of microscopic air holes stretching along its entire length. The large refractive index step between the silica core and its air hole cladding enables light to be concentrated onto a very small area, hence resulting in enhanced nonlinear effects. Tight focusing of intense pump light thus increases the peak power and leads to broadening of the input spectrum or supercontinuum generation. For input pulses that are not too short (pulse width >1ns) and not too intense (peak power <10mW), the fibre plays a passive role (except for pulse energy losses) and acts as a transporter of optical pulses from one place to another [8]. In this case, its shape or spectrum will not be significantly affected. However as pulses become shorter or more intense, different effects of nonlinearity regime kick in.

SPM can lead to the increasing of the bandwidth due to nonlinear refractive index. When the pump wavelength of femtosecond pulses is close to the zero dispersion wavelength of the PCF, the low-power spectral broadening seems to be dominated by SPM. However, it has been demonstrated that femtosecond pulses are not necessarily needed for efficient supercontinuum generation in a PCF [11]. Using nanosecond and picosecond excitation instead, the role of SPM is limited because these pump pulses are long and the power sufficiently low to prevent the self-focusing effect. SRS will firstly dominate, in this case, and it will extend the spectrum at the long wavelength side of the pump, generating a broadband of frequencies between the pump wavelength and the zero dispersion wavelength [12]. In the second stage, these SRS generated frequencies serve as parametric pumps to continuously amplify the generated blue-shifted light of shorter wavelength through FWM. This mechanism is effective because phase matching is achieved regardless of the pump power and SPM has a negligible influence. In FWM, two photons are summed to produce two new photons of different frequencies. Efficient FWM requires that the process be phase-matched; i.e. $\Delta k = 0$.

2.3 Summary

In this chapter, it has been reviewed how the mechanism of OCT system works using the low coherence interferometry technique. Thus in the following Chapter 3, the development and demonstration of a time-domain OCT system will be reported, where its construction will be based on the basics reviewed earlier in this chapter. It has been showed too how supercontinuum spectrum from PCFs can be generated using the nonlinear effects of SPM, SRS and FWM. Its broadened white light will be used extensively in noise characterisation experiments, as discussed in Chapter 4.

2.4 References

1. W. H. Steel, *Interferometry* (Cambridge University Press, 1983).
2. D. Huang, E. A. Swanson, C. P. Lin, J. S. Schuman, W. G. Stinson, W. Chang, M. R. Hee, T. Flotte, K. Gregory, C. A. Puliafito, and J. G. Fujimoto, "Optical coherence tomography," Science **254**, 1178-1181 (1991).
3. Y. Wang, J. S. Nelson, Z. Chen, B. J. Reiser, R. S. Chuck, and R. S. Windeler, "Optimal wavelength for ultrahigh-resolution optical coherence tomography," Optics Express **11**, 1411-1417 (2003).
4. R. R. Alfano, and S. L. Shapiro, "Observation of Self-Phase Modulation and Small-Scale Filaments in Crystals and Glasses," Physical Review Letters **24**, 592 (1970).
5. W. L. Smith, P. Liu, and N. Bloembergen, "Superbroadening in H_2O and D_2O by self-focused picosecond pulses from a YAlG: Nd laser," Physical Review A **15**, 2396 (1977).
6. P. B. Corkum, C. Rolland, and T. Srinivasan-Rao, "Supercontinuum Generation in Gases," Physical Review Letters **57**, 2268 (1986).
7. J. K. Ranka, R. S. Windeler, and A. J. Stentz, "Visible continuum generation in air-silica microstructure optical fibers with anomalous dispersion at 800 nm," Optics Letters **25**, 25-27 (2000).
8. G. P. Agrawal, *Nonlinear Fiber Optics* (Academic Press, San Diego, California, 2001).
9. M. Rusu, A. B. Grudinin, and O. G. Okhotnikov, "Slicing the supercontinuum radiation generated in photonic crystal fiber using an all-fiber chirped-pulse amplification system," Optics Express **13**, 6390-6400 (2005).
10. J. F. Reintjes, *Nonlinear Optical Parametric Processes in Liquids and Gasses* (Acedemic Press, Orlando, 1984).
11. S. Coen, A. H. L. Chau, R. Leonhardt, J. D. Harvey, J. C. Knight, W. J. Wadsworth, and P. S. J. Russell, "Supercontinuum generation by stimulated Raman scattering and parametric four-wave mixing in photonic crystal fibers," Journal of the Optical Society of America B: Optical Physics **19**, 753-764 (2002).
12. S. Coen, A. H. L. Chau, R. Leonhardt, J. D. Harvey, J. C. Knight, W. J. Wadsworth, and P. S. J. Russell, "White-light supercontinuum generation with 60-ps pump pulses in a photonic crystal fiber," Optics Letters **26**, 1356-1358 (2001).

Chapter 3
Optical Coherence Tomography System Development

3.1 Introduction

This chapter will describe the development of a time-domain, fibre-based OCT system. Before the OCT system is able to generate OCT images, there are two major problems that need to be solved. First, the optical path lengths of the reference and sample arm need to be matched. For this, the length of the fibre used in the arms will be carefully measured and cut. Secondly, the sampling data acquired by the computer need to be synchronised, processed and fine controlled with the scanning optics movement so that a full complete image or tomogram can be constructed. For this, software will be developed to handle all these requirements.

3.2 Assembly and Preparation of OCT System

A simple time-domain OCT setup was designed and built, the schematic of which is shown in Fig. 3.1. A picture of the setup is shown in Fig. 3.2. The fibre based OCT system was chosen for a number of reasons [1]; compactness and durability, ease of beam coupling and alignment and its relatively wide acceptance in OCT research. Fibre optic implementations of OCT can also be used in conjunction with endoscopes or catheters to provide physicians with imaging of sub-surface tissue morphology.

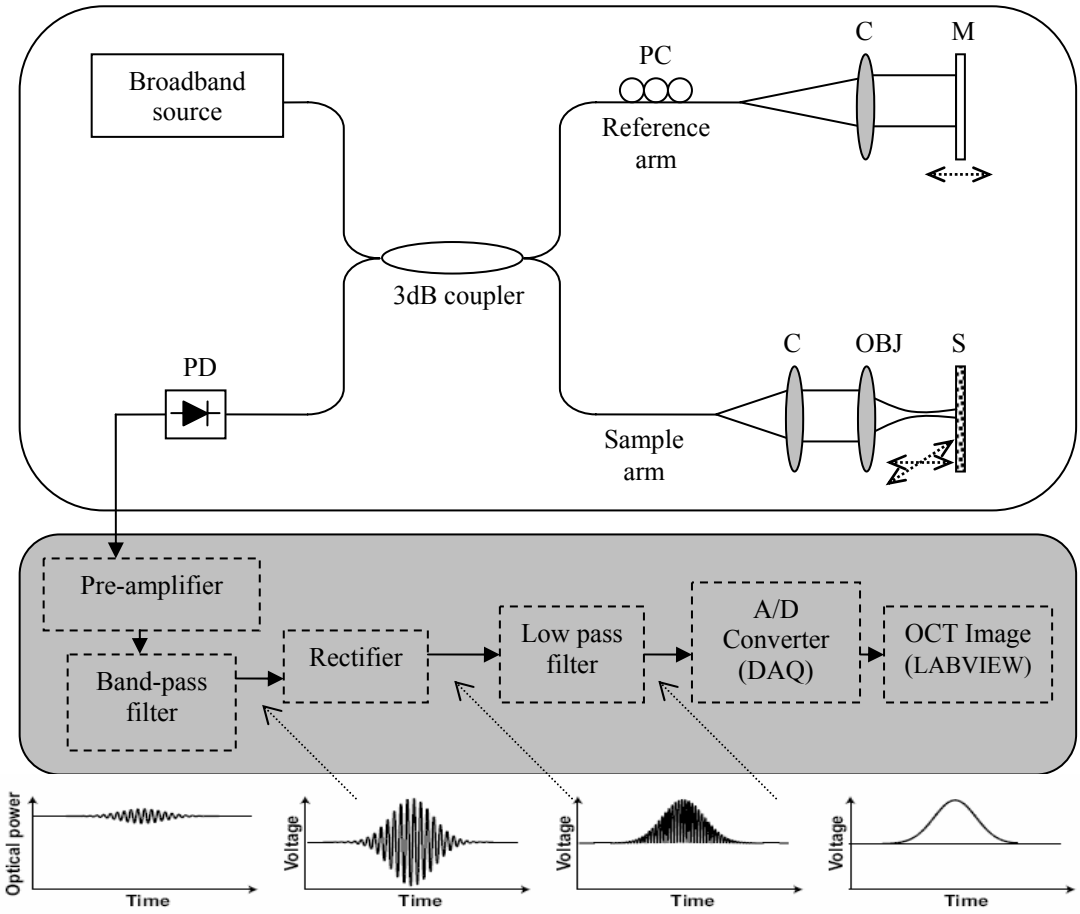

Fig. 3.1: Schematic diagram of the time-domain OCT system. PC: Polarization controller, PD: Photodetector, M: Mirror, OBJ: Objective lens, C: Collimator, S: Sample and DAQ: Data acquisition card.

Fig. 3.1 shows the schematic of a simplified fibre-based OCT system, which is divided into two parts, the optical part (upper box) and the electrical part (lower box). In the optical part, light from the broadband source is launched and split in half at the fibre coupler. The split light, reflected back from the reference arm and the sample arm, then later interfere at the coupler and are detected at the photodetector. The probe at the sample arm collects the detailed information on the sample. The electrical part of the OCT system translates the information into either a 2-dimensional or a 3-dimensional image.

The optical transmittance, coating, and wavelength-dependent losses of the fibre optics employed and the delivery system optics can strongly influence the axial resolution as well as the sensitivity of the OCT system.

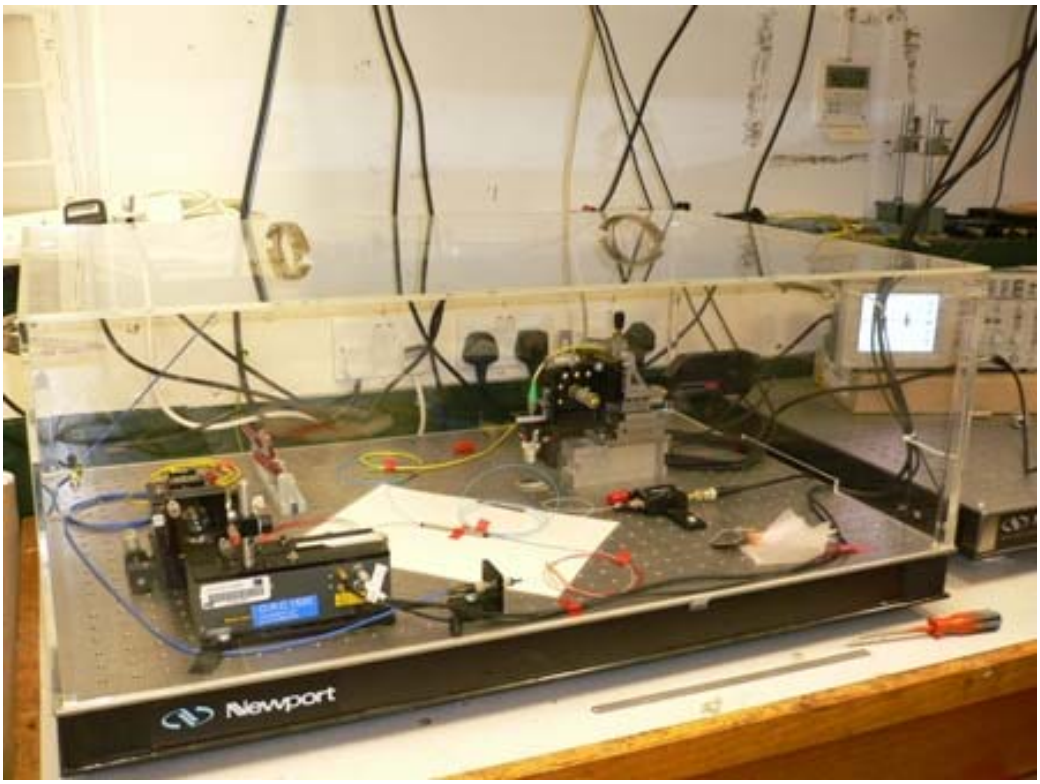

Fig. 3.2: OCT setup enclosed in a Perspex box for environmental temperature control.

Single-mode fibres (SMFs) with appropriate cut-off wavelengths have to be used to provide single-mode light propagation. For this setup, commercial optical fibre (SMF-28, Corning) was used. Conventional fibre couplers are designed to maintain 3 dB splitting over a wavelength range of typically ±10 nm. When using these fibre couplers for delivery of broad-bandwidth laser light, unequal beam splitting with respect to wavelength and power can occur and will reduce the resolution. Hence a broad bandwidth, wavelength flattened, 3 dB fibre optic coupler operating at 1550 nm wavelength was used. This is to maintain the broad bandwidths and consequently better axial resolution. It is important to note that bidirectionality of fibre-based beamsplitters is important in order not to introduce wavelength-dependent losses on the way back to the detector.

The low coherence interferometry is based on the occurrence of fringes if the optical path lengths of the reference and sample arms coincide within the size of coherence length. The length of the fibre arms are carefully measured and cut to match its coherence length. Angle polished connector (APC) patch cords are used in both arms to minimise backreflections. The polarisation controller is inserted in the reference arm to compensate for the polarisation mismatch in the two arms. The

polarisation of light can be caused by sample inhomogeneity, environmental temperature changes, connectorisation and bending of both fibre arms. Introducing the polarisation controller will allow the manual adjustment of the polarisation in the reference arm, and thus improve the sensitivity of the OCT system.

Light in the reference arm is reflected from an Al-coated mirror (reflectivity >90% at 1550 nm) which is mounted on a piezo stage (17AMP001, Melles Griot). The piezo stage was driven with a triangular waveform to simulate a linear scanning mechanism. The piezo stage is able to perform ~175 μm forward and backward translation and the velocity of the stage was set to 350 μm/s at 1 Hz driving frequency. This scanning range and velocity is relatively short and slow, respectively, compared with that of a state of the art OCT system. A rapid scanning optical delay line (RSODL) which uses Fourier domain technique can enable a speedier scanning in the range of several kHz and video rate imaging [2]. But then again, this and the earlier mirror techniques use bulky and expensive mirror optics. To compensate for these disadvantages, a new all fibre optical delay line is proposed and this will be covered in Chapter 5.

In the sample arm, the installed collimator (f = 11 mm, NA = 0.25) is able to wholly collect the light from the APC path cord as its numerical aperture is higher than the numerical aperture of the SMF, of 0.14. This beam is not entirely collimated, as the numerical aperture of the APC partch cord and the aspheric lens on the collimator is not the same. However, since the distance separation of the collimator and the objective lens is very near, the collected beam will be assumed collimated. The collimated beam is focused onto the sample using an objective lens (f = 23.5 mm, NA = 0.22) with low numerical aperture value. The beam is able to focus down onto a spot size, Δx = 4.3 μm (Eq. 2.15). This beam size, incident on the sample, determines the transverse or lateral resolution of the OCT image. The depth of focus, b, on the other hand is limited to 18.59 μm (Eq. 2.16). The common OCT technique is able to produce millimetre depth of penetration (approximately 2-3 millimetres in tissue). Thus, there is still plenty of room to scale up the current OCT system. The methods to improve this depth of focus will be discussed in Chapter 6. The mechanical performance of the scanning optics used for this transverse and depth scanning has to be accurately selected and correctly controlled. Mechanical jitter or displacement of adjacent depth scans as well as noisy control signals of the scanner might result in distorted, and therefore resolution degraded, OCT tomograms. A high performance

translation actuator (850G-HS, Newport) was used, which is able to shift the scanning optics at the resolution of 1 μm.

In the detection part, the photodetector (D400FC, Thorlabs) collects the interference signal, which contains information of the sample along with undesired noise. The received signal is weak and hence a pre-amplifier is used to boost up the signal power. A band-pass filter is used to filter out the undesired noise with the band-pass centre frequency locked at the Doppler frequency. A/D converter (PCI-MIO-16E-4, National Instrument) or a DAQ card is used to convert the analog signal into a 12-bit digital signal, which will be interfaced into a computer. The signal will then be demodulated to obtain the envelope of the fringe. The process of demodulation is currently being done offline using an in-house written MATLAB program. The demodulation process involves full-wave rectification of the signal, followed by low pass filtering and then storing of its final envelope function. The piezo stage motion control (17PCZ013, Melles Griot) in the reference arm and the 2-axis scanning optics actuator control (MM4005, Newport) in the same sample arm, together with the digitized signal were controlled by the LABVIEW program, as shown in Fig 3.3. The flow chart of the LABVIEW program is shown in the Appendix A.

This OCT system will serve as a foundation for experiments reported hereafter.

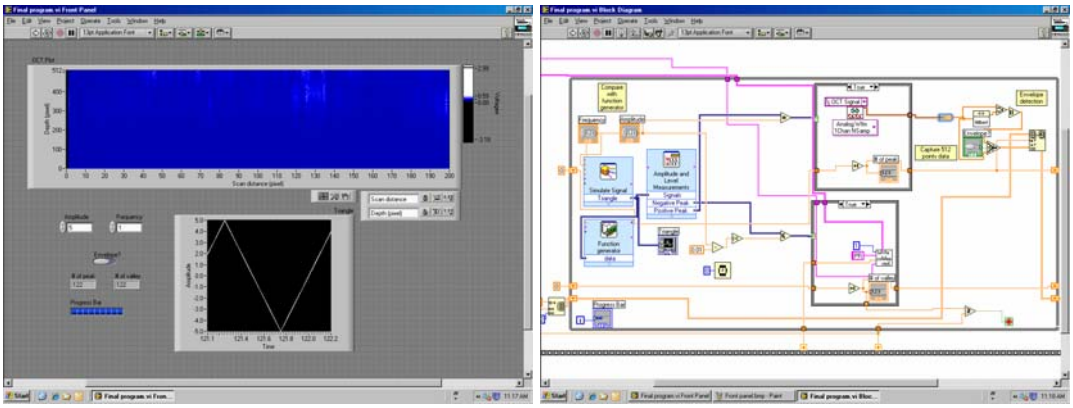

(a) (b)

Fig. 3.3: The developed LABVIEW OCT program showing (a) the front panel and (b) its block diagram

3.3 Interference Signal Detection and Multiple Samples Characterisation

Using a low coherence ASE signal, generated from an SOA (CQF874-308C, JDS Uniphase), operating at a centre wavelength λ_c = 1535.13 nm and having a 3 dB spectral bandwidth of 59.09 nm, its interference signal is obtained and detected (Fig. 3.4). The source signal is launched at full power of + 0.41 dBm. Theoretically, the axial resolution obtained using Eq. 2.14 would give a FWHM length of approximately 17.5 μm. Using a mirror as a sample under test, the FWHM of its interference signal is measured to be 17.6 ± 0.1 μm, which conforms to the coherence length of the SOA source.

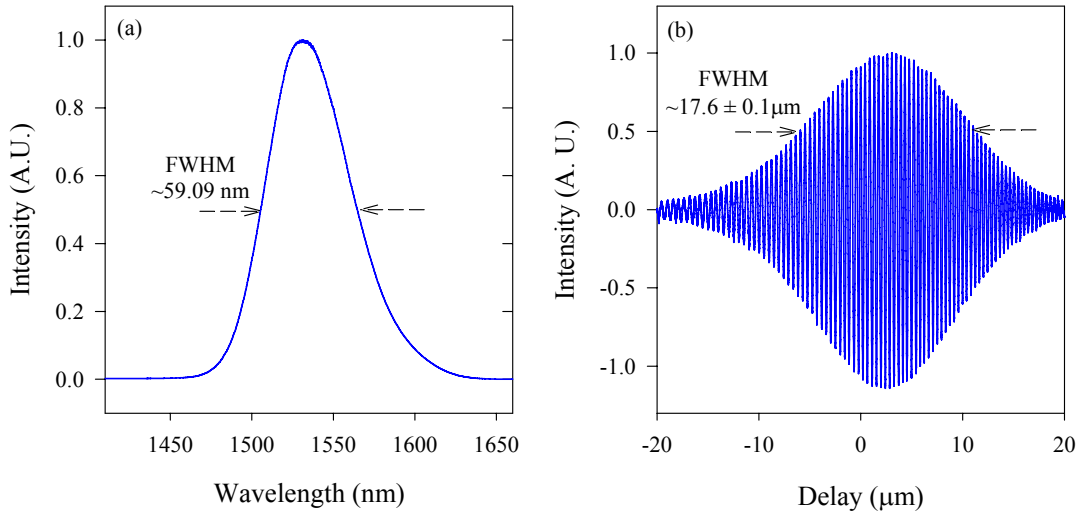

Fig. 3.4: (a) Full spectrum of the SOA source and (b) the interference signal of a mirror obtained using the SOA spectrum

To demonstrate the functionality of this OCT system to scan, three different transparent samples were used for a preliminary test. In the future, those samples can be used for system calibration before a meaningful OCT image scan can be performed on other inhomogeneous samples such as a biological tissue. The SOA was again used as the light source. The samples are listed in Table 3.1 together with their known thickness, which is measured using a micrometer. The samples are then placed under the scanning optics before each scanning is performed.

Table 3.1: List of samples under OCT characterisation

Sample	Refractive index	Thickness (± 0.005 mm)
Microscope glass slide	1.45	1.050
Plastic sheet	1.46	0.055
Plastic laminator	1.46	0.105

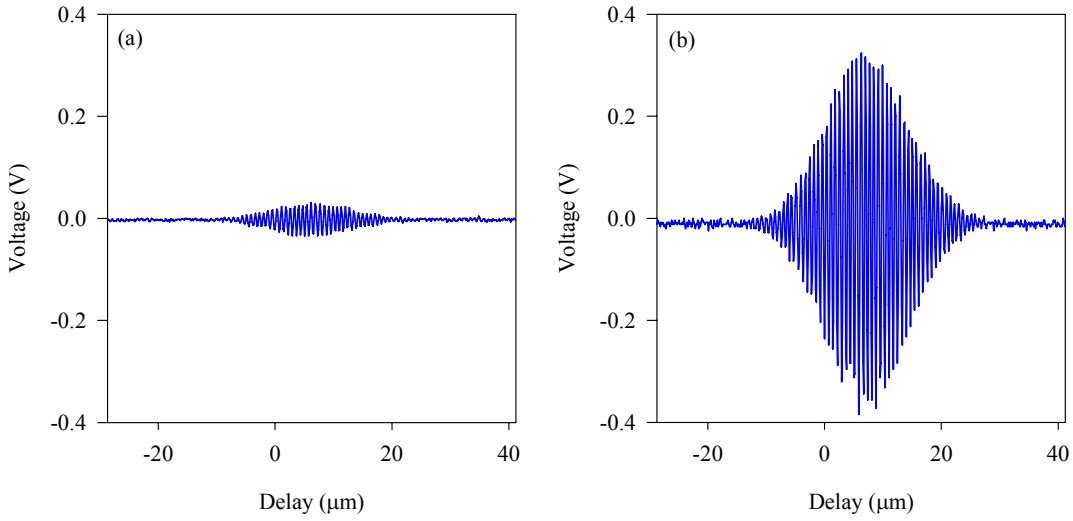

Fig. 3.5: Interference signal of microscope glass slide (a) scanned at 9.190 mm micrometer reading (bottom layer) (b) scanned at 10.790 mm micrometer reading (top layer)

As the thickness of the microscope glass slide is beyond the scanning range of each reference mirror sweep (± 175 μm), its interference signal is captured at two different focusing distances at the scanning probe. The scanning probe is affixed with a micrometer adjuster and can be manually adjusted. Its interference signals are shown in Fig. 3.5. From the two micrometer readings, the glass slide thickness is calculated to be (10.790 - 9.190) mm/1.45 = 1.100 mm. The calculated value does not differ much from the glass slide's real thickness (1.050 mm). The bottom layer produced a weaker backreflected fringe, as compared to the top layer, because the light signal will attenuate substantially while travelling to and fro the bottom layer.

The plastic sheet and plastic laminator used are not uniformly flat on their surfaces. From the interference signal in Fig. 3.6, two fringes can be observed. The bigger fringe of the two is the stronger backreflected light from the top layer of the plastic. From the two fringe distances in Fig. 3.6(a), the plastic sheet thickness is calculated to be 79.5 μm/1.46 = 54.5 μm. For the plastic laminator sample, from its

two fringe separation distance, its thickness is thus calculated to be 150.0 μm/1.46 = 102.7 μm. These values again do not differ much from their exact measured thickness value. From all these observation, the constructed OCT system is shown to be able to perform a meaningful one dimensional axis scan.

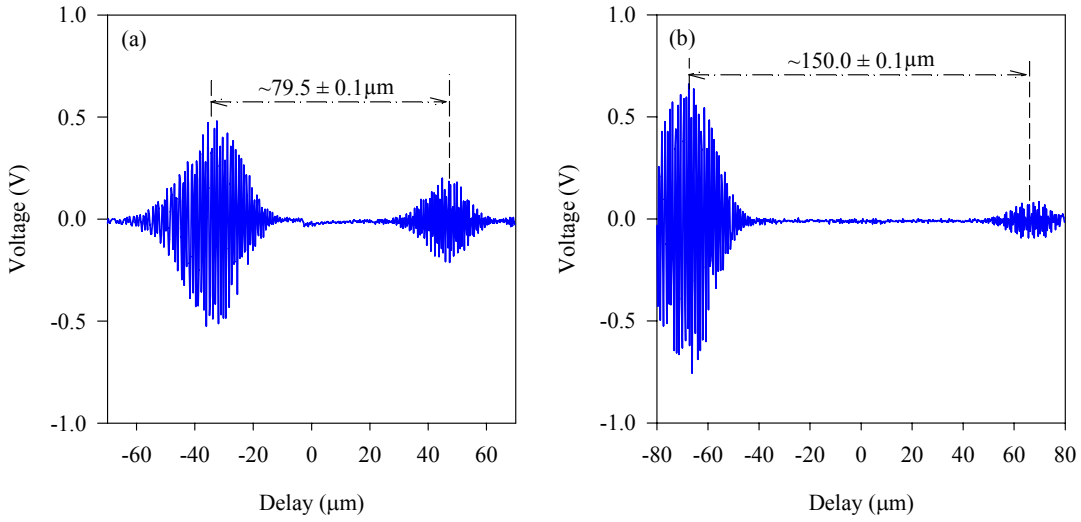

Fig. 3.6: Interference signal of (a) plastic sheet and (b) plastic laminator

3.4 Doppler Frequency Observation

The use of a reference mirror, as a delay line in OCT, is common in order to shift the coherence gate along the sample depth to achieve an interference signal. In a time-domain OCT system, the delay line will introduce a time delay, τ, at a velocity, **v**, and simultaneously generate a corresponding heterodyne frequency. The constant velocity movement of the mirror will shift the centre frequency of the interference signal to the Doppler frequency

$$f_D = \frac{2\mathbf{v}}{\lambda_c} \tag{3.1}$$

where λ_c is the source centre wavelength used. Take, for example, a mirror secured on a piezo driven stage forward scanned at 175 μm and oscillating at 1 Hz frequency, using an SOA source with FWHM spectral width of 59.10 nm, where its centre wavelength is at 1535.13 nm, the Doppler frequency, f_D, is calculated to be 455 Hz. Thus for mirror scanning at 2 Hz and 3 Hz, it will produce a Doppler frequency at 909 Hz and 1364 Hz respectively.

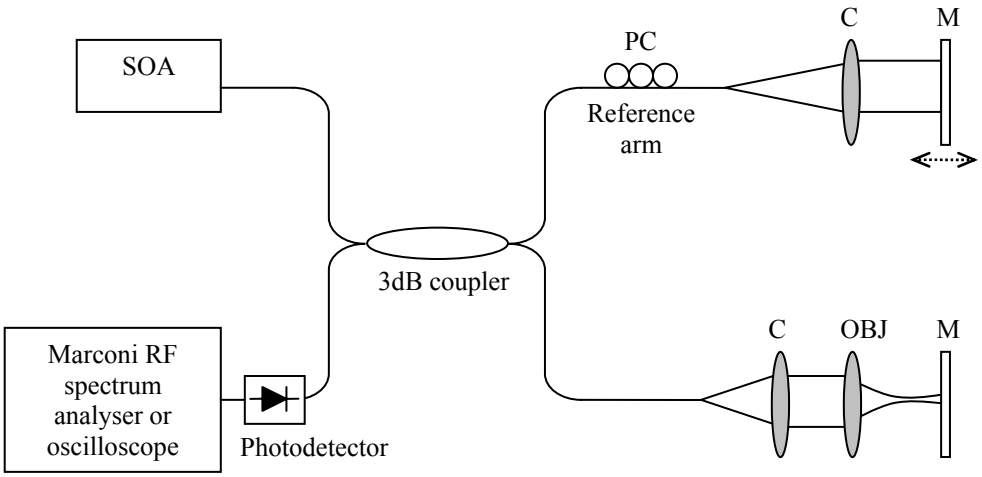

Fig. 3.7: Experimental setup for Doppler frequency measurement

Three Doppler frequency measurements were taken. Using the time-domain OCT setup in Fig. 3.7, the Doppler frequency was measured using an RF spectrum analyser (Model 2382, Marconi) and by taking a Fourier transform of the interference

signal on a oscilloscope(TDS3012B, Tektronix). The interference signal is detected using a photodetector (Model 1811, New Focus) before feeding the electrical signal into the spectrum analyser or the oscilloscope. The video bandwidth and resolution bandwidth for the spectrum analyser was maintained at 10 Hz and 30 Hz respectively. The signal attenuation into the spectrum analyser is 40 dB. Power incident on the detector was maintained at -14.80 dBm in order not to saturate it. For the piezo stage, a triangular waveform was given at three different frequencies, i.e.: 1 Hz, 2 Hz and 3 Hz. The captured RF signal from the spectrum analyser and its equivalent Fourier transform spectrum from the oscilloscope is shown in Fig. 3.8. All the three measurements on the spectrum analyser are subject to 16 times sample sweeping to smooth out the measurement and to reduce noise before being recorded.

The peak frequencies in Fig. 3.8 (a), (b) and (c) were observed at 480 Hz, 1000 Hz and 1570 Hz for the mirror scanning at 1 Hz, 2 Hz and 3 Hz respectively. The difference in the frequency value with the actual Doppler frequency is due to the turning point at which the stage is moving in the opposite direction. Even though the peaks of the frequency are still centred at the Doppler frequency as the mirror scanning rate is increased, frequency broadening is observed together with this increment. Besides that, distinct peaks appeared alongside the broaden frequency range in the spectrum analyser. Besides the Doppler frequency, the interference signal also generated other frequency components alongside it. This means that by increasing the scanning rate, the interference signal can get noisier. These evident peaks may somehow have appeared from the resonance frequency of the mirror driven by the piezo stage. In Fig. 3.8 (b), each of these peaks is a distance apart at ~50 Hz. The alternating current (AC) power line may have contributed to the peaks' appearance too. An unstable centre frequency generated from the function generator that is used to drive the piezo stage may have contributed to this frequency broadening.

For the Fourier transform spectrum, the peak frequencies in Fig. 3.8 (c), (d) and (e) were observed at 455 Hz, 935 Hz and 1440 Hz for the mirror scanning at 1 Hz, 2 Hz and 3 Hz respectively. These values do not differ much from the theoretical Doppler frequency calculated earlier. In this frequency domain, multiple harmonics are recorded along side the main Doppler frequency. This is because the number of points when the Fourier transform is performed is under sampled, an effect of aliasing.

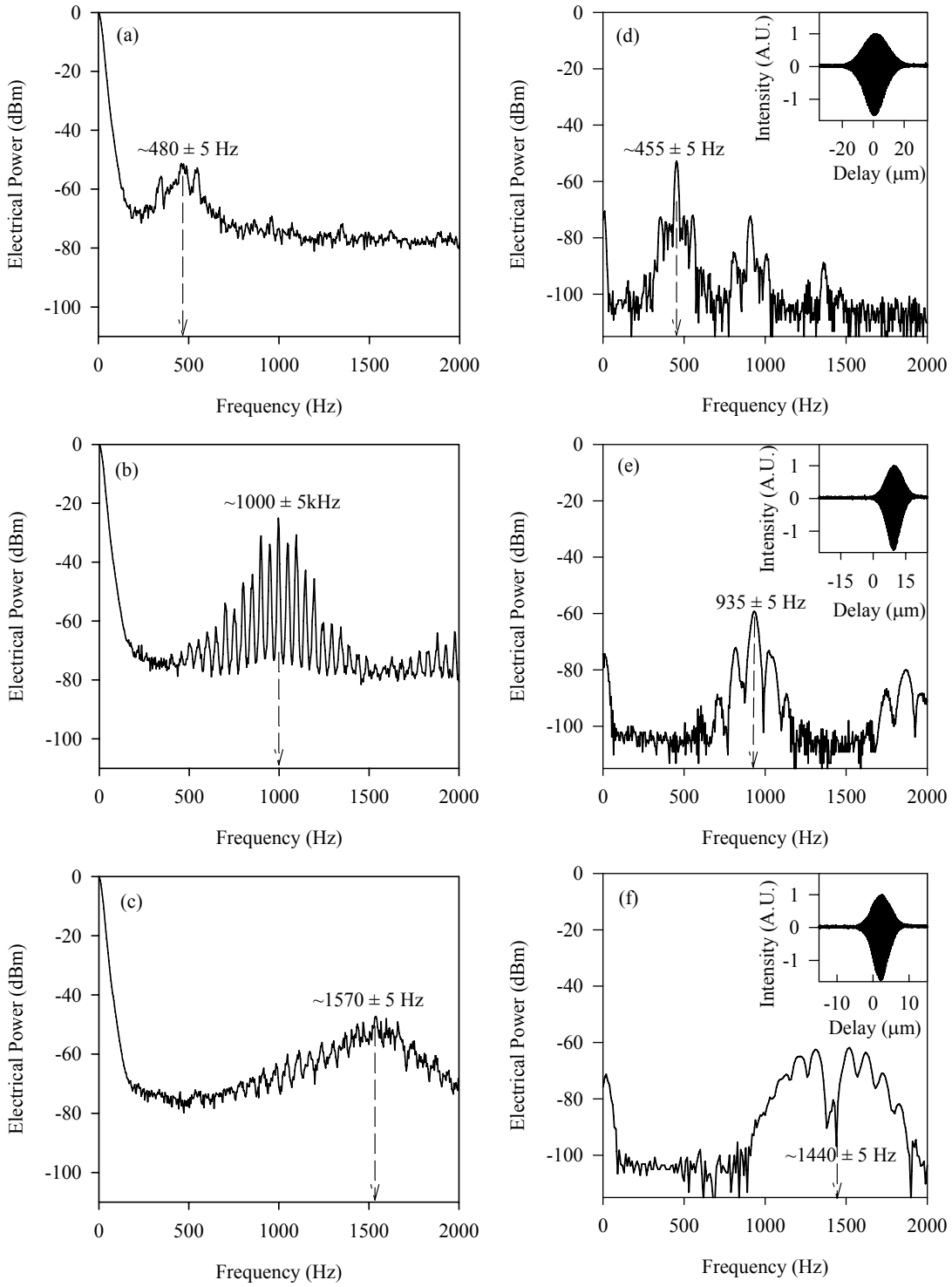

Fig. 3.8: Doppler frequency of the OCT interference signal observed using the spectrum analyser for the reference mirror driven at (a) 1 Hz (b) 2 Hz and (c) 3 Hz, and their equivalent Fourier transform spectrum (d), (e) and (f) using the oscilloscope, respectively. The corresponding interference signal at their driven frequency is shown in the inset. The Doppler frequency broadening is observed together with the increment of the driving frequency for both the spectrum analyser's capture and the oscilloscope's Fourier transform spectrum.

3.5 OCT Tomograms

The constructed time-domain OCT system is able to obtain an interference signal when both the reference and sample arms' optical path length are matched. Currently the reference arm consists of a linearly moving mirror secured on a piezo stage and driven at the rate between 1 to 3 Hz. Lateral scanning was able to move at a precise manner as the translation actuator has a displacement resolution of 1 μm. Each lateral movement has been set to 4 or 5 μm, in accordance to the beam spot size. Using the developed LABVIEW program, the OCT system is operated with the movement scheme as shown in Fig. 3.9 when scanning a sample.

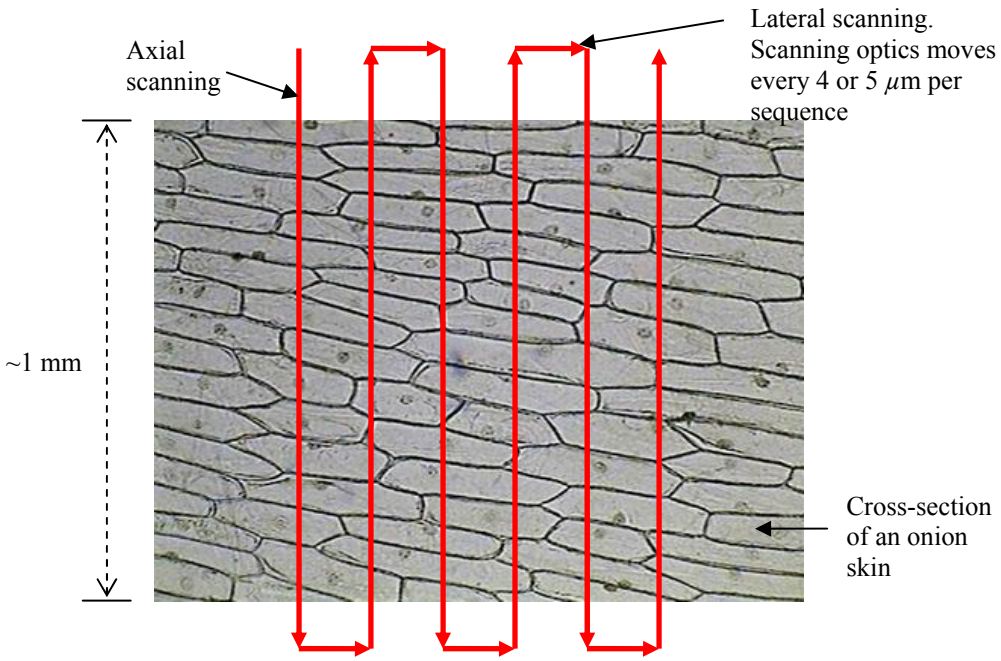

Fig. 3.9: An example of a cross-sectional OCT scan on a highly scattering sample (reproduced from [3]). The vertical arrows denote depth scanning. The horizontal arrows denote transverse scanning by moving the scanning optics

Listed in Fig. 3.10 is a preliminary OCT image obtained while scanning a flat mirror as the sample under test. A mirror is chosen because it is highly reflective and has even flatness, thus reducing the scattering. Plotted in Fig. 3.10 is the continuous stack of an envelope function from the interference signal reflected from the mirror sample. The colour legend in Fig. 3.10 is displayed in a linear scale. The OCT image of the mirror appears to be skewed instead a linear straight line. The scanning optics translation using the MM4005 actuator controller is not entirely precise because of the

introduction of error in the actuator displacement. Thus a misaligned movement was observed during the transverse scanning. Conventional OCT systems sometimes incorporate signal smoothing or averaging in order to avoid this misalignment defect. Because this OCT system has a slow scanning rate, at this early stage of development, this feature will not be embedded into the system until a faster scanning solution to this has been decided.

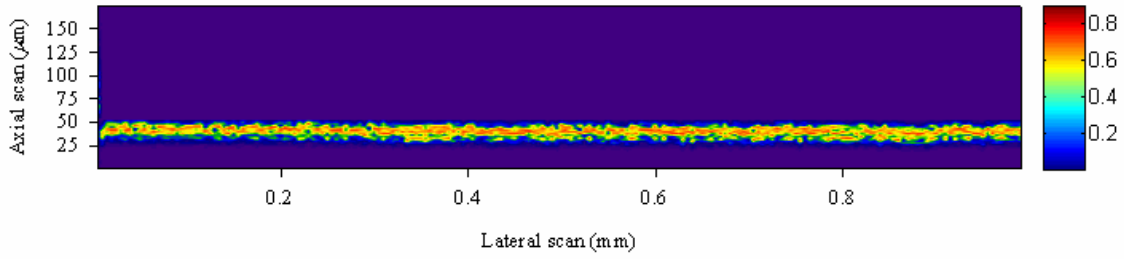

Fig. 3.10: OCT image of a mirror sample using the full spectrum of SOA source. Pixel size and resolution of the image are 200 x 512 and 5 x 0.35 μm in the transverse and axial direction, respectively

The next step in this OCT system study is to introduce a simple biological sample to be scanned. For this, an onion skin is chosen as the sample under test. Onion skin is chosen as it has a distinct cell structure that is recognisable (Fig. 3.9). When using the full bandwidth of the SOA operating at normal driving current, no interference signal is detected. This might be due to the light signal absorption by the water content in the onion and the strong scattering of light in the tissue sample. For this, the full power of the SOA is amplified at higher driving current, which significantly increases the signal power to + 4.65 dBm. The spectrum of the newly amplified SOA signal is shown in Fig. 3.11. The centre wavelength of the new spectrum is shifted to 1525.04 nm. The FWHM bandwidth of the source is slightly reduced to 57.50 nm. This new spectrum is giving an axial resolution of 17.8 μm. By increasing the source power, it is hoped that a higher backreflection signal will be obtained from the onion sample. An interference signal is obtained successfully using this new source modification.

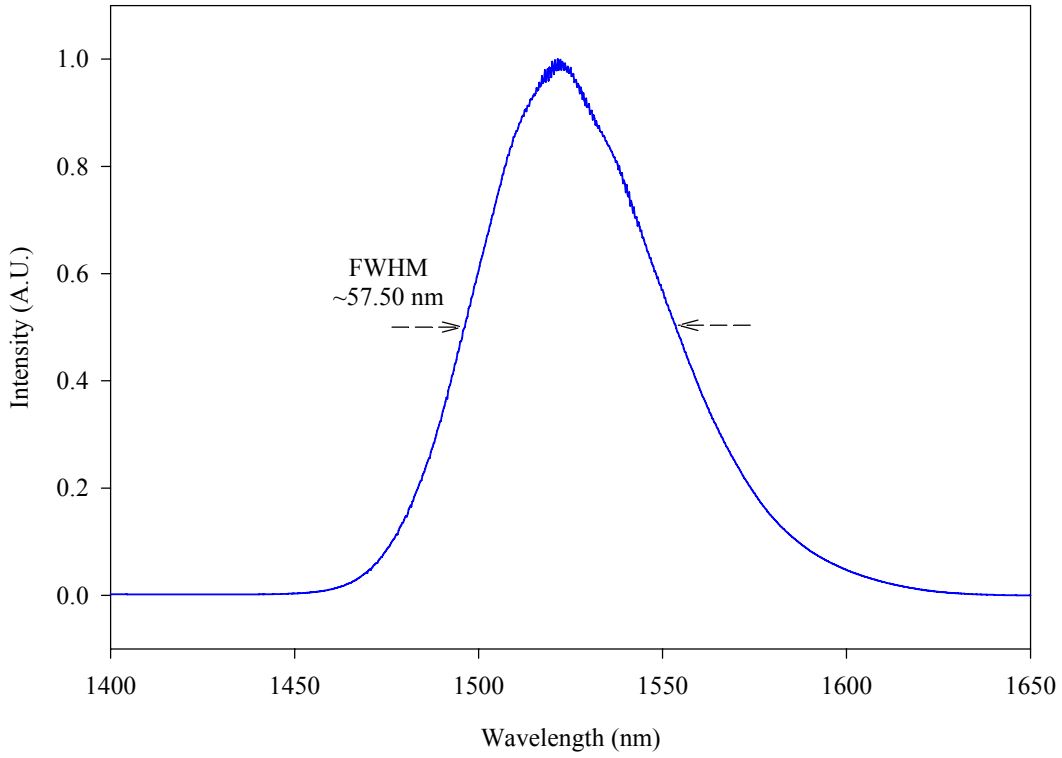

Fig. 3.11: The power spectrum of the amplified SOA signal

Fig 3.12(a) and (b) are OCT images of a section of an onion. From the optical path scan at the reference arm, the images have 175 μm in optical depth. The figures are then scaled, assuming a sample refractive index of 1.4, which gives a physical depth of approximately 125 μm. From the OCT images of the onion in Fig 3.11, the following substructure of the onion skins can be determined. The higher intensity of red colours denoted the border of the cellular structure. The hollow spaces in the middle of the cells are denoted by the blue colours.

Unfortunately, the system was not able to properly distinguish the cell structure in the onion skin as the images appeared to be distorted. Besides the earlier reason of the actuator displacement error, the limited optical power of + 4.65 dBm is not powerful enough to penetrate deeper into the sample. The penetration depth of the light signal too is limited on the onion skin surface at 125 μm. More information of the cell structure too can be covered if the scanning is performed deeper at 1 to 2 mm. Nevertheless, the utility of the OCT system was proven although further development work can be done in order to improve the overall performance of the system.

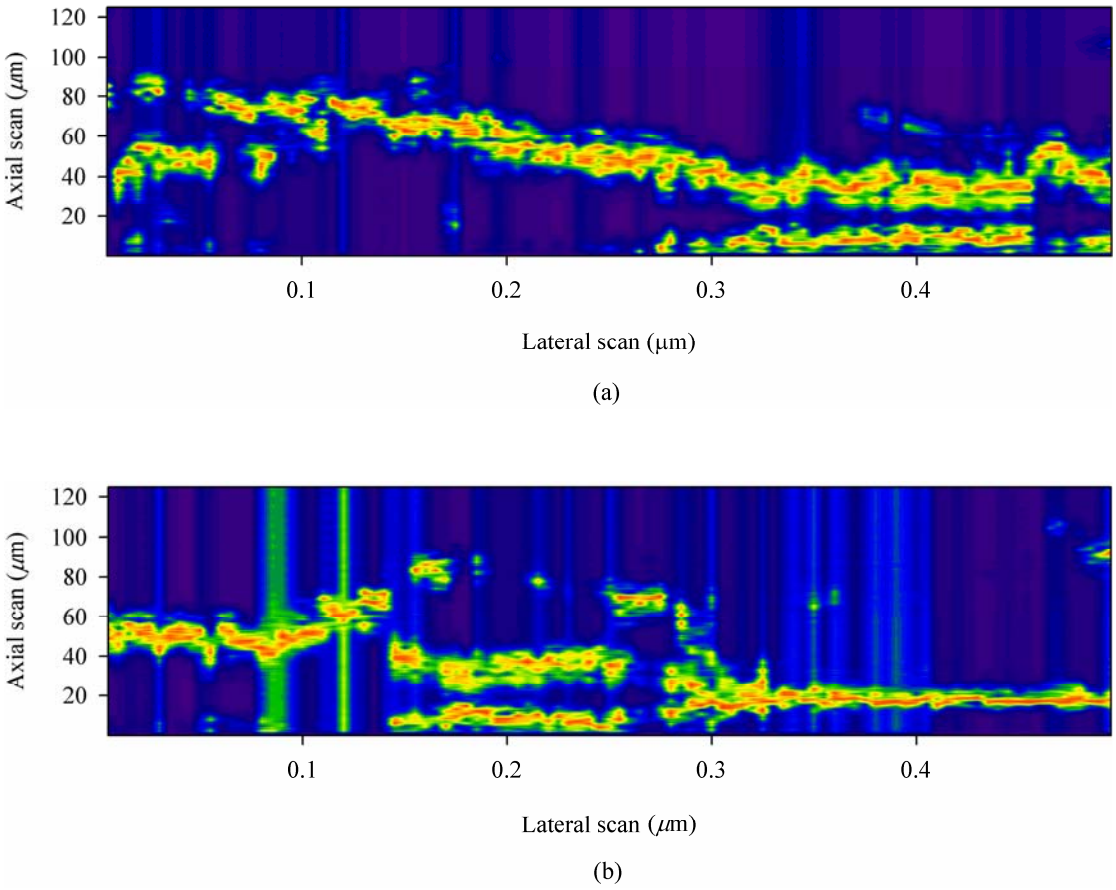

Fig. 3.12: The OCT image of an onion skin using the amplified spectrum of the SOA source. The images are scanned at two different positions on the same onion skin. Both images have the pixel size and resolution of 100 x 512 and 5 x 0.24 μm in the transverse and axial direction, respectively

3.6 Summary

In this chapter, the development and construction of a time-domain OCT system has been reported. The OCT system was able to distinguish a simple transparent sample of glass and certain plastic structures. The system has also successfully stacked and generated a simple OCT image of a mirror using the SOA broadband source. These experimental results prove the utility of the system to perform a meaningful, simple sample scan.

The limited backscattering power from the onion skin sample has prevented the system from scanning as there was no interference signal detected at first, when the SOA source was used alone. To improve it, the SOA signal was amplified, increasing the source power using higher driving current. A crude OCT image of an onion sample skin was obtain. A limited optical scanning depth of 125 μm was one of the reasons for the distorted OCT image. To compensate for this, the new all fibre optical delay line will be constructed at the reference arm, which is able to scan at a deeper penetration. This study is covered in Chapter 5 of this thesis.

3.7 References

1. J. M. Schmitt, "Optical coherence tomography (OCT): a review," IEEE Journal of Selected Topics in Quantum Electronics **5**, 1205-1215 (1999).

2. A. M. Rollins, M. D. Kulkarni, S. Yazdanfar, R. Ung-Arunyawee, and J. A. Izatt, "In vivo video rate optical coherence tomography," Optics Express **3**, 219-229 (1998).

3. W. Dioni, "Homage to the onion skin," in *Miscape*(2003).

Chapter 4

Supercontinuum Source: Performance Comparison and Noise Characterisation

4.1 Introduction

The significant difference between OCT and conventional microscopy is that OCT achieves very high axial image resolutions independent of focusing conditions, because the axial and transverse resolution are determined independently by different physical mechanisms. This implies that axial OCT resolution can be enhanced using a broad bandwidth, low coherence length light source. It is important to note that the light source not only determines axial OCT resolution via its bandwidth and central emission wavelength, but also determines both the penetration in the sample (biological tissue) and the OCT transverse resolution. A source with high output power with low-amplitude noise is necessary to achieve high sensitivity and high-speed, real-time OCT imaging. Hence it is obvious that the light source is the key technological parameter for an OCT system, and a proper choice is essential. For the OCT case, a very broadband spectrum is required and the selection of the centre wavelength is crucial to avoid the water absorption peak in biological samples. For this reason, a supercontinuum source was chosen as it has the better potential to excel as the future dominant broadband source for use in OCT systems.

A supercontinuum SC450 source unit (see Appendix B), courtesy of Fianium UK was loaned to this lab for this experimental purpose. Comparing this source with other commercial supercontinuum lasers [1, 2], this unit is small, compact, light, robust and allowed ease of handling and mobility despite its inherent features of

higher spectral density and broader bandwidth. The laser aperture output is built straight onto the PCF, which is the key ingredient to the nonlinear spectral broadening supercontinuum generation. Its collimated output provides ease of coupling and stage mounting (Fig. 4.1 (a)). Other commercial sources mostly have free space laser output, thus beam steering handling is needed. The setup of commercial Kerr lens mode-locked lasers for signal pumping is generally more complex and therefore bulky and not easy to handle. Whereas for this unit, its passively mode-locked ytterbium (Yb) fibre laser for picosecond optical pulse pumping is scaled down, comes with very minimal maintenance and low power consumption. This quasi-cw laser operates at 40 MHz repetition rate. The pump laser was set at the zero-dispersion wavelength of the PCF. The spectrum of light was broadened when the light propagates through the fibre. The output spectrum was broadened gradually as the pumping intensity increased.

Fig. 4.2 (a) reveals the output spectrum of SC450 taken at a portion of its power. This is done by taking a 4% Fresnel reflection off a glass slide before coupling it into an SMF. This explains the lower spectral flatness on top of the spectrum, which is probably due to the cut-off of power at different wavelengths in the fibre. The supercontinuum light generation was only observed from 600 to 1700 nm, due to the limited scanning range of the optical spectrum analyser (OSA).

4.2 Broadband Sources Characterisation and Comparison

The OCT imaging requires the usage of a broadband source with a low coherence property. Using readily available broadband sources in the laboratory, the loaned supercontinuum unit, SC450, will be compared against semiconductor optical amplifier (SOA) and erbium-doped fibre amplifier (EDFA) sources. SOA and EDFA sources are chosen as comparison devices because these two thermal-like sources are light sources of an incoherent nature where the light packets or photons emitted by such sources are random in phase when compared against a laser. In addition to that, these units can provide high power output, more stable and generate a small noise level in the 1550 nm spectrum.

An SOA is a device which uses semiconductor material as the gain or active medium [3]. To achieve gain, electrons are excited from the valence band to the

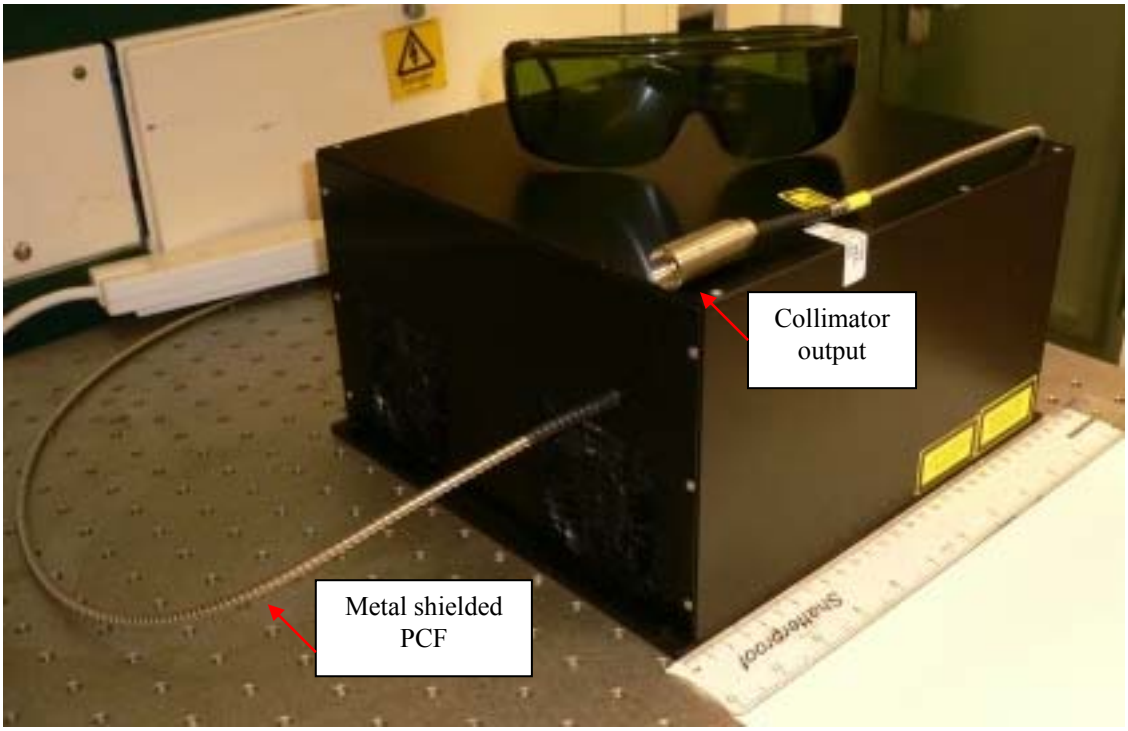

(a)

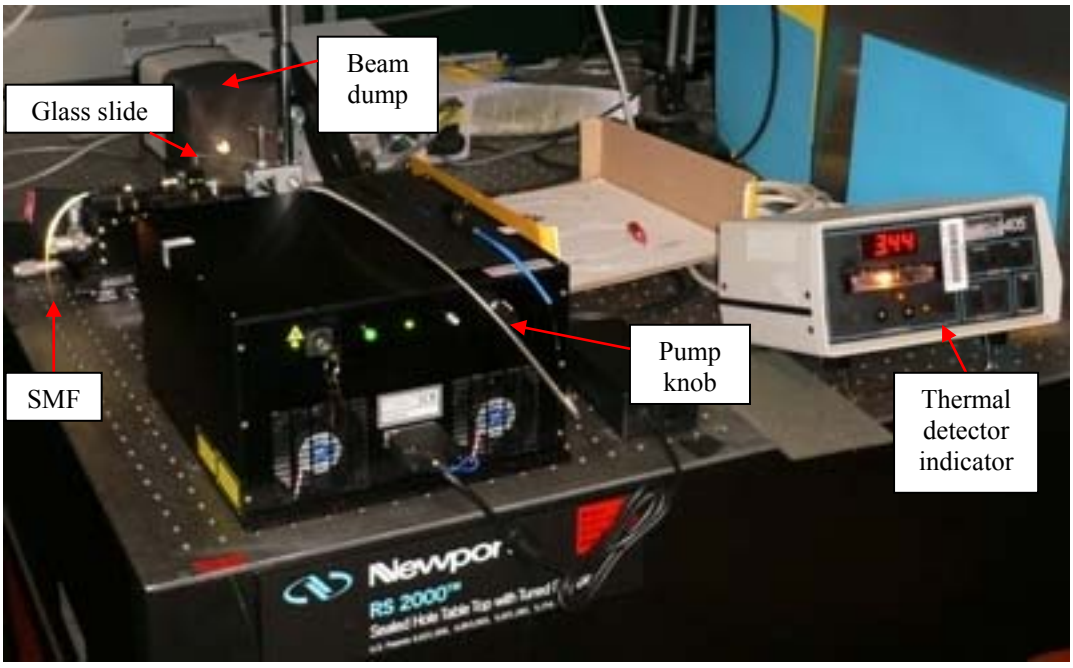

(b)

Fig. 4.1: (a) The front interface of the supercontinuum SC450 source. (b) Because the average power output from SC450 is too high, coupling of its collimated beam into SMF has to be done by taking a partial light beam reflected off a glass slide.

conduction band with electrical current. In the absence of an input signal, a certain fraction of the excited molecules or atoms will fall back to the low energy level and produce spontaneous emission photons. These photons emit in random directions and a small fraction of these photons will propagate towards the output of the amplifier. As the photons travel along the waveguide towards the output, these photons will stimulate the generation of other photons. The stimulated photons will have the same direction of propagation, frequency, phase, and polarization as the photons that caused the stimulated emission. These amplifiers have a similar structure to Fabry Perot laser diodes but with anti-reflection design elements at their end faces. SOA has the potential for practical use in optical networking due to advances in optical semiconductor fabrication techniques and design, particularly in short-haul optical transmission.

Rare-earth doped optically pumped fibres too are normally used in optical communication to amplify signals. Erbium, for example, can realize the operation around the 1550 nm wavelength, the C-band in optical communication. EDFAs have two commonly-used pumping bands – 980 nm and 1480 nm. The 980 nm band has a higher absorption cross-section and is generally used where low-noise performance is required. The absorption band is relatively narrow and so wavelength stabilised laser sources are typically needed. The 1480 nm band instead has a lower, but broader, absorption cross-section. In this study, the EDFA with a 980 nm pump wavelength is used. The 980 nm pump light is multiplexed into the erbium doped fibre where the optical signal is amplified through interaction with the doping erbium ions via the ASE process.

ASE itself is basically an amplified “noise” [3]. An EDFA can amplify not only the input field from a laser but also the spontaneous radiation emitted by the excited molecules or atoms of the amplifier itself. The EDFA is actually bidirectional, with ASE leaving from both ends. Spontaneous emission occurs over the entire length of the optical amplifier. A spontaneous emission photon that travels the whole length of the amplifier can stimulate the emission of more photons and lead to substantial output radiation at the other end of the amplifier. ASE is a “noise” [3] because it can significantly deplete the upper level population, thus diminishing the gain available to the input signal to be amplified. ASE can be expected to seriously deplete the upper-level population of the amplifying transition if it becomes comparable in magnitude to the saturation intensity of the transition.

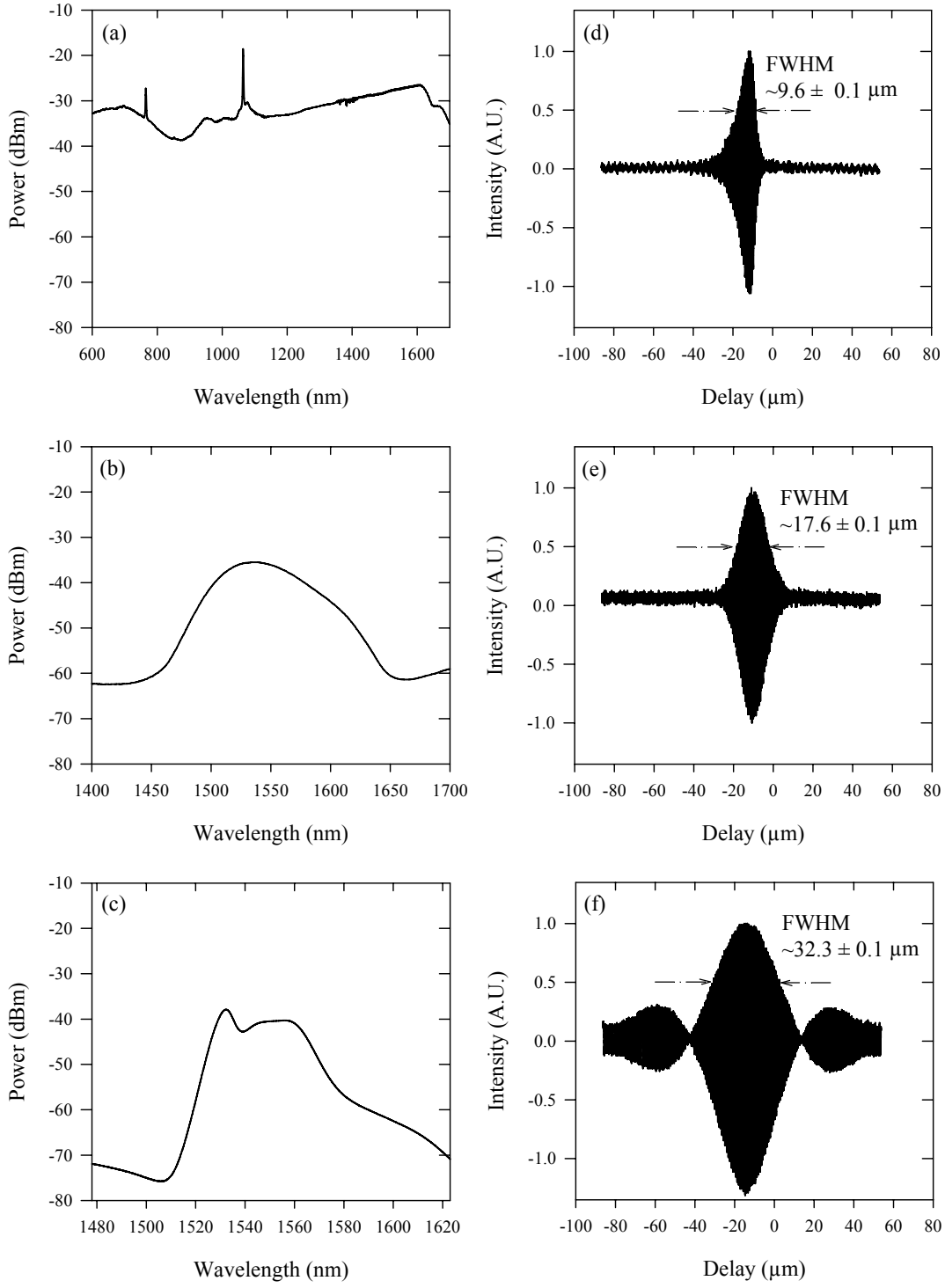

Fig. 4.2: Full spectrum of (a) SC450 (b) SOA (c) EDFA sources and their respective interference signal when launched into the OCT setup. The 3 dB bandwidths of each source are 1440.0 nm (see Appendix B for characteristics) for the SC450, 59.1 nm for the SOA and 37.0 nm for the EDFA. The optical spectrums of these sources are recorded with a 0.5 nm resolution bandwidth.

Because of the undepleted pump, the full spectrum of the SC450 in Fig. 4.2 (a) exhibited an obvious peak at 1064 nm. This corresponds to pumping by the mode-locked Yb fibre laser at the zero-dispersion wavelength of the nonlinear PCF in the SC450. No pump peak appearance is observed for the EDFA at 980 nm because the unit is backward pumped and the ASE output is observed at its front end output. It is also noticed that a second peak appears at 766 nm for the SC450. This might be contributed from the nonlinear interaction generated in the PCF. The exact nonlinear effects that contributed to this second peak are currently unknown. Generally speaking, $\chi^{(2)}$ nonlinear process does not appear in silica, a centrosymmetric material. The 1064 nm photon which is clearly distinct in this source spectrum may have interacted together along with the nonlinear process to produce this peak.

4.2.1 Interference Signal Observation

To demonstrate the application of broadband supercontinuum light from SC450 for high-resolution OCT, its interference signal was obtained and measured against the equivalent interference signal of the SOA and EDFA source. The full spectrum of each source was launched into the OCT setup to obtain their interference signal. Because of the wavelength cut-off and loss each time the supercontinuum spectrum traveled in the OCT setup, the final spectrum incident on the photodetector will be spectrally shaped, when compared to the SC450 original spectrum, as shown in Fig. 4.7. This loss is mostly attributed to the 3 dB coupler cut-off. From the 3dB bandwidth, $\Delta\lambda$ in Fig. 4.7, using Eq. 2.14, the axial resolution for the SC450 is calculated to be 4.8 μm. The measured FWHM of the interference signal in Fig. 4.2(d) is 9.6 μm, twice the magnitude of the theoretical value. The reason for the fringe broadening is because the SC450 spectrum, at this cut-off wavelength, does not exhibit partial coherence features, a prominent aspect of a thermal-like source. Similarly to the one reported in the earlier Section 3.3, the interference signal for the SOA source (Fig. 4.2 (b)) is measured to be 17.5 μm, matching its theoretical value. Because the SOA full spectrum resembled a Gaussian-like shape, its interference signal too fits a Gaussian-like shape. The interference signal for the EDFA source, in Fig. 4.2 (f), resembles a sinc function shape, where side lobes appeared along side the main lobe. The reason for this side lobes appearance is because the full spectrum of the EDFA resembles a flat top shape. The FWHM recorded for the main lobe is 32.3 μm. This value does not correspond with the theoretical FWHM value of Gaussian shape spectrum (Eq. 2.14), but instead fits well with the general sinc shape equation, given by Eq. 4.2.

Fig. 4.3 shows the experimental setup that is used to filter the broadband sources by taking the reflectivity profile of a linearly chirped fibre Bragg grating (CFBG). Here the effects of shaping the sources' spectra are compared with their obtained interference signal. Two CFBG are used, i.e.: the flat top and Gaussian shaped filters. The broadband source is optically filtered with the CFBG using the 3 port circulator configuration. The flat top grating is 140 mm long and reflecting ~40 nm bandwidth at the centre Bragg wavelength of 1550 nm with 63% reflectivity. The Gaussian grating is 130 mm long and reflecting ~23 nm bandwidth at the centre wavelength of 1545 nm with 70% reflectivity. The end of the CFBG is immersed in

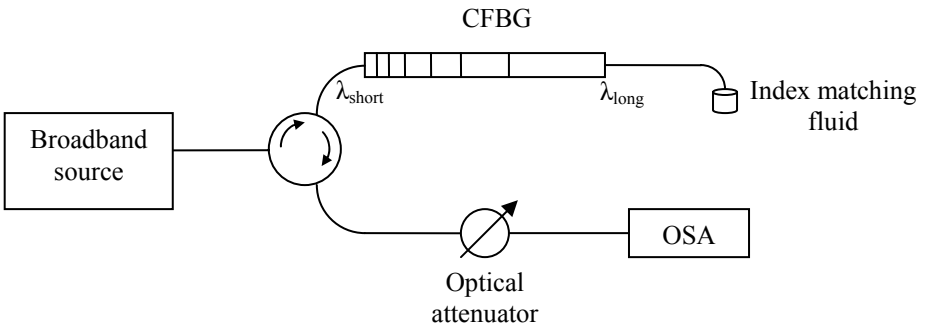

Fig. 4.3: Schematic diagram of signal shaping setup using CFBG for spectral and interference signal characterization.

index matching fluid to prevent the backreflection signal. For all sources, optical power of -15 dB was maintained, using the 1550 nm optical attenuator, before feeding the signal into the OSA. The filtered spectrum for each broadband source is listed in Fig. 4.5 and Fig. 4.6.

Then, modifying the experimental setup in Fig. 4.3, the filtered broadband signals are reused by launching them into the OCT setup, as depicted in Fig. 4.4, to obtain their interference signal. Using the two earlier CFBGs with different shaping, their interference signals using these three broadband sources was characterized, as listed in Fig 4.5 and Fig. 4.6.

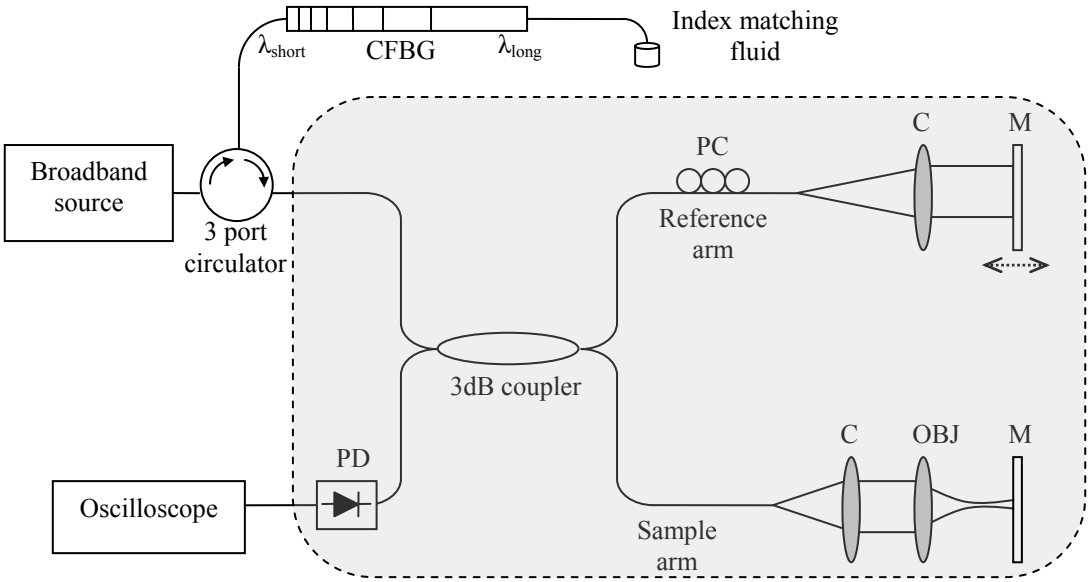

Fig. 4.4: Interference signal characterization of the broadband sources using the two different optically filtered spectral shapes. The OCT system is highlighted in the shaded box.

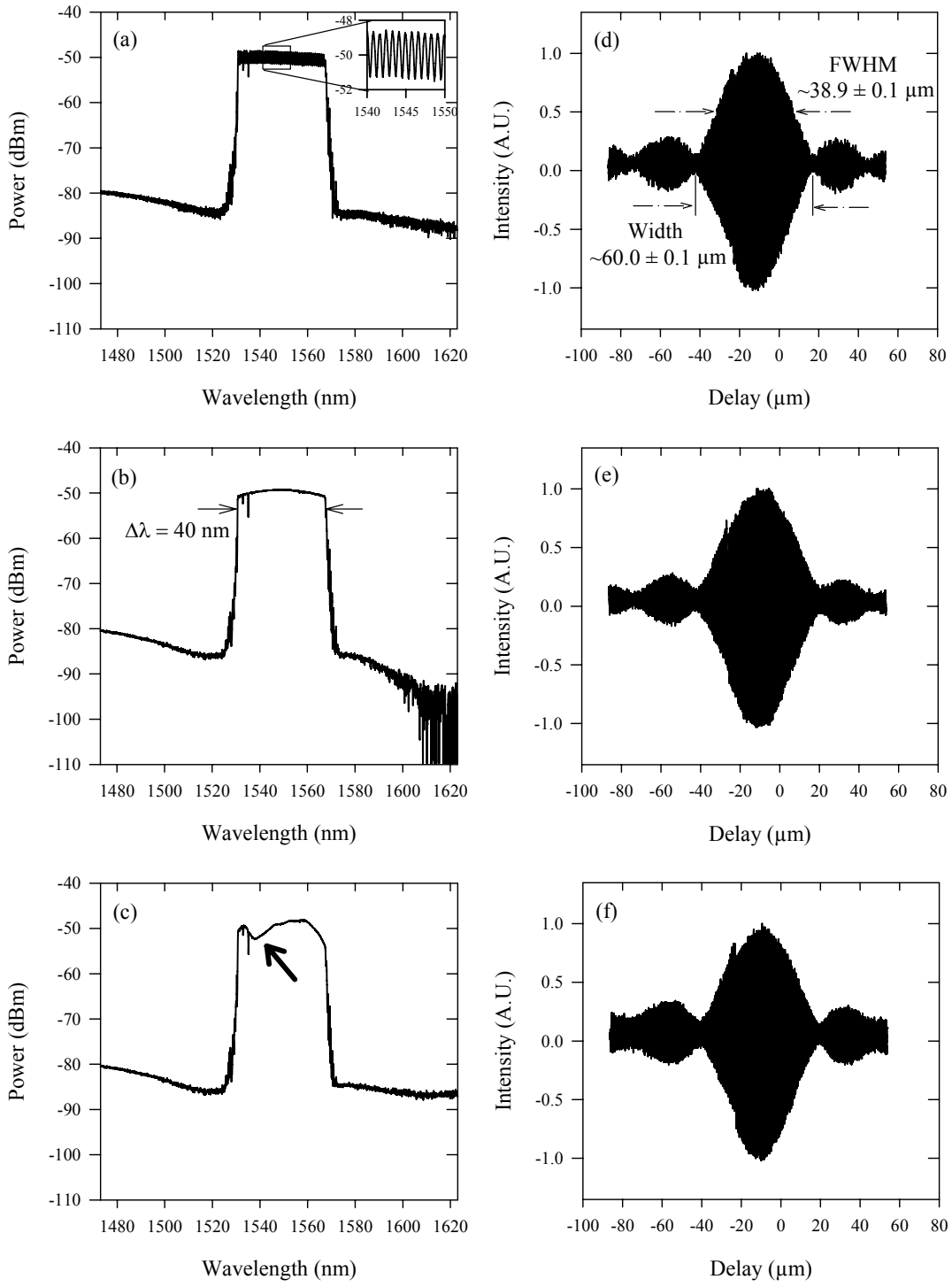

Fig. 4.5: The filtered spectra of (a) SC450 (b) SOA and (c) EDFA sources using a flat top shaped CFBG and their respective sinc shaped function interference signals. *Inset*: (a) Enlarged spectral modulation on top of the top hat spectrum. (c) Small arrow denotes the small dip in spectrum. The filtered optical spectrums are from the OSA with a 0.01 nm resolution bandwidth.

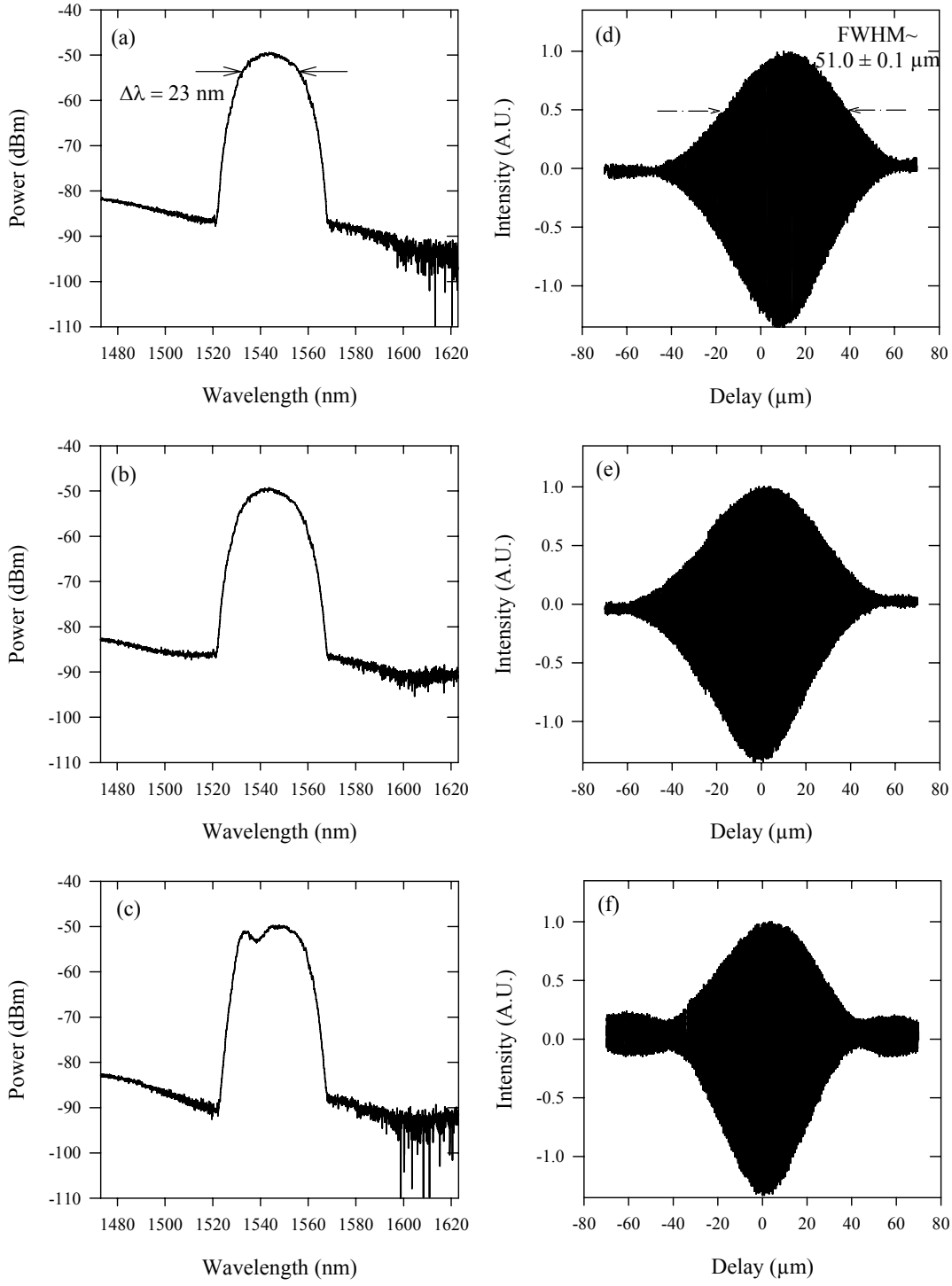

Fig. 4.6: The filtered spectra of (a) SC450 (b) SOA and (c) EDFA sources using a Gaussian shaped CFBG and their respective Gaussian shaped function interference signals. The filtered optical spectrums are from the OSA with a 0.01 nm resolution bandwidth.

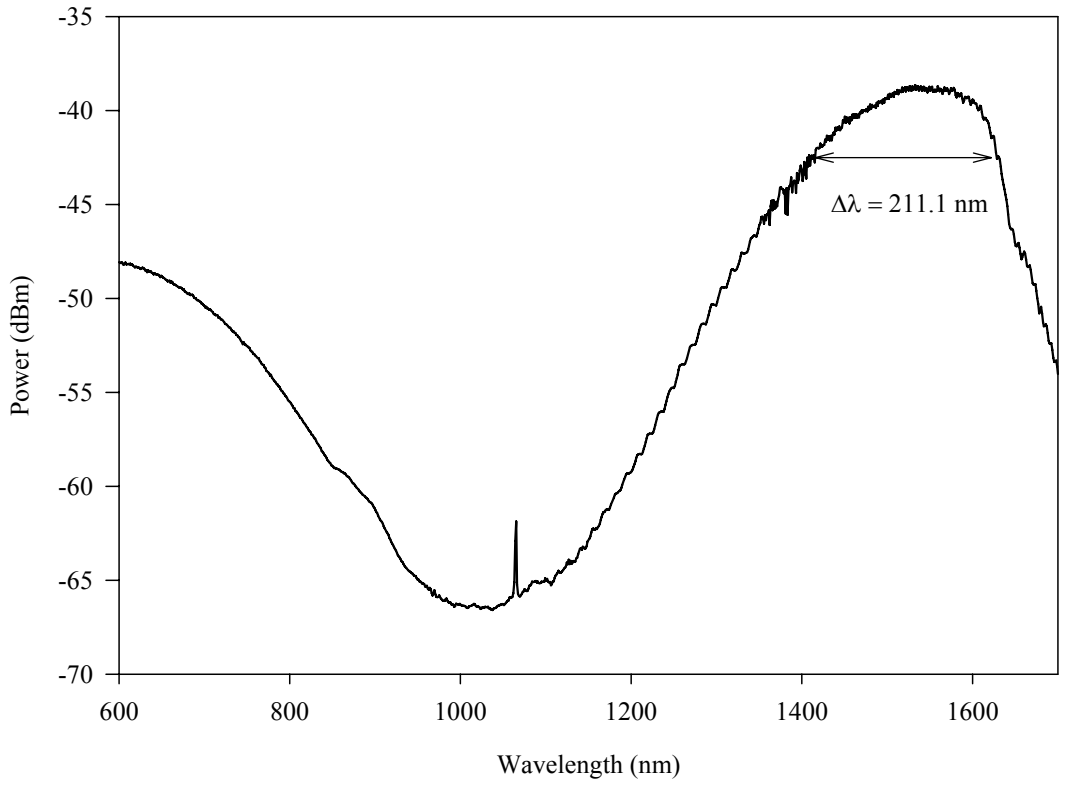

Fig. 4.7: The SC450 spectrum that is incident on the photodetector after coupling from the OCT coupler. This optical spectrum is recorded with a 0.5 nm resolution bandwidth.

For the flat top filtered SC450 spectrum, there is a periodic wavelength oscillation in this 1550 nm wavelength region, as shown in the inset of Fig. 4.5 (a). The SC450 source is emitting a very broad bandwidth of more than 1300 nm. Hence there will be interference of modes when it is coupled into optical fibre from its collimator output. The induced intermodal interference will cause mode competition at the end of the fibre where two or more wavelengths may be experiencing constructive interference [4]. To prevent this, a better beam coupling method was used to ensure that a proper beam profile was coupled into the fibre core. Therefore, no mode interference is observed in Fig. 4.6 (a) during the Gaussian shaped filter experiment.

For both the flat top and the Gaussian filtered SC450 spectrum, the FWHM of their interference signals, were 38.9 μm and 51.0 μm respectively. The same values were obtained for SOA and EDFA filtered sources. Due to uneven fringe symmetry, the correct FWHM measurements for Gaussian filtered sources were obtained from the envelope function of their interference signal in Fig. 4.6. For the flat top filtered

spectrum, the width of its main lobe is 60.0 μm. At their equivalent time value, the main lobe width and the FWHM of the sinc-shaped interference signal conform to the sinc-shape general equation given by Eq. 4.2. Bigger sidelobes appeared for the EDFA filtered interference signal (Fig. 4.5 (f) and Fig. 4.6 (f)) because of a small dip in the spectral shape at the 1535 nm region which moderately shaped the spectrum. The theoretical axial resolution for the Gaussian shaped spectrum is 49.0 μm, which does not differ much from the measured FWHM of the interference signal at 51.0 μm. The Gaussian shaped spectra conform to their theoretical axial resolution, as Eq. 2.14 can only be applied to a Gaussian shaped spectrum.

4.2.2 Effects of Optical Filters Shaping to Its Coherence Function

The sinc shaped functions in Fig. 4.5 (d), (e) and (f) are actually the Fourier transform of the filtered spectrum in Fig. 4.5 (a), (b) and (c), respectively. The common sinc function; sinc(θ) = sin ($\pi\theta$) / $\pi\theta$ satisfies the interference signal shape in Fig. 4.5 (d), (e) and (f).

The Fourier transform of a rectangular pulse in Fig. 4.8 (a) is a sinc function (Fig. 4.8 (b)) as denoted by the following relationship

$$\mathbf{x_1(t)} = \begin{cases} 1, & |t| < T_1 \\ 0, & |t| > T_1 \end{cases} \quad \overset{F}{\longleftrightarrow} \quad \mathbf{X_1(\omega)} = \int_{-T_1}^{T_1} e^{-j\omega t} dt = 2\frac{\sin \omega T_1}{\omega}. \tag{4.1}$$

Now consider the signal with the Fourier transform in Fig. 4.8 (d) and its inverse (Fig. 4.8 (c)), as revealed in the following relationship

$$\mathbf{X_2(\omega)} = \begin{cases} 1, & |\omega| < W \\ 0, & |\omega| > W \end{cases} \quad \overset{F}{\longleftrightarrow} \quad \mathbf{x_2(t)} = \int_{-W}^{W} e^{j\omega t} d\omega = \frac{\sin Wt}{\pi t}. \tag{4.2}$$

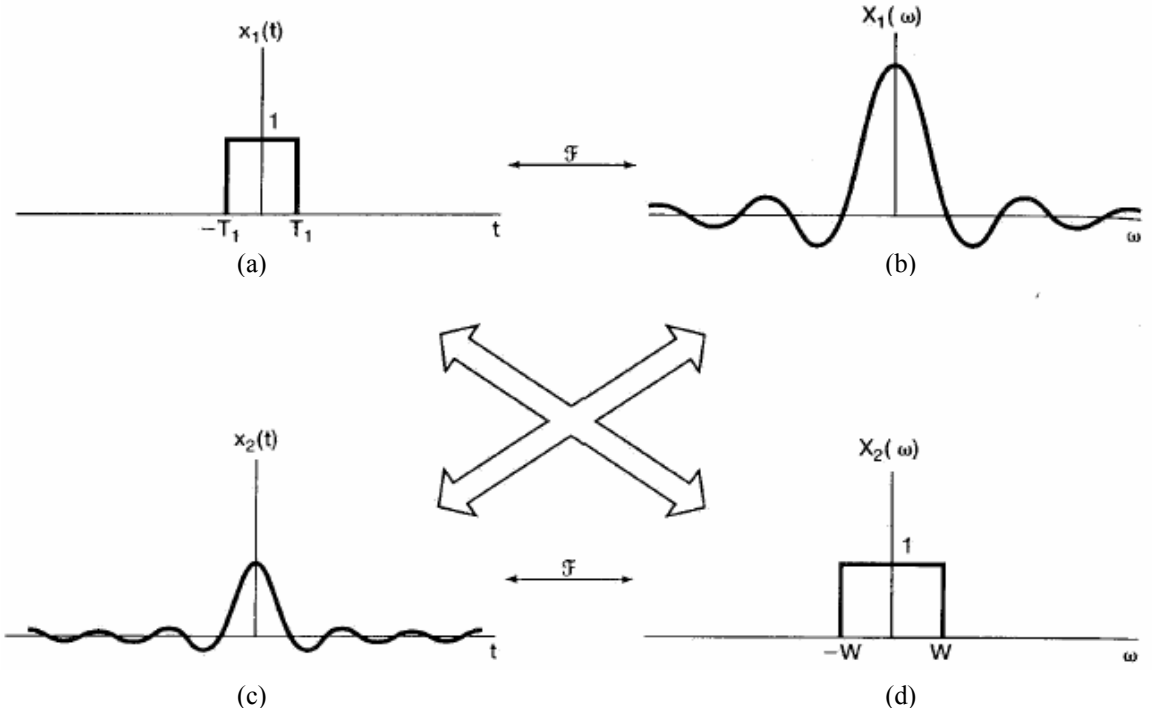

Fig. 4.8: Duality property of Fourier transform.

This is the consequence of the duality property of the Fourier transform.

By comparing the Fourier transform and its inverse transform relations,

$$x(t) = \frac{1}{2\pi}\int_{-\infty}^{+\infty} X(\omega) e^{j\omega t} d\omega \tag{4.3}$$

$$X(\omega) = \int_{-\infty}^{+\infty} x(t) e^{-j\omega t} dt \tag{4.4}$$

it is noticed that the equations are similar in form but not quite identical. This symmetry was also noticed in Eq. 4.1 and Eq. 4.2, i.e. the transform of the flat top function was the sinc function and vice versa.

A Gaussian is an example of a self reciprocal function, in other words, both the function and its transform have the same form (Fig. 4.9)

$$\mathbf{x(t)} = \exp(-\pi t^2) \quad \overset{F}{\longleftrightarrow} \quad \mathbf{X(\omega)} = \int_{-\infty}^{\infty} e^{(-\pi t^2)} e^{-j\omega t} dt = \exp(-\pi\omega^2)\,. \tag{4.5}$$

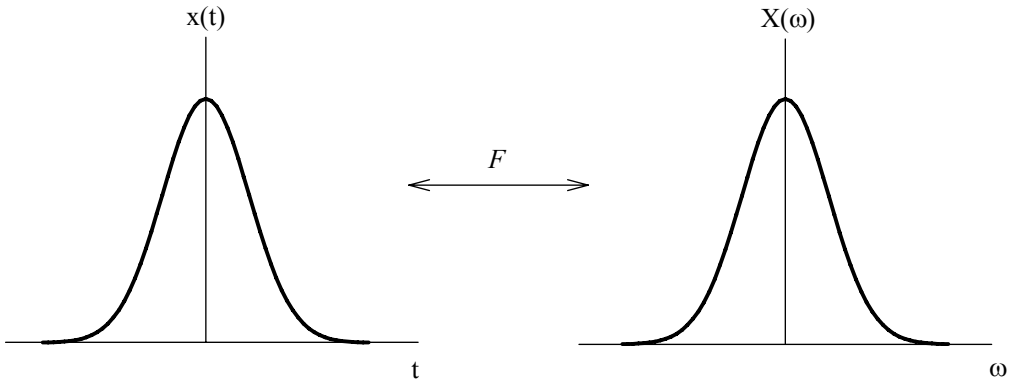

Fig. 4.9: Fourier transform of a Gaussian.

In OCT applications, a Gaussian signal is preferred in order to prevent the sidelobes appearing in the interference signal. A Fourier transform of a Gaussian is another Gaussian and vice versa. Thus using a Gaussian-like spectrum from the broadband source, the interference signal will be a Gaussian too.

4.3 Relative Intensity Noise Measurement

Unfortunately, the supercontinuum unit, SC450 suffers from noise beating, largely contributed from its intensity noise. The noise associated with supercontinuum generation, depending on the input pulse parameters, can lead to 50% intensity fluctuations. As pointed out by Corwin *et al.* [5] and Newbury *et al.* [6], the origin of this noise is the nonlinear amplification of quantum fluctuations, both in the input laser light and in the Raman scattering process within the PCF. This noise is attributed to two distinct components: low frequency (<1 MHz) noise in the supercontinuum generation is an amplified version of the amplitude noise of the pump source and a broadband component originating from nonlinear amplification of quantum fluctuations in both the input laser light and in the Raman scattered light. The Raman scattering here only plays a relatively minor role as compared to input shot noise from the pump. Numerically these authors simulated the above noise contributions using the generalised nonlinear Schrödinger equation and found that when only Raman scattering is included, the RIN is reduced by ~20 dB. But, when only the shot-noise is included, the RIN is reduced by less than ~1 dB. For this reason, it is interesting to study the contribution of the shot-noise from the pump towards the intensity noise of SC450 supercontinuum source.

Generally, noise is known to vary as a function of optical intensity, electrical frequency, chromatic dispersion, the source bandwidth and its spectral shape that is incident on the photodetector [7]. The noise incident on the photodetector normally results from the shot, thermal and intensity noise components.

Shot noise is produced by the random nature of photons arriving at the detector. For the PIN photodiode, the shot noise power, in a one Hz bandwidth, is given by

$$N_{shot} = 2qI_{dc}R_L \,. \tag{4.6}$$

Here I_{dc} is the average current, q and R_L are the electron charge and detector load resistance respectively.

Thermal noise on the other hand, is produced by the random thermal motion of electrons in the load resistor. The existence of this noise can limit the sensitivity of the detector. Its power spectral density (PSD), N_{th} can be described by

$$N_{th} = 4k_B T \tag{4.7}$$

where k_B is the Boltzmann constant and T is the absolute temperature.

The total system noise, N_T at the detector output is the summation of these two noise sources and the source intensity noise, N_{source}

$$N_T = N_{source} + N_{shot} + N_{th}. \tag{4.8}$$

The noise of interest in this study is the intensity noise, N_{source}, which refers to the noise generated by the source itself. This noise is caused by the intensity fluctuations due to the laser's structural parameters such as the physical nature of the PCF or its pump laser in the SC450 case.

The noise of a broadband source can also be parameterized as the relative intensity noise (RIN) on the photodetector. RIN measurement describes the source's maximum available amplitude range for signal modulation. It also serves as a quality indicator of laser devices. RIN is the ratio of noise power spectral density or the mean-square optical intensity noise $\left\langle \Delta P^2 \right\rangle$ fluctuation (in a one Hz bandwidth) to the square of the total average power, P

$$RIN = \frac{\left\langle \Delta P^2 \right\rangle}{P^2} \text{ Hz}^{-1}. \tag{4.9}$$

RIN is essentially a dynamic range measurement. If the average power is reduced, the RIN measurement range is reduced. Thus the thermal noise limitation can be overcome when the average power is large enough.

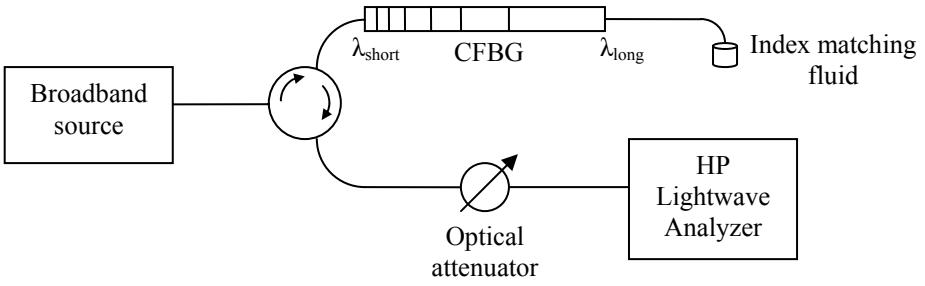

Fig. 4.10: Experimental setup for RIN measurement.

In order to characterize the intensity noise of SC450, the experimental setup presented in Fig. 4.10 was constructed. At the same time the noise intensity of SOA and EDFA sources too are measured. These two light sources are known to be stable and, most importantly, suit the low noise criteria for comparison with the SC450. These two units were chosen to be the benchmark for comparison with SC450. The optical signal from each of the broadband sources was filtered before launching into the lightwave analyser (HP71400C, Agilent). Two different CFBG filters were used, i.e.: flat top and Gaussian shaped filter, similar to the ones reported in the earlier Section 4.2.1. Thus the RIN values of these sources were compared as a function of their spectral shape. An optical attenuator was used to maintain the same -15 dBm optical power into the lightwave analyser's internal, built-in, photodetector during the measurement. The lightwave analyser has a 22 GHz bandwidth. The resolution and video bandwidth of the lightwave analyser were set at 1 MHz and 100 kHz respectively. The electrical signal attenuation is set at 0 dB and the measurements are subject to 32 times sample averaging to smooth out the result reading. The trace data is obtained in the 1 MHz – 1 GHz frequency regime. The trace data downloaded from the lightwave analyser of each filtered sources is summarised in Table 4.1.

A quick check using the HP polarisation analyser (HP 8509B, Agilent) revealed that the Gaussian filtered SC450 source is polarised with the degree of polarisation of 82.5 %, when the filtered spectrum is launched into the unit. The full bandwidth unpolarised SC450 light suffers induced polarisation effects upon filtering and cut-off of wavelength, together with loss, upon incidence on the built-in photodetector in the polarisation analyser. This high degree of polarisation is known to introduce at least a factor of 2 in the RIN measurement of a light source [8], compared with that of unpolarised light. For polarised light, the electric field vector of the light's electromagnetic field can be arbitrarily divided into two perpendicular

components, where both are traveling in phase along its direction of propagation. Hence most of the energy will be confined in this vector. This thus gives rise to the factor of 2 increase in the intensity noise of the light source. No polarisation effect was observed for SOA and EDFA.

For comparison, the measured and predicted value of RIN for each of the filtered sources is summarized in Table 4.2. Recall that RIN value is the ratio of the noise power spectral density (PSD) of the spectrum to the square of the average power. For unpolarised thermal light, the RIN at the desired frequency, f, of interest, is given by this expression [8]:

$$R(f) = \int_0^\infty \frac{S(\upsilon)S(\upsilon + f)}{P^2} d\upsilon \tag{4.10}$$

where $S(\upsilon)$ is the noise PSD as measured by the OSA and P is the total optical power in the spectrum. From Eq. 4.10, a MATLAB program was written to evaluate each source's RIN value and the results were compared with the measured RIN value. The integral is implemented in a summation model. This approximation is only true provided that the light source is a true thermal light source. With help from Dr. Anoma McCoy with the modelling, the RIN value for the filtered SOA and EDFA spectrum was predicted and is quoted in Table 4.2.

For this evaluation, 500 MHz was chosen because, at this frequency, the marker point in the screen dump stays safely at the signal base and, for the SC450 case, it does not overlap at the spike peak which later can contribute to a wrong RIN measurement. The presence of $1/f$ noise in the source output can impose a maximum achievable signal-to-noise ratio in detection sensitivity. In a wide range of carrier transfer processes, the power spectrum, which is inversely proportional to frequency, diverges at low frequencies [9]. This is observed in the noise spectrum where the low-frequency end will exhibit a different slope. The selection of the 500 MHz marker too is influenced by this condition. It is selected because it is positioned far away from the low-frequency end.

The RIN values for the SC450, SOA and EDFA filtered signal are obtained from the "RIN (Laser)" caption in their respective screen dumps in Table 4.1 and are summarised in Table 4.2. The equivalent RMS power is listed as figures enclosed in brackets in Table 4.2. From the Table 4.2, the measured RIN values for the SOA and

EDFA sources filtered with a flat top filter are in good agreement with the predicted RIN value. Their measured RIN values have repeatability within ± 0.25 dB tolerance each time the measurement is performed. For the flat top filtered source, the RIN value for the EDFA source is slightly higher than for the SOA source because of a small dip in the spectral shape at the 1535 nm region (Fig. 4.5 (c)). The opposite was observed for the Gaussian filtered source. The RIN value for the SOA is instead higher because the FWHM bandwidth of its Gaussian filtered shape is smaller than the FWHM bandwidth of the Gaussian filtered EDFA source (Fig. 4.6). The RIN values for light sources are generally higher when measured for the Gaussian spectral shape because of their steep roll over [7] as compared to the flat top spectral shape.

Table 4.1: RIN measurement on a HP71400C Lightwave Analyser for SC450, SOA and EDFA sources in the 1MHz – 1GHz frequency regime

Source	Flat top filter (40 nm bandwidth)	Gaussian filter (23 nm bandwidth)
SC450	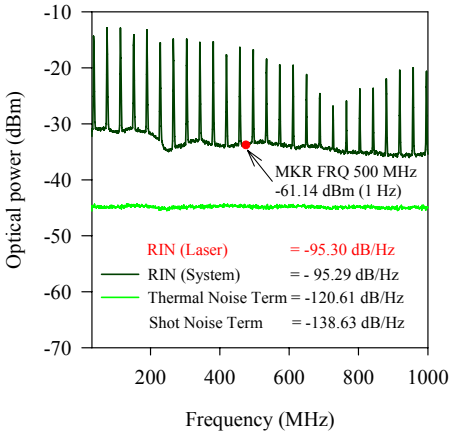	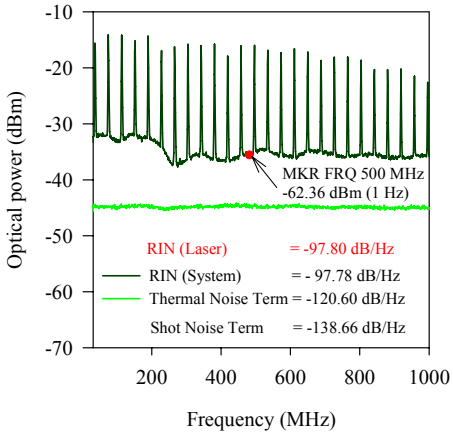
SOA	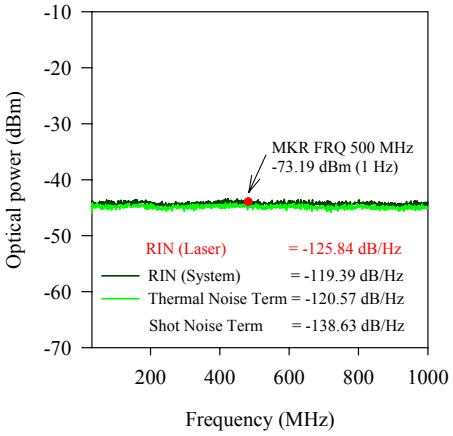	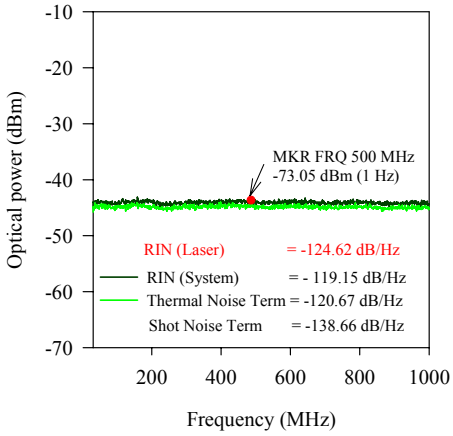
EDFA	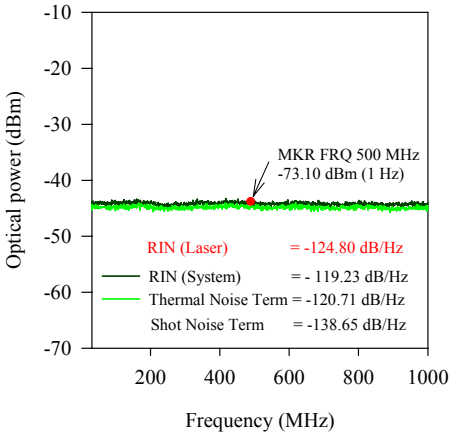	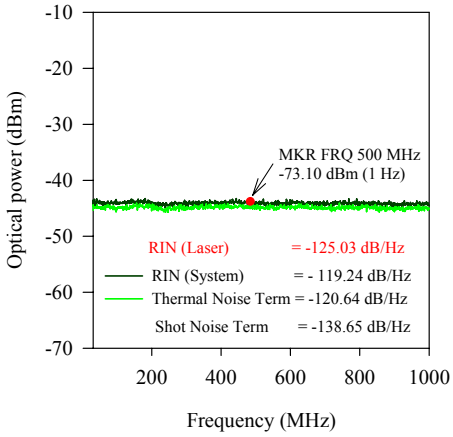

Table 4.2: Measured and predicted RIN for SC450, SOA and EDFA sources

Source	Flat top filter (dB/Hz)		Gaussian filter (dB/Hz)	
	Measured	Predicted	Measured	Predicted
SC450	-95.30 (2.9512×10^{-10} Hz^{-1})	N.A.	-97.80 (1.6596×10^{-10} Hz^{-1})	N.A.
SOA	-125.84 (2.6062×10^{-13} Hz^{-1})	-126.6	-124.62 (3.4514×10^{-13} Hz^{-1})	-125.31
EDFA	-124.80 (3.3113×10^{-13} Hz^{-1})	-126.2	-125.03 (3.1405×10^{-13} Hz^{-1})	-125.56

For the SC450 source, it is noticed that a spike peak is observed at every 40 MHz, in Table 4.1, which corresponds to the repetition rate of this pulsed pumped broadband source. Take note that the RIN value measured for SC450 was higher in magnitude compared to the SOA and EDFA, for both the flat top and Gaussian filter. The flat top filtered SC450 produced a power fluctuation of ~30.54 dB and ~29.50 dB times higher than the SOA and EDFA, respectively. For the Gaussian filtered spectrum, SC450 produced a power fluctuation of ~26.82 dB and ~27.23 dB times higher than the SOA and EDFA, respectively. This increase resulted from two combining factors. In addition to the earlier factor of 2 increment in intensity noise from a polarised signal, the nonlinear amplification of the intensity noise in the SC450 input pumping laser, due to the complex nonlinear phenomena that include SPM, FWM and SRS, are contributing to this higher RIN reading. Unfortunately the measured RIN values for SC450 are not in the vicinity of the thermal-like source's predicted value, hence 'N.A' is written in Table 4.2. This can be attributed to the same reasons as mentioned before. The predicted RIN value can only be achieved if the source is a purely thermal-like source. Thus, it can be concluded that SC450 is not a thermal light source.

Nevertheless, in terms of the OCT application, the source can still be utilized as a potential candidate. Even though, in terms of power variation, SC450 seems to be noisier, its interference signal in Fig. 4.2 (d), Fig. 4.5 (d) and Fig. 4.6 (d) appeared to be stable enough to provide good axial resolution for OCT applications.

4.4 Summary

The utility and usability of a SC450 supercontinuum source for OCT applications has been covered in this chapter. The interference signal of the SC450 has been compared with the interference signal of the SOA and EDFA. Their fringe shapes were compared at their full spectrum, flat top and Gaussian filtered spectrum. The filtered shapes correspond well with their Fourier transform shapes at their interference signal; flat top will give a sinc shape function while Gaussian will give a Gaussian shape function. At their Gaussian filtered shape, the interference signals conform well with the coherence length theoretical values.

The RIN values for the broadband sources have been compared too. Again, the RIN value has been compared for their flat top and Gaussian filtered spectrum. Generally, SC450 gives a higher RIN value; hence it is noisier when compared with the SOA's and EDFA's. At their flat top filtered spectrum, the EDFA's RIN value is higher than SOA's. But for Gaussian filtered spectrum, the SOA's RIN value is higher than EDFA's. The predicted RIN value for both flat top and Gaussian filtered, SOA and EDFA sources matched well with their measured RIN value.

It can be concluded that, even though the SC450 source is noisier in terms of power fluctuation or RIN value, when compared with SOA's and EDFA's, at least its source signal showed a stable shape throughout the characterization of its interference signal. This at least can guarantee a very functional usage for OCT applications.

4.5 References

1. http://www.koheras.com.
2. http://www.precisionphotonics.com.
3. D. Derickson, *Fiber Optic Test and Measurement* (Prentice Hall PTR, Upper Saddle River, New Jersey, 1998).
4. I. Turek, I. Martincek, and R. Stransky, "Interference of modes in optical fibers," Optical Engineering **39**, 1304-1309 (2000).
5. K. L. Corwin, N. R. Newbury, J. M. Dudley, S. Coen, S. A. Diddams, B. R. Washburn, K. Weber, and R. S. Windeler, "Fundamental amplitude noise limitations to supercontinuum spectra generated in a microstructured fiber," Applied Physics B: Lasers and Optics **77**, 269-277 (2003).
6. N. R. Newbury, B. R. Washburn, K. L. Corwin, and R. S. Windeler, "Noise amplification during supercontinuum generation in microstructure fiber," Optics Letters **28**, 944-946 (2003).
7. A. D. McCoy, "Intensity Noise Suppression Using a Semiconductor Optical Amplifier: Characterisations and Applications," in *Ph.D Thesis, Optoelectronics Research Centre*(University of Southampton, Southampton, 2005).
8. G. E. Obarski, and J. D. Splett, "Transfer standard for the spectral density of relative intensity noise of optical fiber sources near 1550 nm," Journal of the Optical Society of America B: Optical Physics **18**, 750-761 (2001).
9. M. S. Keshner, "1/f NOISE," Proceedings of the IEEE **70**, 212-218 (1982).

Chapter 5

All Fibre Optical Delay Line for Optical Coherence Tomography Application

This chapter will review the technologies and techniques behind the construction of an all fibre optical delay line. First, the types of optical delay lines used in the OCT system will be briefly presented. Overview of the CFBG used in the construction of an all fibre optical delay line will be given as well. Then, the development and construction of the all fibre optical delay line will be reported.

5.1 Introduction to Optical Delay Line

Scanning range and repetition rate are one of the major parameters in optical delay line. In most applications, it is desirable to have a high repetition rate and large scanning range to improve the signal-to-noise ratio (SNR) of the application system. Among other applications, that use the optical delay line as its key component, are [1]:

1. Frequency-resolved optical gating (FROG) for the measurement and characterization of ultrafast pulses.
2. Optical autocorrelation for the measurement of intensity versus time of optical pulses.
3. Clocking and delay generation for time-division multiplexing in optical communications.
4. Optical low coherence reflectometry (OLCR) for fault detection in optical waveguides.

In the time-domain OCT setup, optical delay line techniques based on linear translation of reflective elements, rotational methods, fibre stretching and group delay generation based on Fourier domain technique have been reported [2]. In this chapter, the delay line technique based on FBG will be reviewed and reported. This technique, when compared with the previous techniques, can provide greater mobility from the elimination of bulk optics, a larger path delay amplification and subsequently deeper depth penetration into sample.

5.2 Overview of Fibre Bragg Grating

Fibre Bragg gratings (FBGs) are typically made in silica optical fibres with cores doped with germanium. These germanium-doped fibres will exhibit increased photosensitivity and, together with the introduction of hydrogen into the core, this will further enhance the photosensitivity effect. These two effects combine to create the periodic variation of the refractive index in the core region when subject to a periodic pattern of UV illumination.

The common fabrication technique of FBGs nowadays is using a phase mask [3]. Upon the incidence of UV beam, the grooves on the UV-transmissive mask plate will cause the incidence beam to be diffracted, into several orders, $m = 0, \pm1, \pm2\ldots$. This is shown schematically in Fig. 5.1.

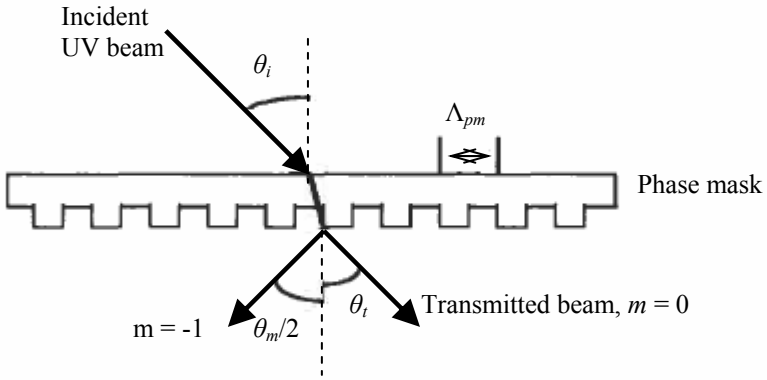

Fig. 5.1: Diffraction of UV beam upon incidence on a phase mask.

The incident and diffracted orders satisfy the general diffraction equation, with the period, Λ_{pm}, of the phase mask

$$\Lambda_{pm} = \frac{m\lambda_{UV}}{\left(\sin\frac{\theta_m}{2} - \sin\theta_i\right)} \tag{5.1}$$

where $\theta_m/2$ is the angle of the diffracted order, λ_{UV} is the wavelength, and θ_i is the UV beam's incident angle. Normally, the UV beam is incident normal to the phase mask and most of the diffracted light is contained in the zero, +1, and -1 diffracting orders.

In a uniform FBG, different wavelength components of an incident light are reflected at different positions along the grating, according to the local grating period [3]

$$\lambda_B = 2n_{eff}\Lambda \tag{5.2}$$

where λ_B is the Bragg wavelength, n_{eff} is the effective refractive index of the core mode and Λ is the grating period.

Most gratings designed for practical applications are non uniform gratings. Often the main reason is to reduce the undesirable sidelobes. While a uniform FBG has the same grating period along its whole length, a chirped fibre Bragg grating (CFBG) has a grating period which varies along its length which can take any functional form of linear, quadratic or even higher order. Chirping the period of the grating enables the dispersive properties of the scattered light to be tailored. CFBGs are useful for dispersion compensation, for controlling and shaping shorter pulses in fibre lasers and for creating stable continuous-wave (cw) and tunable mode locked external-cavity semiconductor lasers [4]. Linearly chirped FBGs are popular due to their linear group delay properties that can be used for performing dispersion compensation. Owing to the varying period, the spectrum of the CFBG is broader compared to a uniform FBG.

Fig. 5.2 shows a schematic of a chirped grating, of length L_{gr} and chirped bandwidth $\Delta\Lambda_{chirp}$. Note that the chirp in the period can be related to the chirped bandwidth, $\Delta\Lambda_{chirp}$ of the fiber grating as

$$\Delta\lambda_{chirp} = 2n_{eff}(\Lambda_{long} - \Lambda_{short}) = 2n_{eff}(\Delta\Lambda_{chirp}). \quad (5.3)$$

The reflection from a chirped grating is a function of wavelength and, therefore, broadband light entering into a positively chirped grating (increasing period from input end) will see the shorter wavelength component, λ_{short} reflected earlier than the longer one, λ_{long}.

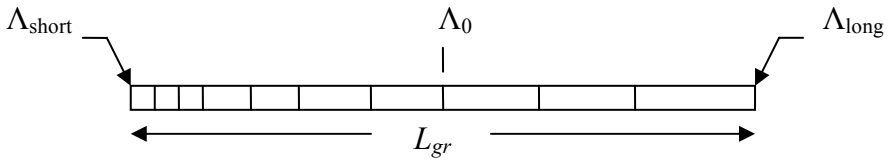

Fig. 5.2: Chirped grating.

Chirped gratings disperse light by introducing a delay between the shortest and longest reflected wavelengths. This dispersion can be used to compensate for chromatic dispersion induced broadening during optical transmission in a fibre.

Many OCT systems rely on bulk optics for an optical delay line in their reference arm. An all-fibre optical delay line in an OCT system can be made possible by constructing two CFBGs and positioning them in reversed cascaded orientation against each other. The idea of all fibre optical delay line for OCT applications was first proposed by Lee *et al.* [5]. The authors used a pair of CFBGs, and cascaded them in a reverse orientation manner to produce a delay when one of the gratings was stretched. By stretching one of the gratings, an optical delay of a few orders of magnitude greater than the actual physical stretch can be achieved. Much of the theoretical treatment for this method has been dealt with rigorously by Lee *et al.*[5] and Yang *et al.*[6]. Using this method, all fibre material can be realised in this mechanism where the inherent fibre advantage of low insertion loss, alignment free and ease of mobility can be achieved. The all fibre delay line too can offer amplified optical delay for the scanning of samples in the OCT system.

While straining the fibre under tension, it will introduce a wavelength shift in the grating. This shift of Bragg wavelength with strain can be expressed using [7]

$$\Delta\lambda_B = \lambda_B(1 - p_e)\varepsilon \tag{5.4}$$

where $\varepsilon = dl/L_{gr}$ is the applied strain, p_e is the elasto-optic coefficient, with numerical value ~0.22. For a chirped dispersion grating, its dispersion D is given by

$$D = \frac{2n}{c} \cdot \left(\frac{L_{gr}}{\Delta\lambda_{chirp}} \right) \tag{5.5}$$

where n is the effective refractive index, L_{gr} is the fibre length, c is the light speed and $\Delta\lambda_{chirp}$ is the chirped grating's bandwidth. The dispersion D is also associated with the group delay $t_g(\lambda)$ as

$$D(\lambda) = \frac{dt_g(\lambda)}{d\lambda} \tag{5.6}$$

where the group delay $t_g(\lambda)$ depends on the wavelength.

The presence of the time or phase ripple in the CFBGs group delay has been thought to contribute to the significant broadening in the interference signal in an OCT system [8]. Through the group delay, the phase of the light signal changes while travelling along the fibre. The group delay, t_g, experienced by the light pulse, is related to this phase shift, ϕ, by:

$$t_g(\lambda) = \frac{d\phi(\omega)}{d\omega} = -\frac{\lambda^2}{2\pi c} \cdot \frac{d\phi(\lambda)}{d\lambda} \tag{5.7}$$

where λ is the wavelength of the light pulse and c is the light velocity. Reversing and integrating Eq. 5.7, the phase shift, ϕ, can now be expressed as a function of the group delay, t_g, by

$$\phi(\lambda) = -2\pi c \int \frac{t_g(\lambda)}{\lambda^2} d\lambda \,. \tag{5.8}$$

Eq. 5.8 can be the basis for the phase ripple analysis of a CFBG in interference signal broadening. Interference signal broadening is a common phenomenon observed and is reported in Section 5.6 of this chapter.

In this chapter, an OCT system employing the all fibre optical delay line will be constructed. Before that, initial characterization of the CFBGs' group delay was performed to acquire the dispersion properties and the group delay ripple (GDR) of the gratings. Then the interference signal generated from CFBGs as an optical all fibre delay line in an OCT system is reported and discussed.

5.3 Chirped Fibre Bragg Gratings Characterization

Using the in-house fibre Bragg grating fabrication technology, a pair of linearly chirped FBGs was fabricated. The gratings are custom designed long CFBGs [9] that are made from a hydrogen loaded and germanium doped core single mode fibre at the operating wavelength of 1550 nm, of length 130 mm. The two gratings were fabricated with a raised cosine apodisation profile over ~2% and 50% respectively and thus yielded a top hat and a Gaussian-like shape function (Fig. 5.3) The apodisation is crucial to prevent sidelobes and thus prevent the image degrading in the OCT system. Both gratings were fabricated with a central wavelength at 1547 nm and the peak effective refractive index modulation was 3.7 x 10^{-4}, while the chirp rate in the gratings was kept at 3.846 nm/cm to yield the dispersion value of 25 ps/nm

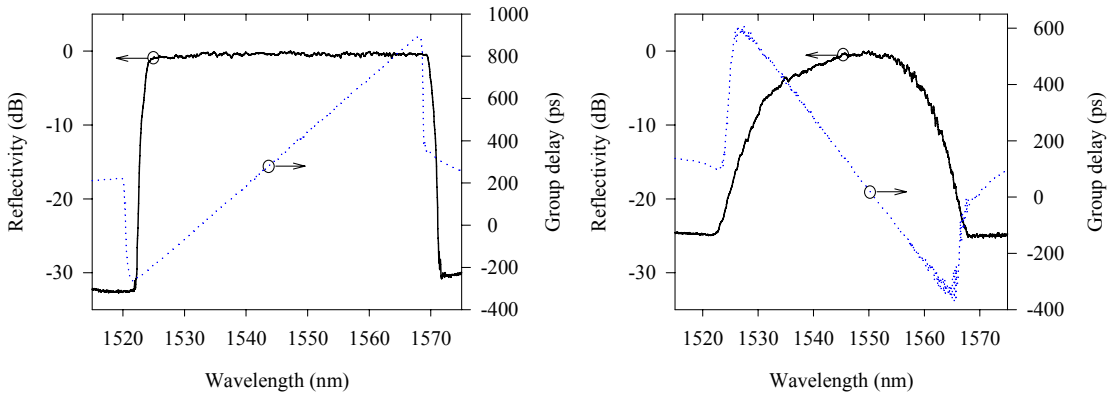

Fig. 5.3: Reflectivity spectrum and group delay for the top hat and Gaussian-shaped CFBGs. The top hat grating is characterized from the short wavelength side and has a 50 nm FWHM bandwidth with 25 ps/nm dispersion. The Gaussian grating is characterized from the long wavelength side and has a 23 nm FWHM bandwidth with -25 ps/nm dispersion.

with 70% reflectivity. The characteristics of these CFBGs when used as a broadband reflector and their group delay, are shown in Fig. 5.3. The reflected optical power of the gratings is measured by the optical spectrum analyser (OSA). The group delay property of these gratings is characterised using the modulation phase shift method [10]. The setup for this characterization method is shown in Fig 5.4.

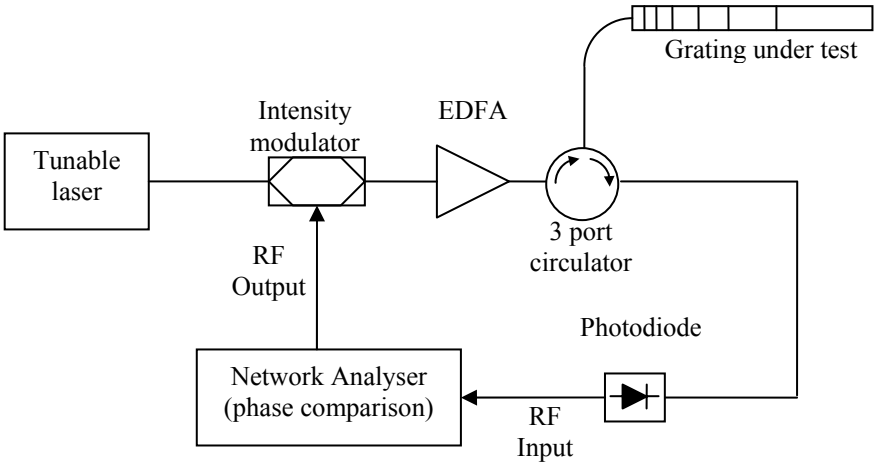

Fig 5.4: Measurement setup for the modulation phase method.

The input light from a tunable laser is modulated by an optical intensity modulator and the driving signal, with a frequency of *f*, is provided by the network analyser. The modulated light is then launched into the grating under test. The reflected light signal is then detected by a photodiode which later is introduced back into the network analyser. The network analyser compared the phase difference between the received signal and the driving electrical signal. As the wavelength of the tunable laser is tuned, the phase difference among different wavelengths $d\phi(\lambda)$ is scanned and analysed. The relative time delay at different wavelengths, which can be modified from Eq. 5.7, is given by

$$t_g(\lambda) = -\frac{\lambda^2}{2\pi c}\cdot\frac{d\phi(\lambda)}{d\lambda} = \frac{1}{f}\cdot\frac{d\phi(\lambda)}{2\pi}. \tag{5.9}$$

5.4 All Fibre Optical Delay Line Construction

Using these 2 gratings, a new all fibre optical delay line, as illustrated in Fig. 5.5, is designed. The top hat grating is UV glued at a point 1 cm away from both ends of the grating, onto a piezo controlled stage at one end and onto a fixed stage at the other end, thus giving a total of 150 mm length for straining (Fig 5.6). Since the top hat and Gaussian gratings are arranged in a reverse cascaded orientation, the dispersion value of the two gratings will then be compensated.

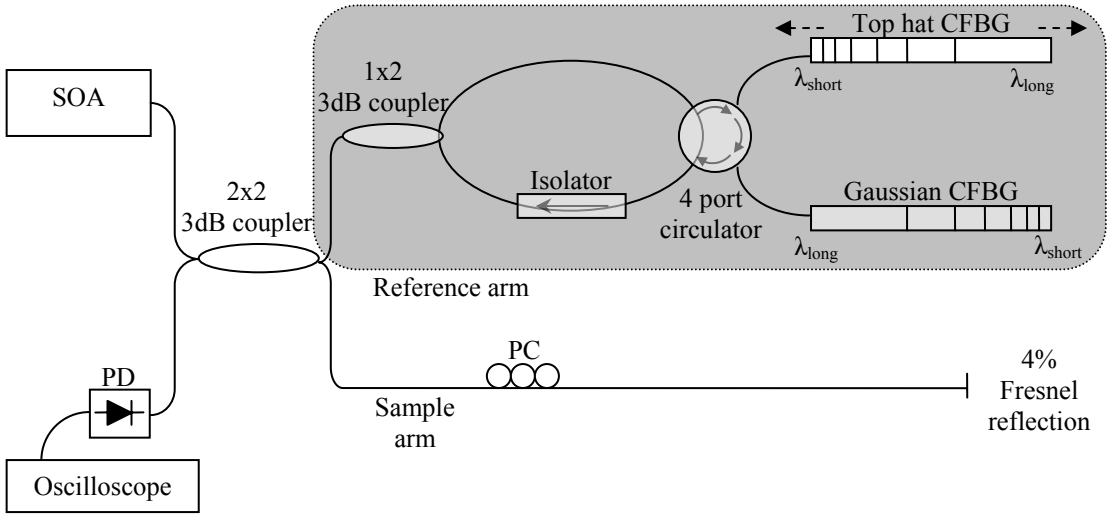

Fig. 5.5: Schematic diagram of the experimental set-up. SOA: semiconductor optical amplifier; PC: polarisation controller; PD: photodetector; CFBG: chirped fibre Bragg grating. The constructed all fibre optical delay line is highlighted in the shaded box.

Similarly with the original OCT setup, as reported in Section 3.2, the piezo stage is driven with a triangular waveform to simulate a linear extension of the grating, mimicking the real scanning mechanisms in the OCT system. A polarisation controller was affixed to the sample arm to prevent the mismatch of polarisation that arises from the induced birefringence in the constructed all fibre delay line. An isolator was placed between the 1x2 3dB coupler and the 4 port circulator to prevent the split signal from the light source from propagating in the reverse direction in the reference arm. Instead of constructing focusing optics to scan a sample, the Fresnel back-reflected signal from an end-cleaved fibre in the sample arm is used to match the coherence length in both the sample and reference arms. Using this method, the presence of bulk optics in the sample arm can be eliminated [11] and this proves that

dispersion from the scanning optics in the sample arm does not contribute to the defects of the interference signal.

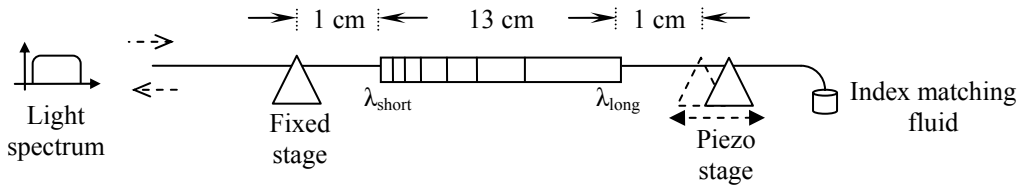

Fig. 5.6: Schematic diagram of how the top hat CFBG is glued onto the fixed stage and piezo stage.

5.5 Interference Signal Generation

An SOA with a 1535.13 nm centre wavelength, + 0.41 dBm power and a FWHM spectral bandwidth of 59.09 nm was used as the broadband, ASE light source. Light travels in this reference arm in the following manner. Light will be split in half at the 1x2 3 dB coupler. The one half of the split light will enter and circulate the 4 port circulator. The other half will be stopped at the isolator. While circulating through the circulator ports, the light will be backreflected twice from the two gratings attached to it. The first backreflection comes from the top hat grating that is under a controlled stretch. The second grating will shape the light into a Gaussian-like shape. Then the light will return to the 2x2 3 dB coupler, to interfere with light from the sample arm, before hitting the photodetector.

Stretching the top hat grating will introduce a Bragg wavelength shift. Because there is a dispersion property in the grating, the Bragg wavelength shift will translate to a shift of time delay in the top hat grating. The Gaussian grating is a nearly identical grating to the top hat grating except for its spectral shape. Thus, every point in this grating is a mere reflection point to each wavelength component of the earlier backreflected light from the top hat grating.

The reflection spectral profile resulting from the shaping of both gratings will determine the shape of the interference signal as well. In this case, the final spectrum is a Gaussian-like spectral shape incident on the photodetector, with the advantage of giving suppression of unwanted sidelobes at its intereference signal shape. In order to generate an interference signal, light from both the sample and the reference arm need to interfere at the 2x2 3 dB coupler before being incident on the photodetector.

5.6 Result and Discussion

The shift of Bragg wavelength, $\Delta\lambda_B$, with strain can be expressed using $\Delta\lambda_B=\lambda_B(1-p_e)\, dl/L_{gr}$ (Eq. 5.4), where dl is the applied stretch on the strained grating length, L_{gr}, and p_e is the elasto-optic coefficient with a numerical value ~0.22. The top hat grating is stretched by 162 μm; this will give rise to Bragg wavelength shift and time delay of 1.33 nm and 33.37 ps respectively. This actually corresponds to a 3.45 mm depth for scanning which is sufficient for the penetration of light into the OCT sample. The generated interference signal is shown in Fig. 5.7.

The coherence length, l_c, which is the measure of the axial resolution in OCT, is given by Eq. 2.14 in Section 2.1. The FWHM of the interference signal was measured to be ~100 μm. Its coherence length is significantly broadened compared to the theoretically predicted coherence length at 48 μm. The shape of the signal was an approximate form of the interference signal in Fig. 4.6 (e).

The generated interference signal from the constructed all fibre optical delay line, is anticipated to be a Gaussian-like shape, has been broadened by more than twice the FWHM magnitude. It is speculated that the difference between the experimental and the actual value can be attributed to the small dispersion imbalance between the two CFBGs, in this new reference arm, together with the presence of group delay ripple and phase ripple in the gratings. Light of broadband nature has many wavelengths travelling at a group velocity. At large optical bandwidths, the effect of dispersion on the interference signal, and hence the axial resolution, becomes significant. Such a case has been reported where the light which enters the tissue, for example, will undergo dispersion [12]. The different wavelengths return at slightly different times. Hence the wider the bandwidth the higher the dispersion. In an extreme case, if the dispersion is too great, the reference and sample arms will no longer interfere and need to be compensated. After passing through the two gratings, the effect of the gratings' slight dispersion mismatch can cause the interference signal to be widened and its frequency dispersion is then no longer symmetric. The selection of an isolator, a 1x2 coupler and a circulator which are not entirely wavelength flattened may have caused the Gaussian backreflected signal from the Gaussian grating to be slightly distorted. This may have caused the interference signal to be distorted and out of its original Gaussian shape.

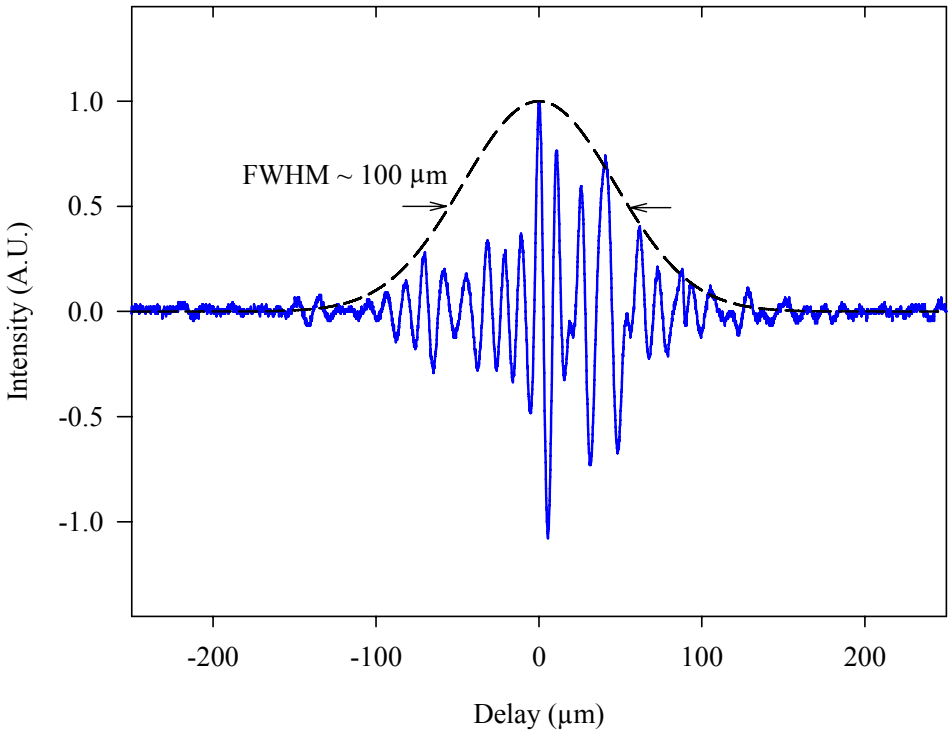

Fig. 5.7: Interference signal (solid) and the Gaussian envelope fit (dash) of a Fresnel backreflected signal from the end-cleaved fibre in the constructed all fibre optical delay line OCT system.

But mainly, the presence of group delay ripple was thought to be the reason for this broadening. In the future work, detailed in Chapter 6, a theoretical analysis of the phase and group delay ripple in CFBGs will be suggested to find the cause. More experimental investigation can be carried out in terms of numerical work to understand the theoretical treatment of the phase ripple on the interference signal. Future work can be concentrated on the simulation of the effect of these ripples on the interference signal broadening.

5.7 Doppler Frequency Observation

Going back to the same experimental setup as in Fig. 3.7, the Doppler frequency of the new constructed delay line was measured. Three Doppler frequency measurements were taken at 1 Hz, 2 Hz and 3 Hz piezo stage driving frequencies. The recorded power incident on the photodetector (Model 1811, New Focus) was -21.36 dBm. This was lower than the earlier Doppler frequency observation in Section 3.4, because of the multiple insertion loss introduced by circulators, gratings, couplers and isolator in the delay line. The first Doppler frequency (Fig. 5.8 (a)) has the peak centred at ~500 Hz. The Doppler frequencies in Fig 5.8 (b) have their peaks centred ~1 kHz. Lastly the Doppler frequencies in Fig 5.8 (c) have their peaks concentrated in-between the peaks of ~1.5 kHz. The recorded parameters, on the Marconi RF spectrum analyser, are as follows. All the three measurements are subject to only one time sample averaging, as multiple times averaging will cause the peaks to gradually decrease and diminish towards the end. The video bandwidth and resolution bandwidth for the spectrum analyser was maintained at 87 Hz and 100 Hz respectively. The signal attenuation into the spectrum analyser is 10 dB.

Again, similarly with the experimental setup carried out in Section 3.4, frequency broadening is observed together with the increment of piezo driving frequency. The reasons for the frequency broadening are also thought to be the same. The interference signal generated has other frequency components besides the Doppler frequency itself. Also, the unstable centre frequency, generated from the function generator that is used to drive the piezo stage, may have contributed to the frequency broadening too. This time, the distance of these peaks are no more 50 Hz apart and thus it can be assured that the AC power line does not contribute to the appearance of these multiple frequency peaks. By eliminating the mirror delay, the newly constructed all fibre optical delay line would also not contribute any resonance frequency to these multiple frequency peaks.

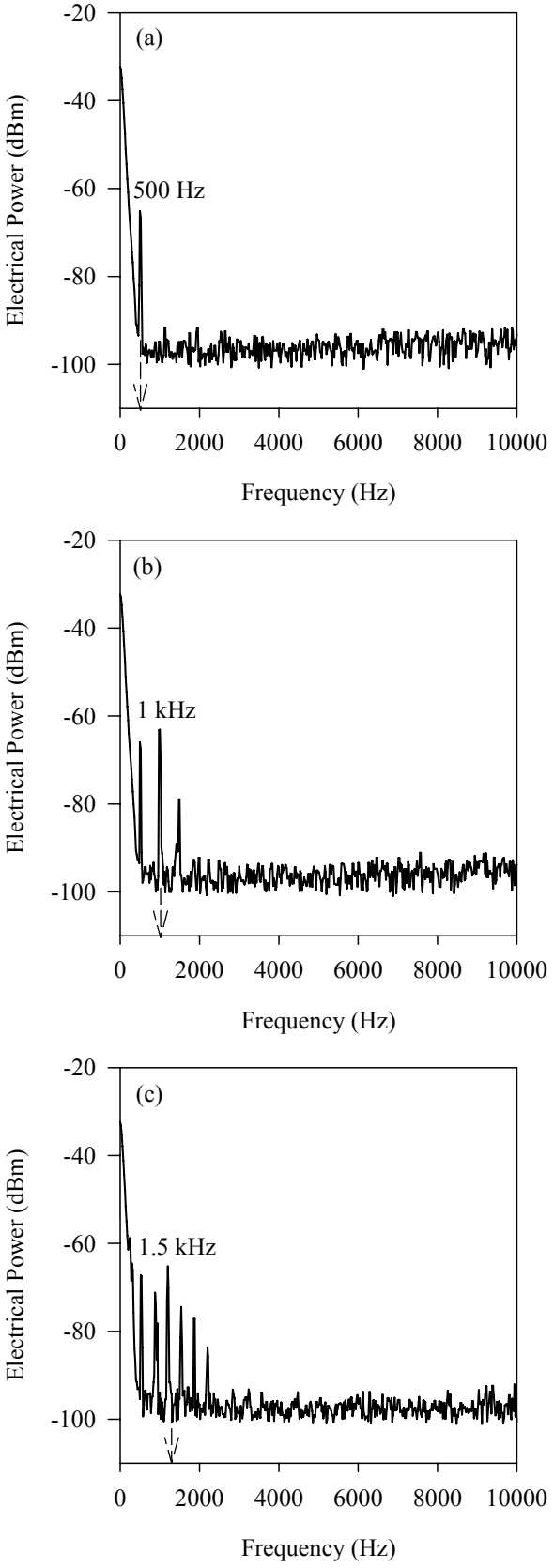

Fig. 5.8: Doppler frequency of the all fibre optical delay line driven at (a) 1 Hz (b) 2 Hz and (c) 3 Hz. The Doppler frequency broadening is observed together with the increment of the driving frequency.

5.8 Summary

The construction of an all fibre optical delay line utilising a pair of CFBG has been covered in this chapter. The gratings are fabricated with a top hat and Gaussian shape-like function and each yields a dispersion value of 25 ps/nm. While cascading the gratings in a reverse orientation, the dispersion values are canceled out. When the top hat grating is stretched, an interference signal is obtained. The Bragg wavelength shift of 1.33 nm, from a stretch of 162 μm to the top hat grating gave a penetration depth scan of ~3.45 mm. This is more than adequate for depth scanning in OCT applications. The fringe's FWHM at 100 μm showed a broadening of twice the theoretical value of 48 μm. The reason for this is believe to be due to the slight dispersion mismatch in the OCT arms and the contribution of phase ripple in the gratings. The measured Doppler frequencies are the same as with the earlier measured frequency when using a flat mirror in the reference arm. This study has paved the way for a more in-depth study of grating phase ripple in the future, as will be detailed in Chapter 6.

5.9 References

1. L. P. Sanz, "High Speed Optical Delay Line for Optical Coherence Tomography," in *MSc Thesis*(Technical University of Denmark, Roskilde, 2004).
2. B. E. Bouma, and G. J. Tearney, *Handbook of Optical Coherence Tomography,* (Marcel Dekker, New York, 2002).
3. R. Kashyap, *Fiber Bragg Gratings* (Academic Press, New York, 1999).
4. T. Erdogan, "Fiber grating spectra," Journal of Lightwave Technology **15**, 1277-1294 (1997).
5. B. H. Lee, T. J. Eom, E. Choi, G. Mudhana, and C. Lee, "Novel Optical Delay Line for Optical Coherence Tomography System," Optical Review **10**, 572-575 (2003).
6. C. Yang, S. Yazdanfar, and J. Izatt, "Amplification of optical delay by use of matched linearly chirped fiber Bragg gratings," Optics Letters **29**, 685-687 (2004).
7. A. D. Kersey, M. A. Davis, H. J. Patrick, M. LeBlanc, K. P. Koo, C. G. Askins, M. A. Putnam, and E. J. Friebele, "Fiber grating sensors," Journal of Lightwave Technology **15**, 1442-1463 (1997).
8. E. Choi, J. Na, S. Y. Ryu, and B. H. Lee, "Strained chirped fiber Bragg gratings based all-fiber variable optical delay line for optical coherence tomography," Optical and Quantum Electronics **37**, 1263-1276 (2005).
9. M. Ibsen, M. K. Durkin, M. N. Zervas, A. B. Grudinin, and R. I. Laming, "Custom Design of Long Chirped Bragg Gratings: Application to Gain-Flattening Filter with Incorporated Dispersion Compensation," IEEE Photonics Technology Letters **12**, 498-500 (2000).
10. Z. Zhang, "Passive and Active Bragg Gratings for Optical Networks," in *Ph.D Thesis, Optoelectronics Research Centre*(University of Southampton, Southampton, 2007).
11. E. Choi, J. Na, S. Y. Ryu, G. Mudhana, and B. H. Lee, "All-fiber variable optical delay line for applications in optical coherence tomography: Feasibility study for a novel delay line," Optics Express **13**, 1334-1345 (2005).
12. M. E. Brezinski, *Chapter 5, Optical Coherence Tomography: Principles and Applications* (Elsevier, Burlington, 2006).

Chapter 6
Conclusions and Future Work

6.1 Summary

In this thesis, the development and construction of a time-domain OCT system has been documented. A time-domain OCT system, utilising a mirror delay line at its reference arm, has been designed. Its system performance has been demonstrated by scanning a glass slide, a plastic sheet and a plastic laminator sample. The measured fringe separation distance is in good agreement with the actual measured samples' thickness. Thus, the unit can be used to perform a meaningful scan on any transparent and thin samples. A simple and crude early stage OCT tomogram has been obtained by scanning a mirror sample. A scan has been performed on an onion skin and small features of the cellular structure, such as its borders and the middle of hollow cells, can be determined. Overall, the constructed time-domain OCT system is able to perform a crude meaningful scan on a simple biological sample.

This thesis also documented the work of a noise study of a broadband source for application in the OCT system. The broadband source of interest in this case is the high power, light-weight SC450 supercontinuum source (Fianium, UK). Interference signals generated from this source were compared with other thermal-like sources; i.e.; SOA and EDFA. A flat top and a Gaussian-like grating filter were used to shape the broadband sources' signal. The sources exhibit the exact Fourier transform interference signal of their own filtered shape. The RIN value for the different filters, using different broadband sources, has been compared and discussed too. For the Gaussian shaped signal, the RIN value is slightly higher compared to the flat top shaped signal. With the help of Dr. Anoma McCoy, the RIN value for the filtered broadband sources have been calculated and predicted. Except for the SC450 source, which is not a pure thermal source, the measured RIN value of each filtered SOA and

EDFA source are in good agreement with their predicted values. The SC450 source exhibits a high signal fluctuation and is noisier when compared to the SOA and EDFA. This source is noisier due to two reasons; the factor of 2 increments in intensity noise from its polarised signal and the nonlinear amplification of the intensity noise in the pump laser due to complex nonlinear phenomena. Nevertheless, the SC450 can still be utilised as a potential broadband source for OCT applications based on the stability of its interference signal.

Later, realising that the constructed time-domain OCT system is very slow and has very limited depth scanning penetration, the all fibre optical delay line is constructed and then its operation is demonstrated. Using a pair of nearly identical CFBGs, differing only in their coherence function shape, the gratings are cascaded in a reverse orientation manner. This cancels out each other's dispersion value. A nearly Gaussian-like interference signal was produced when one of the CFBG was stretched. A small stretch of the top hat grating amplified the depth scan penetration available at the sample arm. The depth penetration is improved from the actual physical displacement of 162 μm to 3.45 mm. Unfortunately the FWHM, or axial resolution, is broadened by twice the magnitude of its theoretical value. The future work, as highlighted in the next section, will discuss the methods and challenges to improve this system.

6.2 Future Work

6.2.1 Noise Suppression

Limiting the noise is the key to achieving high resolution imaging in OCT. Broadband CFBG filters centred at shorter wavelengths (1310 or 1100 nm), instead of the 1550 nm wavelength, can be designed to characterize the interference signal and its RIN. These wavelengths too are better suited in the OCT application due to the lower scattering and absorption characteristics of the sample under test. Most of the samples under OCT characterisation consist of inhomogeneous biological samples. The nature of the supercontinuum source's noise, either concerning the pump laser or the PCF fundamental properties, is yet to be fully investigated. More experimental work can be carried out to further establish the nature of the noise of the SC450 source before incorporating it into a high resolution OCT system. Once the parameters

are known and the causes are determined, the possibility of reducing these noise sources can be studied too in the future.

For the time being, by using the conventional balanced detection system, it will be possible to increase the signal-to-noise ratio of the OCT system. The commercial unit, model Nirvana^{TM}, auto-balanced photodetector (New Focus, Inc.) can provide the said solution, as depicted in Fig. 6.1. The suggested configuration, in Fig. 6.1, will introduce the isolator between the C_1 and C_2 couplers to ensure that the backreflected beam from the reference mirror will not increase the shot noise on the photodetector. The equally split signal at the coupler can ensure that the intensity noise is properly suppressed. In addition, the attenuator at one of the photodetector arms can improve the detection efficiency. Attenuation at 3 dB is preferable, as the common mode rejection ratio (CMRR) is maximised when power in the reference input of the photodetector is twice that in the input signal.

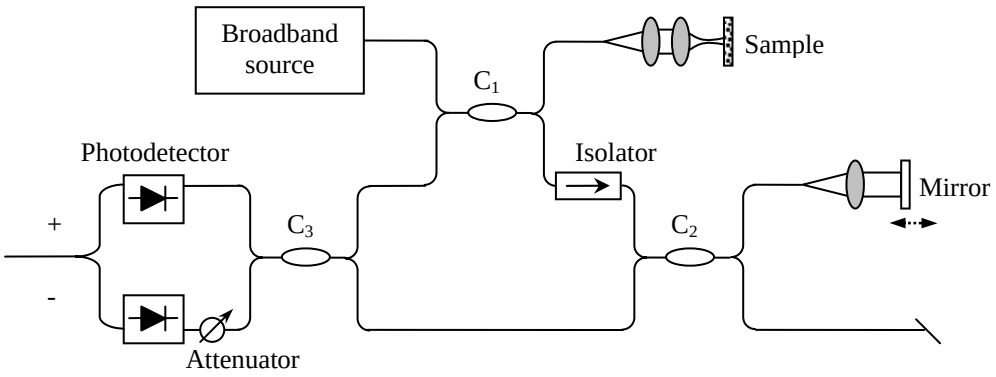

Fig. 6.1: OCT system with balanced photodetector.

6.2.2 One micrometer Centre Wavelength Broadband Source

The considerations for choosing a light source need to take into account the penetration depth and the absorption coefficient of water in a biological sample. It has been shown that the dispersion zero of water is close to 1 μm wavelength [1] and the effect of dispersion on the interference signal broadening can be minimised by operating at this wavelength. Examples of broadband sources, that can emit at 1 μm centre wavelength, are SLDs and some Ytterbium (Yb) doped fibre sources. An Yb ASE source is a perfect example for the usage in the OCT system as it is readily

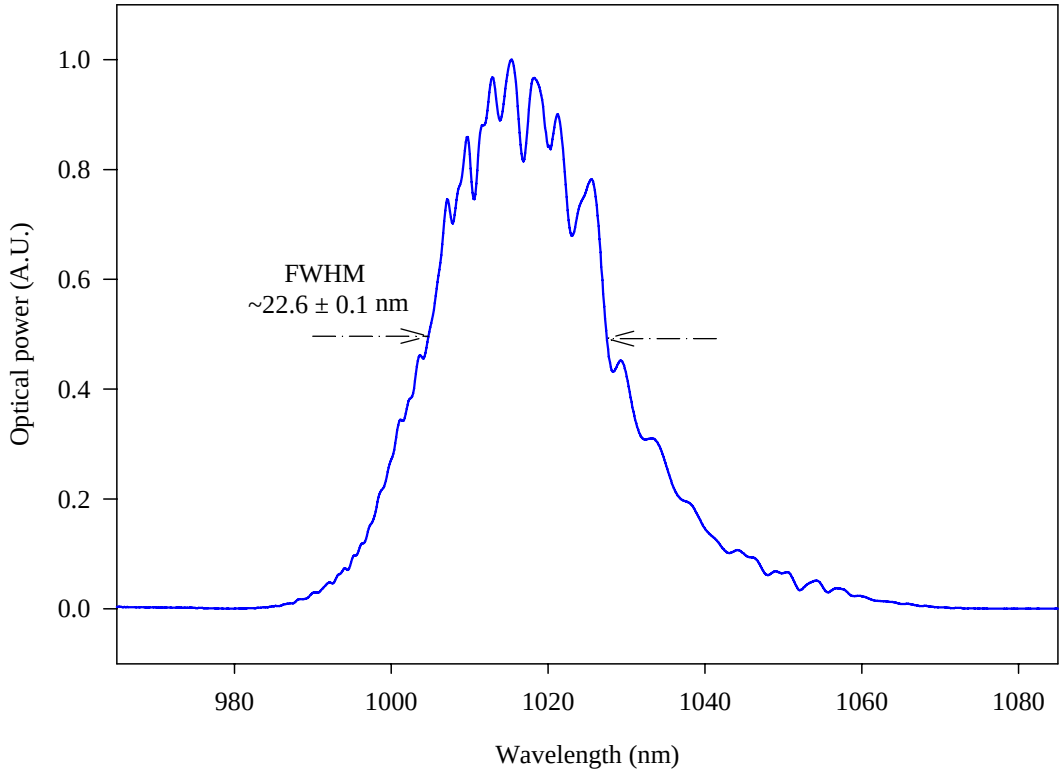

Fig. 6.2: Emission spectrum of an in-house Yb ASE source.

available in the ORC grating lab. Its spectrum is shown in Fig. 6.2. Its centre wavelength is at 1016.1 nm and the FWHM bandwidth is 22.6 nm. Its maximum recorded power is 80 μW, or -11 dBm. At this optical bandwidth the axial resolution for OCT will be 20.1 μm.

Take note that, when using the broad bandwidth spectrum centred at 1 μm, the spectrum actually covers large portions of the detector sensitivity interface between silicon and indium-germanium-arsenic (InGaAs) detectors. Germanium or Si–InGaAs sandwiched detectors might be used, but these are less sensitive than silicon and InGaAs detectors alone [2]. Fortunately, the InGaAs photodetector unit (D400FC, Thorlabs) that was used throughout all the previous experiments, has a wide spectral response, i.e., 800 nm – 1700 nm. This will be sufficient for a 1 μm central wavelength signal, provided that the broadband source does not emit below 800 nm wavelength.

Besides the photodetector, the output response of the OCT system is also determined by the optical properties of the interferometer used. This covers the wavelength-dependent losses and splitting ratios of the beamsplitter, as well as the

cut-off wavelength of the single-mode fibres (SMFs) employed. A common error that many researchers made was to mix together the different components with different centre operating wavelengths in their setup. Each optical component is custom made for its optimum operating wavelength. Special care needs to be taken especially when splicing the fibres in the OCT setup. Due to different core and, hence, mode sizes, when the light travels from 1.55 μm SMF into 1 μm SMF or vice versa, there will be a significant splice loss. The minimum loss theoretically possible from this splice can be shown using the following equation [3]

$$\text{Minimum loss} = 10\log_{10}(4r_1^2 r_2^2 (r_1^2 + r_2^2)^{-2}) \tag{6.1}$$

where r_1 = 5.25 μm and r_2 = 2.95 μm [4] are the mode field radii for the 1550 nm SMF and 1060 nm SMF respectively. Therefore, for each fibre splice there will be a minimum loss of ~ -1.37 dB. This problem can be avoided entirely by using 1 μm operating wavelength components throughout the whole OCT setup.

6.2.3 Interference Signal Broadening Simulation

In Chapter 5, the interference signal is broaden from its theoretical axial resolution of 48 μm to more than a factor of two at 100 μm. As speculated earlier, this can be attributed to the phase ripple or noise properties in the gratings [5]. In Chapter 5 too, the group delay property (Fig. 5.3) is presented for both the gratings used in the construction of the all fibre optical delay line. Fig. 6.3 shows the group delay ripples (GDRs) in both gratings, which are obtained by taking a linear fit of the group delay property and subtracting it from the measured group delay values. Random fluctuations of up to ±10 ps and ±30 ps are observed for the top hat grating and Gaussian grating respectively. At present, the tolerance value of GDR that will influence the performance of the OCT system is still unknown. Nevertheless, the presence of the GDR will become the essential study in the future to understand the performance of an all fibre optical delay line OCT system.

The amplitude of the phase ripples is more indicative of the performance of the chirped grating [6]. The phase ripple information in the grating can be obtained using Eq. 5.8. This information can be extracted from the earlier group delay

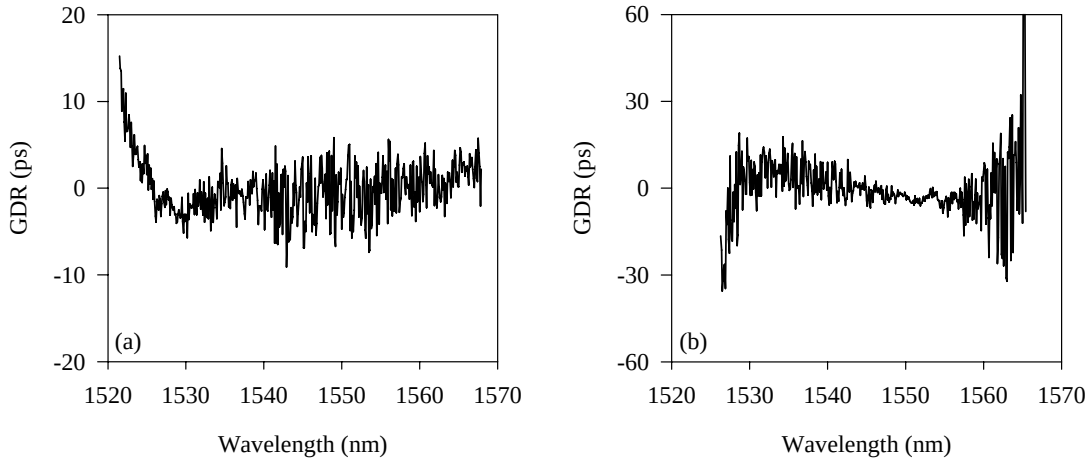

Fig. 6.3: Group delay ripple of (a) top hat grating and (b) Gaussian grating.

properties of the top hat and Gaussian gratings, from Fig. 5.3. The extracted phase ripple properties are presented in Fig. 6.4.

Here, the study can be constrained to phase ripples, as opposed to group delay or time ripple. By applying various periods and amplitudes onto the phase ripple, the effect on the interference signal shaping can be interrogated. A relationship needs to be established first between the phase noise and the stretching of the gratings in the reference arm that can contribute towards the interference signal broadening. It is hoped, in the future, that the nature of the phase ripple presence can be determined.

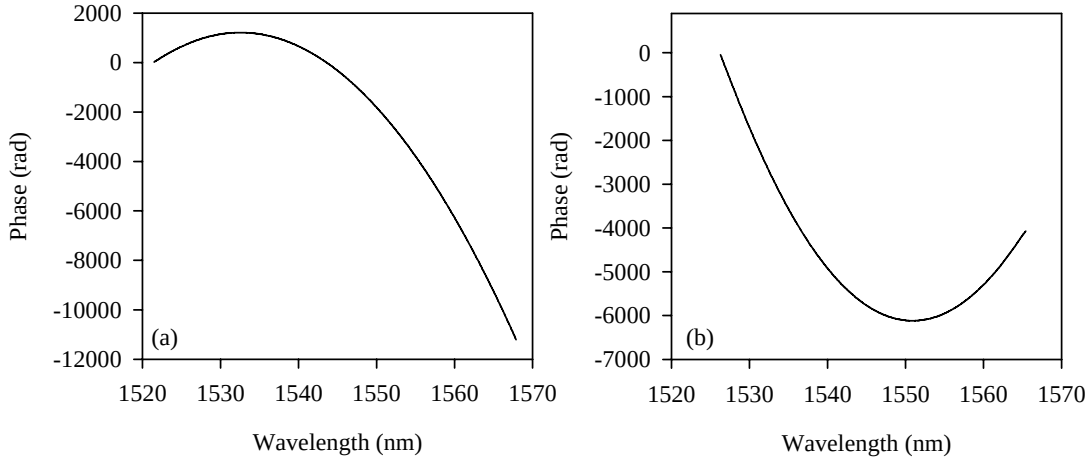

Fig. 6.4: The phase ripple of (a) top hat grating and (b) Gaussian grating are simulated by employing Eq. 5.8 using the group delay data in Fig. 5.3.

6.2.4 Depth of Focus Improvement

The depth of focusing on the current OCT system can only focus at a meagre depth of 18.59 μm. There are two ways to improve the depth of focus. Using a technique called optical coherence microscopy (OCM), Izatt *et al.* [7] have produced a series of two dimensional *en face* images using a high numerical aperture objective lens. By adjusting the focus of the lens, the authors are able to penetrate further into the sample and produce a series of depth scans. This is done by incorporating the light rejection mechanism of a confocal microscopy setup and the coherence gating technique of OCT. Another technique that can be used is to apply a form of dynamic focusing of scanning optics at the sample arm [8]. This can be achieved by using a special optical setup that can shift the focusing beam that is incident on the sample. All this can be done without changing the optical path length in the interferometer's arms.

6.2.5 Fibre Optic Endoscope

The current OCT endoscope is bulky, expensive and full of moving mechanical parts [9]. Fibre optic endoscopes are finding acceptance in biomedical imaging because of their compactness and practicality in usage. Because of their distinct miniscule size, this implies that they can be inserted into a blood vessel, for example, for health monitoring purposes and many other suitable healthcare applications. The idea of adapting this fibre optic endoscope into an OCT system has been of great excitement and could revolutionize the medical industry. The endoscope instrument itself can offer the inherent advantage of being safe and cheap, in addition to its convenience of usage. Clinical applications of endoscopic OCT systems requires probes that are quickly replaceable, cheap, compact and robust. A fibre optic endoscope can be designed initially for proof of concept, before implementing it in the OCT system. The current OCT setup is fibre based, thus enabling the possibility of implementing fibre endoscope and catheter based imaging.

6.3 References

1. Y. Wang, J. S. Nelson, Z. Chen, B. J. Reiser, R. S. Chuck, and R. S. Windeler, "Optimal wavelength for ultrahigh-resolution optical coherence tomography," Optics Express **11**, 1411-1417 (2003).

2. W. Drexler, "Ultrahigh-resolution optical coherence tomography," Journal of Biomedical Optics **9**, 47-74 (2004).

3. C. R. Pollack, *Fundamentals of Optoelectronics* (Irwin, Chicago, 1995).

4. http://www.corning.com/opticalfiber.

5. E. Choi, J. Na, S. Y. Ryu, and B. H. Lee, "Strained chirped fiber Bragg gratings based all-fiber variable optical delay line for optical coherence tomography," Optical and Quantum Electronics **37**, 1263-1276 (2005).

6. J. F. Brennan, "Broadband fiber Bragg gratings for dispersion management," Journal of Optical and Fiber Communications Reports **2**, 397-434 (2005).

7. J. A. Izatt, M. D. Kulkarni, W. Hsing-Wen, K. Kobayashi, and M. V. Sivak, Jr., "Optical coherence tomography and microscopy in gastrointestinal tissues," IEEE Journal of Selected Topics in Quantum Electronics **2**, 1017-1028 (1996).

8. F. Lexer, C. K. Hitzenberger, W. Drexler, S. Molebny, H. Sattmann, M. Sticker, and A. F. Fercher, "Dynamic coherent focus OCT with depth-independent transversal resolution," Journal of Modern Optics **46**, 541-553 (1999).

9. G. J. Tearney, S. A. Boppart, B. E. Bouma, M. E. Brezinski, N. J. Weissman, J. F. Southern, and J. G. Fujimoto, "Scanning single-mode fiber optic catheter-endoscope for optical coherence tomography," Optics Letters **21**, 543-545 (1996).

Appendix A

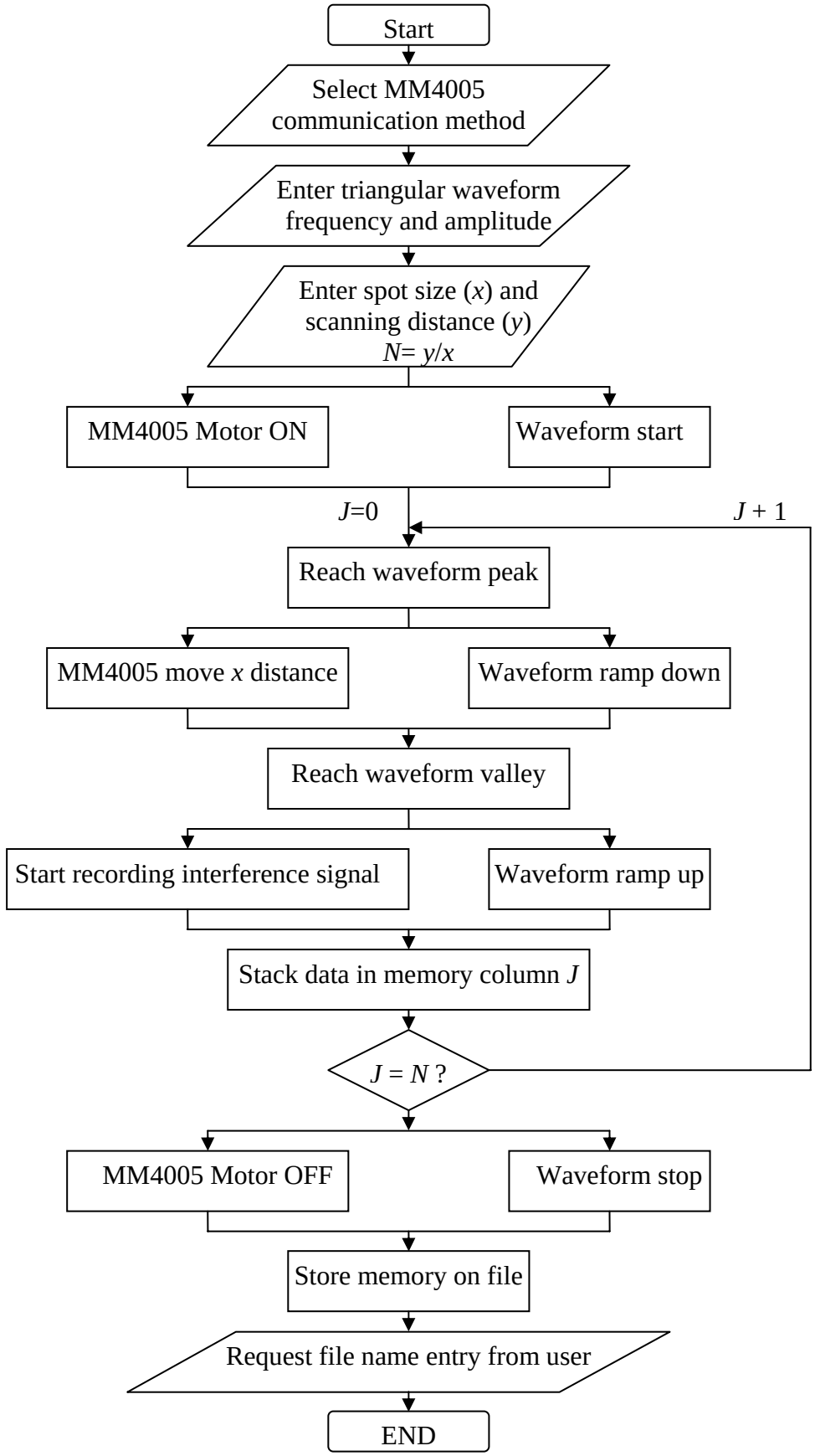
Start
Select MM4005 communication method
Enter triangular waveform frequency and amplitude
Enter spot size (x) and scanning distance (y)
N= y/x
MM4005 Motor ON
Waveform start
J=0
J + 1
Reach waveform peak
MM4005 move x distance
Waveform ramp down
Reach waveform valley
Start recording interference signal
Waveform ramp up
Stack data in memory column J
J = N ?
MM4005 Motor OFF
Waveform stop
Store memory on file
Request file name entry from user
END

Appendix B

Fianium PRODUCT DATASHEET

SuperContinuum Source SC450

KEY FEATURES

- Ultra-broadband light source
- Spectral range: 460 -2000 nm
- Spectral density up to 5 mW/nm
- Output power up to 6 W
- Small footprint
- Maintenance free

APPLICATIONS

- Fundamental study
- Optical coherence tomography
- Bio-medical
- Metrology

DESCRIPTION

SC450 is a high power fiber laser generating supercontinuum radiation in the 460 –1700 nm spectral band with average power up to 6W. The laser consists of a master source based on the FemtoMaster1060, a custom made nonlinear high power fibre amplifier. The lasers areair-cooled, maintenance free and do not require any adjustments.

Fianium

PRODUCT DATASHEET

TYPICAL SPECIFICATION

Parameters	Unit	SC450-2	SC450-4	SC450-6
Spectral bandwidth	nm	460-1800	460-1900	460-2000
Spectral flatness	dB	‹ 6		
Master source pulsewidth	ps	5		
Repetition rate	MHz	20	40	50
Average power	W	2	4	6
Spectral density	mW/nm	› 1.5	› 3	› 4.5
Power consumption, max	W	‹ 100		‹ 200
Dimensions (W x L x D)	mm	300 x 250 x 120		
Weight	kg	4.5		

OPTIONS

A variety of customised options such as:

- **spectral bandwidth**
- **output power**

are available on customer request. Performance can be tailored to the customer's requirements.

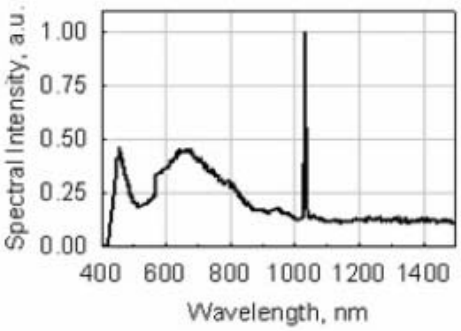

Typical optical spectrum SC450 in linear scale

CAUTION: THIS IS CLASS 4 LASER PRODUCT AND USE OF CONTROLS AND ADJUSTMENTS OTHER THAN THOSE SPECIFIED IN THE PRODUCT MANUAL MAY RESULT IN HAZARDOUS LASER RADIATION EXPOSURE

FIANIUM UK

20 Compass Point, Ensign Way
Southampton SO31 4RA, UK
Tel: +44 2380 458776
Fax: +44 2380 458734
www.fianium.com
info@fianium.com

FIANIUM INC

132 East Broadway, Suite 810
Eugene OR 97403 USA
Tel: +1 541 343 6767
Fax: +1 541 343 1838
www.fianium.com
sales@fianium.com